ALI NAWAZ

MODIFICATION OF CHARGE TRANSPORT PROPERTIES IN DEFECT-FREE POLY(3-HEXYLTHIOPHENE-2,5-DIYL) FIELD-EFFECT TRANSISTORS

CURITIBA

2017

ALI NAWAZ

MODIFICATION OF CHARGE TRANSPORT PROPERTIES IN DEFECT-FREE POLY(3-HEXYLTHIOPHENE-2,5-DIYL) FIELD-EFFECT TRANSISTORS

Thesis presented in partial fulfillment of the requirement for the degree of PhD. in Physics at the Department of Physics of Universidade Federal do Paraná.

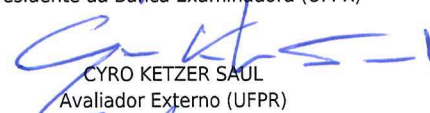Advisor: Prof. Dr. Ivo Alexandre Hümmelgen

CURITIBA

2017

ATA Nº **27**

ATA DE SESSÃO PÚBLICA DE DEFESA DE TESE PARA A OBTENÇÃO DO
GRAU DE DOUTOR EM FÍSICA

No dia quinze de Dezembro de dois mil e dezessete às 08:30 horas, na sala PE04, Depto. de Física - Centro Politécnico , do Setor de CIÊNCIAS DE CIÊNCIAS EXATAS da Universidade Federal do Paraná, foram instalados os trabalhos de arguição do doutorando **ALI NAWAZ** para a Defesa Pública de sua Tese intitulada: **"Modification of charge transport properties ind defect-free poly (3 -hexylthiophene - 2,5 - diyl) field-effect transistors"**. A Banca Examinadora, designada pelo Colegiado do Programa de Pós-Graduação em FÍSICA da Universidade Federal do Paraná, foi constituída pelos seguintes Membros: IVO ALEXANDRE HUMMELGEN (UFPR), CARLOS CÉSAR BOF BUFON (CNPEM), CYRO KETZER SAUL (UFPR), HENRI IVANOV BOUDINOV (UFRGS), JOSÉ PEDRO MANSUETO SERBENA (UFPR). Dando início à sessão, a presidência passou a palavra ao discente, para que o mesmo expusesse seu trabalho aos presentes. Em seguida, a presidência passou a palavra a cada um dos Examinadores, para suas respectivas arguições. O aluno respondeu a cada um dos arguidores. A presidência retomou a palavra para suas considerações finais. A Banca Examinadora, então, e, após a discussão de suas avaliações, decidiu-se pela _APROVAÇÃO_ do aluno. O doutorando foi convidada a ingressar novamente na sala, bem como os demais assistentes, após o que a presidência fez a leitura do Parecer da Banca Examinadora. A aprovação no rito de defesa deverá ser homologada pelo Colegiado do programa, mediante o atendimento de todas as indicações e correções solicitadas pela banca dentro dos prazos regimentais do programa. A outorga do título de doutor está condicionada ao atendimento de todos os requisitos e prazos determinados no regimento do Programa de Pós-Graduação. Nada mais havendo a tratar a presidência deu por encerrada a sessão, da qual eu, IVO ALEXANDRE HUMMELGEN, lavrei a presente ata, que vai assinada por mim e pelos membros da Comissão Examinadora.
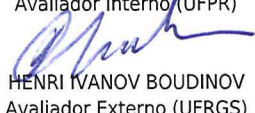Observações:_____
_____
_____

Curitiba, 15 de Dezembro de 2017.

IVO ALEXANDRE HUMMELGEN
Presidente da Banca Examinadora (UFPR)

CYRO KETZER SAUL
Avaliador Externo (UFPR)

JOSÉ PEDRO MANSUETO SERBENA
Avaliador Interno (UFPR)

HENRI IVANOV BOUDINOV
Avaliador Externo (UFRGS)

CARLOS CÉSAR BOF BUFON
Avaliador Externo (CNPEM)

TERMO DE APROVAÇÃO

Os membros da Banca Examinadora designada pelo Colegiado do Programa de Pós-Graduação em FÍSICA da Universidade Federal do Paraná foram convocados para realizar a arguição da Tese de Doutorado de **ALI NAWAZ**, intitulada: **"Modification of charge transport properties ind defect-free poly (3 -hexylthiophene - 2,5 - diyl) field-effect transistors"**, após terem inquirido o aluno e realizado a avaliação do trabalho, são de parecer pela sua _APROVAÇÃO_ no rito de defesa.
A outorga do título de doutor está sujeita à homologação pelo colegiado, ao atendimento de todas as indicações e correções solicitadas pela banca e ao pleno atendimento das demandas regimentais do Programa de Pós-Graduação.

Curitiba, 15 de Dezembro de 2017.

IVO ALEXANDRE HUMMELGEN
Presidente da Banca Examinadora (UFPR)

CYRO KETZER SAUL
Avaliador Externo (UFPR)

JOSÉ PEDRO MANSUETO SERBENA
Avaliador Interno (UFPR)

HENRI IVANOV BOUDINOV
Avaliador Externo (UFRGS)

CARLOS CÉSAR BOF BUFON
Avaliador Externo (CNPEM)

Dedicated to my beloved family;

Abu, Ami, Oumar and Usama

ACKNOWLEDGMENTS

The greatest challenge to any thinker is stating
the problem in a way that will allow a solution.

(Bertrand Russell)

RESUMO

O trabalho atual investiga a melhoria das propriedades de transporte de carga em transistores de efeito de campo de baixa tensão (FETs), que utilizam poli(3-hexiltiofeno-2,5-diil) (P3HT) não-100% e 100% regioregular como os semicondutores orgânicos, e poli(álcool vinílico) reticulado (cr-PVA) como isolante. O trabalho de pesquisa realizado durante o projeto pode ser dividido em duas partes. A primeira parte investiga a melhoria das propriedades de transporte de carga na interface cr-PVA/P3HT, e a influência de defeitos de regioregularidade de P3HT nas propriedades da interface. A segunda parte demonstra a preparação de filmes finos que consistem em moléculas alinhadas de P3HT 100% regioregular e, consequentemente, a aplicação desses filmes alinhados para o desenvolvimento de dispositivos de alto desempenho.

No caso da primeira parte, o problema essencial é que o transporte de carga na interface de cr-PVA/P3HT está limitado pela presença de armadilhas na interface que correspondem aos dipolos de superfície de cr-PVA. Esses dipolos de superfície possuem a capacidade de modificar a distribuição de carga em moléculas adjacentes de P3HT, o que pode levar à localização e a captura de cargas. Isso representa um problema fisico complexo, sendo que a variação de energia potencial na interface depende da posição e orientação das armadilhas dipolares em relação às moléculas de P3HT. No entanto, a solução é conceitualmente simples, pois, em princípio, é apenas necessário passivar as armadilhas. Para conseguir isso, é apresentada uma técnica experimental econômica, na qual a superfície de cr-PVA é tratada com um surfactante catiônico, brometo de hexadeciltrimetilamónio (CTAB). As cabeças hidrofílicas carregadas positivamente de CTAB visam a passivação das armadilhas carregadas negativamente da superfície de cr-PVA. A deposição de CTAB sobre o cr-PVA, em relação ao cr-PVA somente, resulta em aumento significativo na capacitância do isolanate (C_i), e as imagens de microscopia de força atômica (AFM) mostram que a superfície de cr-PVA é coberta com grãos de surfactante bem conectados. Em caso de dispositivos baseados em P3HT não-100% regioregular, este tratamento resulta em uma melhora da mobilidade de efeito de campo (μ_{FET}) por um fator de ~3 (μ_{FET} médio de 0.44 cm^2/V.s) quando comparado aos dispositivos não tratados. Para investigar como o tratamento do surfactante modifica o transporte de carga na interface, a variação de μ_{FET} em função da espessura efetiva do gargalo do canal (l_0) também é analisada e discutida detalhadamente.

Curiosamente, ao contrário dos dispositivos baseado em P3HT não-100% regioregular, o tratamento com surfactante em dispositivos baseado em P3HT 100% regioregular resulta em degradação de μ_{FET} e do desempenho geral dos dispositivos. Isso indica que a interação de defeitos de regioregularidade e armadilhas de superfície de cr-PVA é um fator crítico que afeta as propriedades de transporte de carga na interface cr-PVA/P3HT. Para investigar este assunto, a interação das moléculas de P3HT não-100% e 100% regioregular com dipolos de superfície de cr-PVA é investigada usando espectroscopia de absorbância, AFM e cálculos de química quântica. Observa-se que, dependendo da presença ou ausência de defeitos de regioregularidade de P3HT (e, portanto, da planaridade molecular), o contato entre as moléculas de P3HT e os dipolos de superfície de cr-PVA afeta a ordem molecular do P3HT de forma diferente. Por causa dos defeitos de regioregularidade, as moléculas de polímero não-100% regioregular produzem momentos de dipolo mais altos em comparação com moléculas 100% regioregular. Consequentemente, discute-se como a interação de moléculas de P3HT não-100% e 100% regioregular com dipolos de cr-PVA contribuem à desordem energética na interface cr-PVA/P3HT. Neste caso, o transporte de carga em dispositivos de FET é investigado para quatro espessuras diferentes de P3HT não-100% e 100% regioregular. Os resultados elétricos mostram que o comportamento de $\mu_{FET} \times l_0$ e a dependência de μ_{FET} na espessura do canal são uma função forte da presença ou ausência de defeitos de regioregularidade de P3HT.

Neste trabalho, os dispositivos (não tratados) baseados em P3HT 100% regioregular demonstram μ_{FET} tão alto quanto 1.20 cm^2/V.s. Esses valores tornam esses dispositivos reconhecíveis para a integração em várias aplicações comerciais. No entanto, um desenho de circuitos para muitas outras aplicações de alto desempenho impõem um requisito de μ_{FET} mais rigoroso (> 5 cm^2/V.s). Para alcançar este marco, na segunda parte do projeto de pesquisa, está apresentada uma técnica de deposição simples (chamado, floating–film transfer method, em inglês), que permite o alinhamento supra-molecular das moléculas de P3HT 100% regioregular. A aplicação de filmes de polímero alinhados em FETs resulta em valores de μ_{FET} de até 8 cm^2/V.s, que é o valor mais alto reportado até agora para os FETs baseados em P3HT.

Palavras-chaves: Transistores orgânicos de efeito de campo, poli(3-hexiltiofeno-2,5-diil) livre de defeitos, regioregularidade, poli(álcool vinílico) reticulado, interface isolante/semicondutor, armadilhas dipolares.

ABSTRACT

The current work investigates the improvement of charge transport properties in low-voltage organic field-effect transistors (OFETs) that utilize non-100% and 100% regioregular poly(3-hexylthiophene-2,5-diyl) (P3HT) as the organic semiconductors, and cross-linked poly(vinyl alcohol) (cr-PVA) as the gate insulator. The essential research work performed during the project can be divided into two parts. The first part investigates the improvement of charge transport properties at the cr-PVA/P3HT interface, and the influence of regioregularity defects of P3HT on interface properties. The second part demonstrates the development of high performance OFETs based on supra-molecularly aligned thin films of 100% regioregular P3HT.

In the case of the first part, the essential problem in hand is that charge transport at the cr-PVA/P3HT interface is limited by the presence of charge traps at the interface corresponding to the surface dipoles of cr-PVA. These surface dipoles hold the ability to modify charge distribution on adjacent P3HT molecules, which can lead to localization and trapping of otherwise mobile charge carriers. This presents a physically complex problem, since the potential energy variations at the interface depends on the position and orientation of the dipolar traps with respect to P3HT molecules. However, the solution is conceptually simple since, in principle, it is only required to passivate the traps. In order to achieve this, a cost-effective experimental technique is presented, in which the cr-PVA surface is treated with a cationic surfactant, hexadecyltrimethylammonium bromide (CTAB). The positively charged hydrophilic heads of CTAB are aimed at passivating the negatively charged traps of the cr-PVA surface. The deposition of CTAB over cr-PVA leads to significant enhancement in gate insulator capacitance (C_i), and the atomic force microscopy (AFM) images show that the cr-PVA surface is covered with well-connected surfactant grains. In the case of non-100% regioregular P3HT OFETs, this treatment results in an improvement of field-effect mobility (μ_{FET}) by a factor of ~3 (average μ_{FET} of 0.44 cm^2/V.s) when compared to untreated devices. In order to investigate how the surfactant treatment modifies charge transport at the interface, variation of μ_{FET} as a function of the effective bottleneck thickness of the conducting channel (l_0) is also analyzed and thoroughly discussed.

Quite interestingly, contrary to non-100% regioregular P3HT devices, the surfactant treatment in 100% regioregular P3HT devices leads to degradation of μ_{FET} and overall device performance. This indicates that the interaction of regioregularity defects and cr-PVA surface

traps is a crucial factor affecting charge transport properties at the cr-PVA/P3HT interface. In order to address this issue, the interaction of non-100% and 100% regioregular P3HT molecules with cr-PVA surface dipoles is investigated using UV-vis absorbance spectroscopy, AFM and quantum chemical calculations. It is observed that, depending on the presence or absence of regioregularity defects of P3HT (and thus the molecular planarity); the intimate contact between P3HT molecules and cr-PVA surface dipoles affects the molecular order of P3HT differently. Because of the regioregularity defects, the non-100% regioregular polymer molecules produce higher dipole moments compared to 100% regioregular molecules. Consequently, it is discussed how the interaction of non-100% and 100% regioregular P3HT molecules with cr-PVA surface dipoles contribute differently to the potential energy variations at the cr-PVA/P3HT interface. In this case, the charge transport in FET devices is investigated for four different thicknesses of both non-100% and 100% regioregular P3HT. The electrical results reveal that the behavior of $\mu_{FET} \times l_0$ and the dependence of μ_{FET} on channel thickness are a strong function of the presence/absence of the regioregularity defects of P3HT.

In this project, the untreated 100% regioregular P3HT devices demonstrate μ_{FET} as high as 1.20 cm^2/V.s. Such high values make these devices recognizable for translation to various commercial applications. However, the circuit designs of many other high performance applications impose a more stringent μ_{FET} requirement (> 5 cm^2/V.s). In order to achieve this landmark, in the second part of the research project, a simple and cost-effective deposition technique (floating–film transfer method) is presented, which allows supra-molecular alignment of 100% regioregular P3HT molecules. The application of aligned polymer films in FET devices leads to the demonstration of μ_{FET} values as high as 8 cm^2/V.s, which is the highest value reported so far for P3HT based OFETs.

Table of contents

1

Introduction

Transistors hold a fundamental importance in driving today's microelectronic industry, with the basic working principle of controlling the flow of electric current through a semiconductor. Following the discovery of the first transistor by Bardeen and Brattain in 1947 (Figure 1.1a) [1], the transistor technology witnessed a great deal of evolution and many different types of transistors were introduced to the microelectronics industry. One of these was the field-effect transistor (FET), which, although first reported as a practical application in 1960 [2], was initially proposed by Julius Edgar Lilienfeld in 1930 [3]. Since then, the FET technology has evolved dramatically, and presently FETs are being applied as one of the most important constituents of many electronic applications ranging from basic amplifiers to sensors and light emitting diode (LED) displays. In addition, the development of innovative flexible display technologies and applications are also being envisaged, for which the use organic materials in FET devices remain under extensive research [4–10]. In most of the cases organic FETs (OFETs) adopt the thin-film transistor (TFT) architecture; the semiconductor is sandwiched between the source and drain electrodes and isolated from the gate electrode by
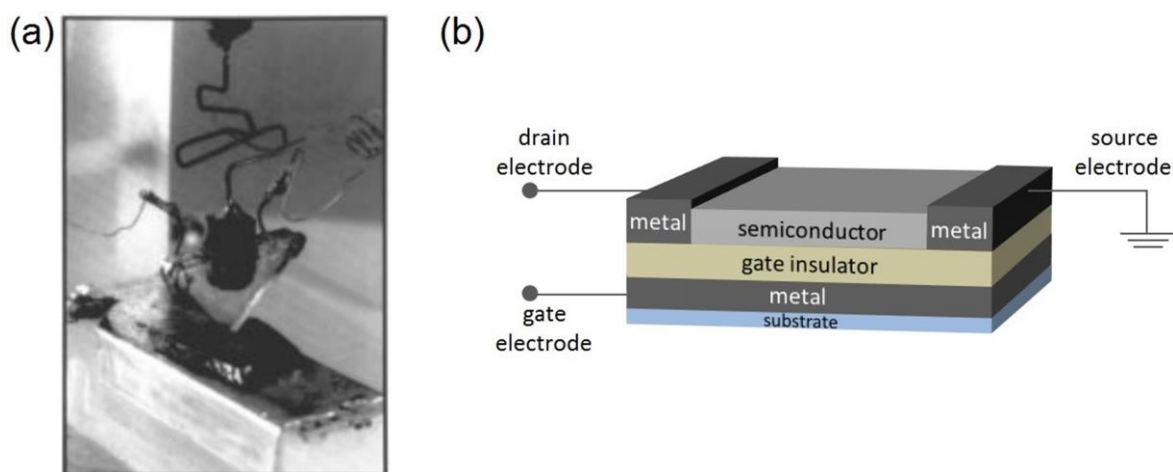
Figure 1.1 (a) The first transistor. The bottom electrode was the base of the germanium crystal. The other two electrodes were formed on the tip of the block above the germanium crystal [188], and; (b) typical OFET structure in TFT architecture.

the insulator (Figure 1.1b). The application of a voltage between the gate and the source electrode modulates the density of charge carriers in the semiconducting channel. Simultaneous application of a second voltage between the source and the drain electrode results in the flow of current in the channel [11].

What makes OFETs attractive for current electronic applications is that all the layers can be deposited at low/room temperatures using low-cost solution-processable methods, and that most of the organic semiconductors exhibit a degree of mechanical flexibility [11]. On the other hand, inorganic semiconductors like silicon (Si) are rigid materials and require high processing temperatures [12]. Although techniques have been introduced to transfer polycrystalline Si TFTs onto flexible substrates, these require costly and complicated fabrication steps [13]. For this reason, there is now a serious level of industrial interest in using OFETs for future applications like rollable, bendable or foldable color displays (Figure 1.2) that are inconceivable with the use of Si or other inorganic semiconductor technologies [14]. The performance of OFETs has already surpassed that of amorphous Si (a-Si) TFTs [15,16], and, in some cases, compete with polycrystalline Si TFTs [17]. In terms of field-effect mobility of charge-carriers (μ_{FET}) of OFETs, values as high as 43 cm^2/V.s in the case of molecular crystals [17] and 24 cm^2/V.s in the case of conjugated polymers [18] have already been reported.

Conjugated polymers are a distinct category of organic semiconductors which, in fact, demonstrate superior properties than molecular crystals in terms of cost-effectiveness and flexibility [19,20]. Not too long ago, conjugated polymers were considered as electrically

Figure 1.2 Projected trend of the flexible-display technology from a curved device to future flexible devices, such as rollable and foldable displays, that offer many potential advantages, *e.g.* very thin profiles and lightweight display systems.

insulating materials, until the conducting properties (due to the presence of loosely bound π–electrons) in polyacetylene (PAc) were discovered in 1977 [21] (PAc was first synthesized in 1974 [22]). Conjugated polymers essentially tend to be insoluble [23], and hence, following the discovery of conducting properties in conjugated polymers, there were serious concerns whether or not processing methods could be developed [23]. Indeed, significant progress was made in this area and many approaches were developed to overcome this challenge [23]. One of these was the side-chain functionalization which decreases the interchain coupling and increases entropy thus rendering conjugated polymers soluble in organic solvents. The addition of moderately long side chain onto the monomer units of conjugated polymers resulted in a variety of processable semiconducting polymers [23].

Among conjugated polymers, polythiophene derivatives have emerged as effective semiconducting materials mainly due to their solution processability and ability to self-organize into highly crystalline structures. The application of polythiophene derivatives in OFET devices has led to the demonstrations of some of the highest reported μ_{FET} values in polymer based OFETs [24–27]. One particularly interesting example of polythiophenes is poly(3-hexylthiophene-2,5-diyl) (P3HT), since it is widely available, it has a simple chemical structure (Figure 1.3) that crystallizes easily, it is soluble in various organic solvents [28], and it demonstrates efficient electronic properties [29]. Due to these advantages extensive research efforts have been dedicated over the past ~25 years towards understanding and improving the crystalline structure of P3HT [30–37]. Much like other polythiophenes, the order in P3HT films is, to a great extent, dependent on its regioregularity which determines the extent of the delocalization of π–electrons [19]. In 2012, the synthesis and detailed characterization of chemically defect-free 100% regioregular P3HT (DF-P3HT) was reported for the first time by Kohn *et al.* [38]. However, no further initiative was taken towards the application of DF-P3HT to OFETs, yet this could be a viable alternative to achieve better device performance
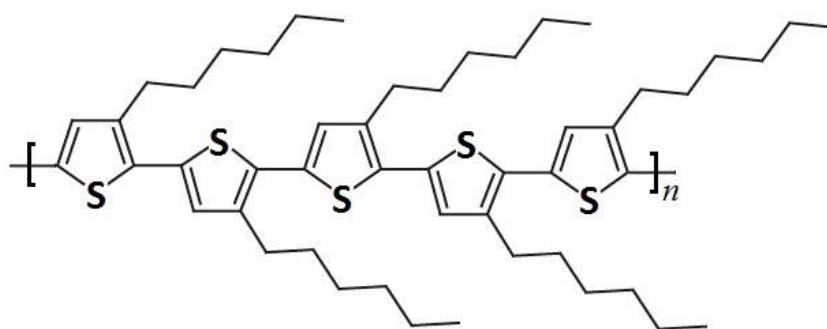
Figure 1.3 Chemical structure of P3HT.

without the use of expensive and complicated experimental techniques. Indeed most of the publications on "high" performance non-100% regioregular P3HT based OFETs typically report μ_{FET} values < 0.5 cm^2/V.s [39–48]. These values may be sufficient for driving the backplane circuitry of applications like liquid crystal displays (where μ_{FET} > 0.1 cm^2/V.s is required [49]), however, they are far from the requirement of modern high-speed applications such as organic LED (OLED) displays. Each pixel of an OLED display is driven by 2-4 OFETs, and the required μ_{FET} to operate the pixel at a sufficient speed could be as high as 5-10 cm^2/V.s [16]. Another disadvantage related to the majority of reports on P3HT based OFETs is the incorporation of inorganic materials (such as SiO$_2$) as the gate insulator layer [28,31,50]. Although SiO$_2$ demonstrates good insulating properties, it is difficult to implement it to soft electronics due to its rigidity. In addition, because of the relatively low dielectric constant of SiO$_2$ ($\kappa = 3.9$ [51]), the corresponding OFET devices have to be operated at high voltages (typically above 20 V) [28,31,50]—which restricts their use in low power applications, *e.g.*, large-area sensors [52].

This thesis deals with the performance enhancement of low-voltage OFETs prepared with non-100% and 100% regioregular P3HT as the organic semiconductors, and cross-linked poly(vinyl alcohol) (cr-PVA) as the organic gate insulator. The use of cr-PVA is justified because of its high dielectric constant ($\kappa \sim 7$ [53]), bio-degradability and mechanical flexibility. However, the surface of cr-PVA has charge traps that cause degradation of charge transport properties at the cr-PVA/P3HT interface. Hence, a detailed study is presented that investigates the effect of the interaction of non-100% and 100% regioregular P3HT molecules with cr-PVA surface traps, and its influence on charge transport at the interface. In order to passivate the cr-PVA surface traps and consequently improve charge transport properties at the interface, a simple, cost-effective and environmentally friendly treatment is presented using a cationic surfactant. In this context, it is demonstrated how regioregularity defects of P3HT influence the final outcome of this treatment. Finally, a simple technique (floating–film transfer method) is used that allows molecular alignment in polymeric films. The application of this technique in 100% regioregular P3HT based FETs leads to μ_{FET} values as high as 8 cm^2/V.s.

2

Organic semiconductors, insulators and field-effect transistors: a theoretical background to the physical problem

2.1 Organic Semiconductors

The term *organic semiconductors* denotes materials that 1) mostly comprise of carbon and hydrogen atoms, and a small amount of heteroatoms such as, oxygen, sulfur and nitrogen, and; 2) show a degree of electrical conductivity sufficient for the operation of classical semiconductor devices such as field-effect transistors (FETs), light-emitting diodes (LEDs) and solar cells [14,54]. Organic semiconductors can be distinguished into the following three types:

1) *Amorphous organic semiconductors* are non-crystalline materials that are characterized by a completely disordered molecular packing, which lacks long-range order [54]. They can be deposited through spin coating or thermal evaporation for device applications like LEDs or xerography [54].

2) *Conjugated polymers*, such as poly(3-hexylthiophene-2,5-diyl) (P3HT), are polycrystalline materials that consist of large number of small crystals, called crystallites. Molecular chains in these crystallites are covalently coupled and form repeat units in a pattern. However, this pattern may change abruptly at chain ends or crystal boundaries, and crystals may be separated by amorphous regions. Nevertheless, conjugated polymers form relatively long-range molecular order compared to amorphous materials. Conjugated polymers are usually processable from solution, which allows deposition from a range of techniques including ink-jet deposition, spin coating or industrial reel-to-reel coating [54].

3) *Molecular crystals* such as naphthalene or anthracene consist of a crystal and a basis held together by van-der-Waals interactions [54]. The molecules form patterns that periodically repeat in space without change in composition, orientation or dimension. For this reason, charge-carrier mobilities in molecular crystals are much higher when compared to non-crystalline or poly-crystalline materials [54].

2.1.1 Electronic structure and charge transport

The electronically important constituent of any organic semiconductor is the carbon atom. In the case of ethene, for instance, a double bond is formed between two carbon atoms (Figure 2.1a). The three electrons occupying the in-plane sp^2–hybridized orbitals directly interact to form σ–bonds, while the non–hybridized $2p_z$–orbitals, perpendicular to the plane, interact to form the π–bonds (Figure 2.1a). The electrons occupying the σ–bond are mainly localized along the path linking the two atomic nuclei, whereas, the π–electrons are much more loosely bound.

If the carbon atoms combine together to form larger molecules, typically with benzene as the basic unit, the π–electrons delocalize over the entire molecule to form a π–conjugated system (Figure 2.1b) [55]. Consequently, the energy levels associated with all of the contributing π–orbitals form the frontier orbitals, highest occupied molecular orbital (HOMO), and lowest unoccupied molecular orbital (LUMO) [56]. The HOMO/LUMO levels play the role of valence and conduction bands, respectively, found in perfectly crystalline systems [56]. The energy separation between HOMO–LUMO is the energy band gap (E_g); the energy required to remove an electron from the HOMO to the vacuum level is the ionization potential (*I.P.*), and; the energy required to add an electron to the LUMO is the electron affinity (χ). The electronic structure of organic semiconductors differs from their inorganic
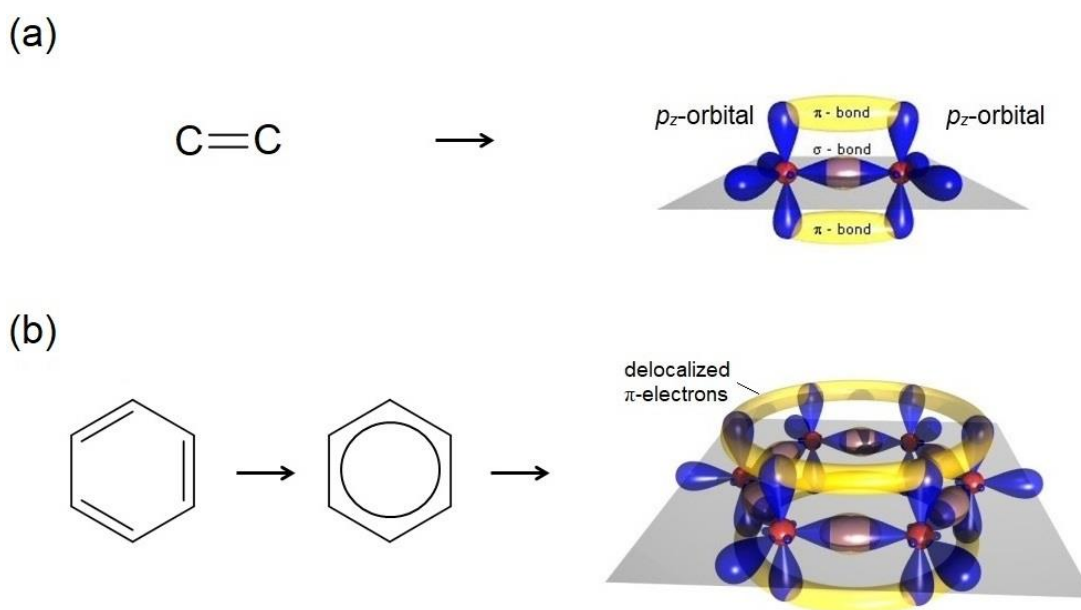
Figure 2.1 (a) Illustration of the formation of σ– and π–bonds in ethene, and; (b) illustration of the delocalization of π–electrons in benzene.[1]

---

[1] www.orgworld.de

counterparts principally by the nature of bonding. Although strong covalent bonds exist along the chain of molecules, however, inter–chain bonding in organic semiconductors takes place through considerably weaker van der Waals forces[2]. This results in a much weaker delocalization of electronic wavefunctions among neighboring chains.

In the case of conjugated polymers, the repeating unit (*mer*) is often based on a five– or six–membered carbon ring system (aromatic ring). The local arrangement of carbon atoms in the aromatic ring can be altered by, *e.g.*, incorporating heteroatoms, or the hydrogen atoms can be substituted by side groups (alkyl chains) to allow solubility with common organic solvents [54]. Some examples of conjugated polymers are shown in Figure 2.2. Electron delocalization along a chain of *mers* (or polymer backbone) occurs because of the overlapping π–orbitals of carbon atoms. In a hypothetical, infinitely planar polymer chain, the HOMO and LUMO states are fully delocalized along the polymer chain. However, in practice, polymer chains usually suffer from conformational disorders, owing to the fluctuations in torsional (dihedral) angles between neighboring aromatic rings. Consequently, the polymer chains exhibit deviations from planar conformations, which strongly limits the electron delocalization by decreasing the overlap between π–orbitals of adjacent rings[3] [57].
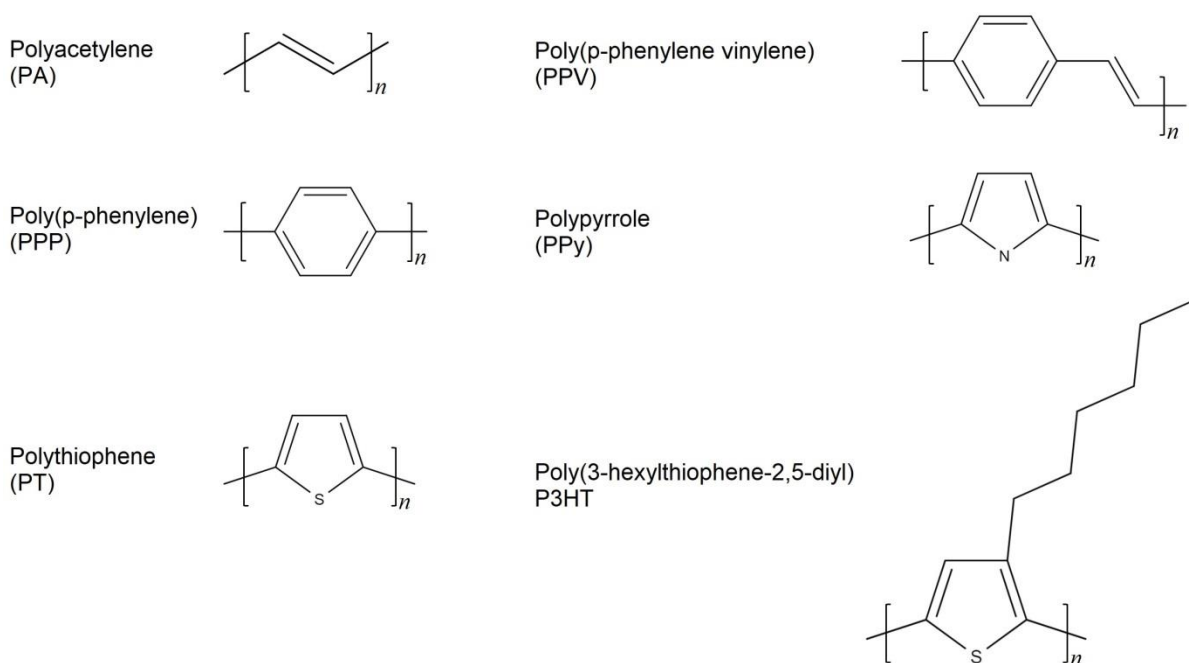
Figure 2.2 Chemical structures of few conjugated polymers.

---

[2] The electrostatic interaction between the correlated fluctuating dipoles in two molecules results in an attractive
[3] Electron delocalization in most polymers is usually limited to ~20 *mers* [54].

Deviations of torsional angles can be small, *e.g.*, up to ~20° due to the incorporation of alkyl chains [57] or due to steric interactions between hydrogen atoms [59], which may only have a little effect on the electronic properties of polymers. However, large deviations of torsional angles break the symmetry of the π–conjugation along the polymer chain, practically dividing the chain into distinct segments of equal or unequal lengths (Figure 2.3). One of the most serious cases is the inclusion of synthesis related chemical defects within the polymer chains. These defects are sometimes attributed to the unfavorable couplings between adjacent aromatic rings. In such cases, the interaction between heteroatoms and alkyl chains, or the interaction between alkyl chains of the neighboring *mers* cause large deviations in the torsional angles between adjacent aromatic rings [60].

As a consequence of structural irregularities in conjugated polymers, largely caused by the deviations of torsional angles, two types of disorders are usually discussed, namely, energetic and positional disorders [61]. When a conjugated polymer is deposited as a thin film, the solid structure consists of a distribution of polymer chains held together by weak van der Waals forces [61]. The torsional disorder produces fluctuations in conjugation lengths, which, in turn, results in fluctuations in the HOMO and LUMO energies of the π–conjugated
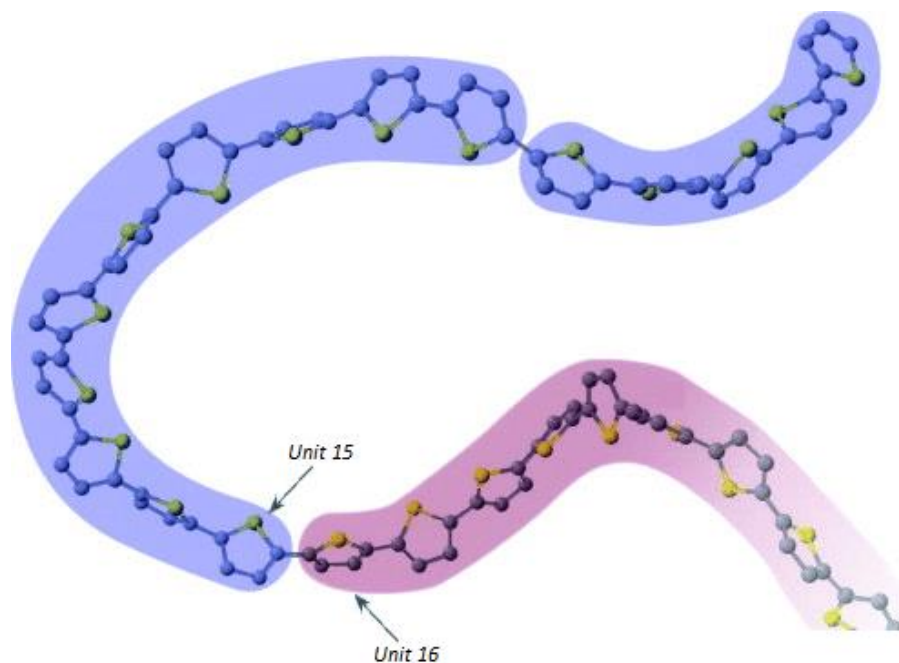
Figure 2.3 Part of a typical polythiophene chain. The torsional angle between thiophene units 15 and 16 is ~90 °. Therefore, the π–electron overlap is negligible between these units, causing a break in the π–conjugation symmetry. The blue and red envelopes are schematic representations of the localization of charge carriers on either side of the conjugation break [58].

segments. In addition, the polarization effects from surrounding chains add to the energy fluctuations of the π–conjugated segments. The resulting disorder is referred to as the energetic disorder [61]. On the other hand, the fluctuations in the orientations and inter–chain distances (due to torsional angles) can result in strong fluctuations in the inter–chain electronic overlap [61]. The resulting fluctuations in the strength of electronic interactions between polymer chains characterize the positional disorder, which limits electron delocalization in the inter–chain direction.

The electronic structure of conjugated polymers can be considered as a complex interplay between the intrinsic π–electron delocalization along the polymer backbone, and the presence of energetic and positional disorder in polymer thin films. Most polymers typically exhibit both types of disorders [61]. The essential effect of disorder is to cause 1) fluctuations in the energy of π–conjugated segments; 2) fluctuations in the density or mean inter–chain distance, and; 3) absence of long-range order. Consequently, the energetic environment of all the segments within the solid differs, thereby splitting the electronic bands into manifolds of localized states randomly distributed in energy and space [62].

Because of the disorder-induced strong energy fluctuations, the molecular sites in polymer thin films are no longer represented as a discrete level of energy, ε, but as an energy distribution, $N(\varepsilon)$, as illustrated in Figure 2.4. The corresponding density of localized sites is described by a Gaussian distribution (commonly termed as the Gaussian density of states (DOS, Figure 2.4) [61,63–66]. The flow of charge carriers between these localized sites follow the mechanism of *hopping* transport (through uncorrelated jumps), rather than the mechanism of band transport common for conventional high conductivity inorganic semiconductors. According to the hopping process, charge carriers are transported by thermal activation between the localized molecular sites. In this context, the charge carriers found in a particular site can absorb or emit vibrational energy (phonon), and jump to a neighboring site [67,68]. Hopping transport is favored by the majority of localized sites located in the centers of the Gaussian distributions (forming a transport level) [66]. However, the sites located in the bottom part (tail) of the Gaussian distributions are strongly localized, acting as traps [66]. The charge carriers found in these sites require a much higher energy to be promoted to the transport level. The presence of tail sites is a strong limitation to charge transport properties in organic semiconducting materials.
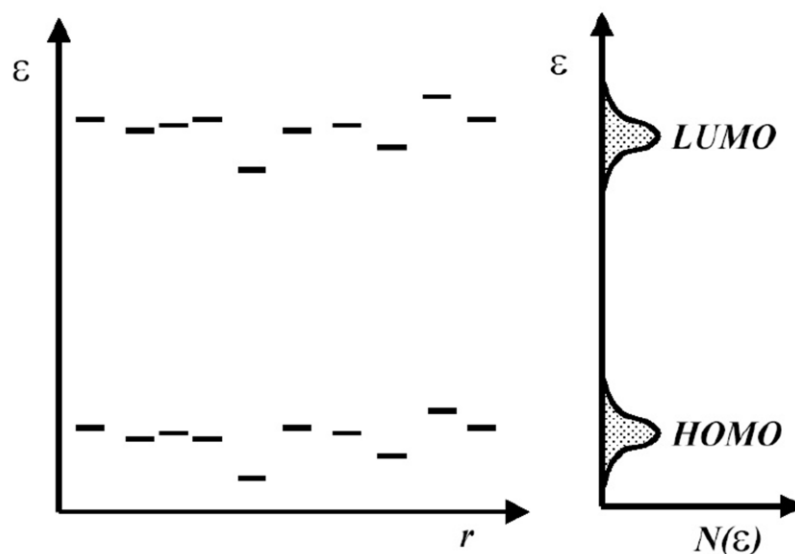
Figure 2.4 Localized molecular sites randomly distributed in energy (as a function of distance, *r*) in a conjugated polymer film. The statistical function that describes the probability-distribution of localized sites in HOMO/LUMO is the Gaussian distribution [61,63–66].

2.2 Poly(3-hexylthiophene-2,5-diyl)

Poly(3-hexylthiophene-2,5-diyl) (P3HT) was used as the principal organic semiconducting material in this project for the development of organic field-effect transistors (OFETs). P3HT is one of the most investigated conjugated polymers [30–37], because of its various advantages, including solution-processability, non-toxicity, extended π–conjugation system, and relatively superior chemical and electronic properties [54]. The chemical structure of a P3HT *mer* consists of a five-membered thiophene (aromatic) ring with alternating single and double carbon bonds. The aromatic ring is attached to an insulating alkyl side chain. The *mer* units covalently bond with adjacent units which successively repeat to form a conjugated chain. Regioregularity of P3HT is dependent on the relative position of the side chains, which, may be connected to position 3 or 4 (Figure 2.5) [54]. For instance, if the side chain is always at the same position (say 3), and the repeat units are always connected from position 2 on one ring to 5 on the next (called 2,5" or head-to-tail), a regioregular P3HT structure is formed, where all side chains point in the same direction [54]. Other combinations such as 2,2" ("head-to-head") or 5,5" ("tail-to-tail") lead to structures with irregular side chain directions, referred to as irregioregular P3HT structure (Figure 2.5b) [54]. The atomic positions of aromatic ring are shown in Figure 2.5c-e.
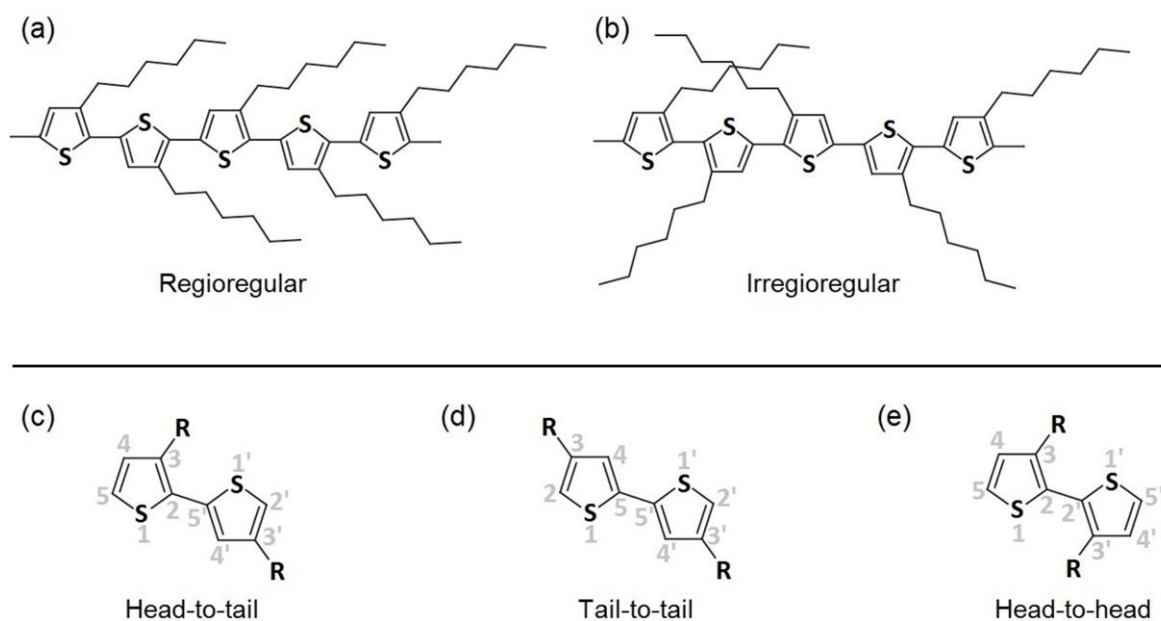
Figure 2.5 P3HT coupling ring connections showing (a) regioregular structure formed when all connections are head-to-tail, while; (b) irregioregular structure formed otherwise; (c) head-to-tail; (d) tail-to-tail, and; (e) head-to-head configurations. The numbering of the atoms is shown in grey [54].

P3HT in its solid state consists of a distribution of crystalline and amorphous regions [69]. The degree of crystallinity, however, depends on the regioregularity of the polymer, which is influenced by the molecular chemistry [70]. Low regioregular or irregioregular P3HT usually suffers from synthesis related chemical defects along the polymer chains. These defects induce higher torsional angles between adjacent *mer* units. The first effect is the decrease in π–conjugation lengths, and the second effect is that the polymer chains partially adopt an orientation parallel to the substrate (face-on orientation, Figure 2.6a). As a further consequence, the steric interactions between the side chains of neighboring molecules prevent close packing of the polymer chains. Hence, low regioregular P3HT suffers from low degree of delocalization in both intra– and inter–chain directions, and high degree of both energetic and positional disorders [54].

As the regioregularity of P3HT increases, through chemical elimination of coupling defects along polymer chains, lower torsional angles between adjacent units are obtained. This leads to the formation of well-stretched polymer chains with high degree of π–conjugation. The *mer* units adopt a coplanar conformation which allows close intermolecular organization between adjacent polymer chains [54]. The outcome is the realization of sheet like structures with face-to-face stacking of aromatic rings, vertically separated by the side chains, in a molecular orientation perpendicular to the substrate (edge-on orientation, Figure
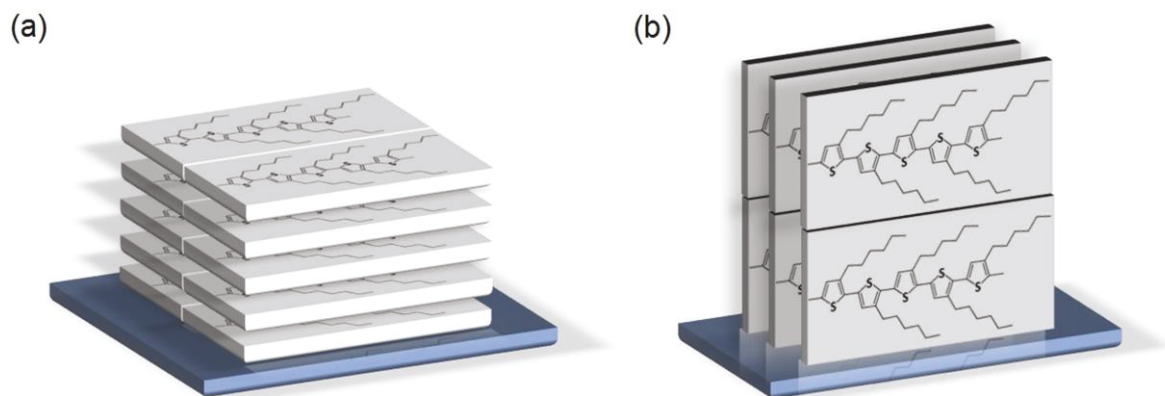
Figure 2.6 Illustrations of (a) parallel (face-on), and; (b) perpendicular (edge-on) orientations of P3HT molecules.

2.6b) [54]. Hence, high regioregularity in P3HT allows relatively higher degree of delocalization in both intra– and inter–chain directions, and relatively lower degree of both energetic and positional disorders.

2.2.1 Synthesis of defect-free poly(3-hexylthiophene-2,5-diyl)

The synthesis of P3HT was first reported by McCullough *et al.* in 1992 [71]. They used 1,3-bis[diphenylphosphinopropane]nickel(II) chloride (Ni(dppp)Cl$_2$) as the catalyst to generate P3HT. In 1992, and subsequently in 1995, Reike *et al.* also reported synthesis of P3HT by using a polymerization method; 2,5-dibromo-3-hexylthiophene was reacted with activated Rieke zinc to generate the organozinc derivative, which was further reacted with Ni(dppp)Cl$_2$ to generate P3HT [72,73]. In 1999, McCullough *et al.* developed the Grignard metathesis (GRIM) polymerization (also known as Kumada catalyst-transfer polycondensation (KCTP)), aiming at large-scale synthesis of P3HT [74].

Although the GRIM method has been widely used for polymer synthesis, the polydispersity as well as batch-to-batch reproducibility are difficult to control because of the very high polymerization rate and insolubility of Ni(dppp)Cl$_2$. In order to overcome these issues, in 2013 Bannock *et al.* proposed the use of a continuous-flow tube reactor as an alternative method [75], which could be used for the synthesis of a range of conjugated polymers [76,77] and fullerene derivatives [78]. Bannock *et al.* dispersed Ni(dppp)Cl$_2$ in perfluoropolyether suspensions and used droplet-based microreactors to synthesize P3HT [75]. Consequently, high regioregularity (> 98%) and high molecular weight ($M_n \sim 30$ kDa) was achieved.

Further improvements in the continuous-flow method were reported by Kumar *et al.* in 2014 [79], who used 3,4-ethylenedioxtyhiophene (EDOT) as an inert solvent for dissolving Ni(dppp)Cl$_2$. This method provided ultrafast polymerization times (~2 min), high throughput (32.8 g per channel per hour) and good batch to batch reproducibility (yields up to 70%) [79]. However, because of the use of Ni(dppp)Cl$_2$ as the catalyst, a tail-to-tail (TT) coupling defect was inevitably incorporated into the polymer chains. The inclusion of TT defect in the polymer chain essentially results in reduction in the planarity of the polymer backbone and breaks the conjugation of head-to-tail segments [38]. Recent studies show that the TT defect originating from the catalyst structure could be located anywhere within the linear P3HT chain [38,80]. Therefore even partial inclusion of this defect can have strong influence on the overall microstructure and crystallinity. In order to eliminate the effect of Ni(dppp)Cl$_2$ on the final structure of the polymer, Kumar *et al.* reported an improved continuous-flow synthesis method in 2016, wherein, Ni(II) was converted to Ni(0) to obtain 100% regioregular defect-free P3HT (DF-P3HT) [81].

The DF-P3HT synthesized by Kumar *et al.* was utilized in this project for the fabrication and characterization of thin films and transistor devices. Detailed synthesis and structure characterization is provided in [81]. Briefly, the traditionally used catalyst (Ni(dppp)Cl$_2$) was suspended in tetrahydrofuran under nitrogen blanket. To this, isopropylmagnesium chloride was added, finally resulting in the complete conversion of Ni(II) to Ni(0). Subsequently, a solution of 2-bromo-3-hexyl-5-thineylmagnesium chloride was added which resulted in the immediate formation of dark red/brown color solution. After further stirring for 30 min at room temperature, the final purified polymer was obtained as a thick film with green metallic luster [81,82]. This synthesis method resulted in the complete exclusion of the TT defect and DF-P3HT with high molecular weights (M_n > 70 kDa) could be synthesized.

2.3 Organic gate insulators

The choice of organic gate insulator for OFET devices is critical since the insulator/semiconductor (I/S) interface constitutes the region where effective charge transport occurs. The surface properties of gate insulator can largely influence the chemical and electronic properties of the semiconductor, and consequently important OFET characteristics. Hence, the preparation of high performance devices imposes rigorous requirements towards the choice of the gate insulator material. Among other characteristics, a gate insulator is required to have a high dielectric constant (κ), such that high capacitance and high charge

carrier densities can be obtained at low operating voltages. This is evident in Equation 2.1; capacitance per unit area (C_i) of a parallel-plate capacitor is directly proportional to the dielectric constant of the insulator [83]:

$$C_i = \varepsilon_0 \left(\frac{\kappa}{d}\right),$$
(2.1)

where, ε_0 is the vacuum permittivity (8.85×10^{-12} F/m), and d is the thickness of the gate insulator. It can be seen that C_i is also inversely proportional to the thickness of the insulator, which implies that, in order to obtain high charge carrier densities at low operating voltages, the insulator should be as thin as possible.

2.3.1 Cross-linked poly(vinyl alcohol)

Among other organic insulators—such as polypropylene ($\kappa = 2.1$), polyisobutylene ($\kappa = 2.2$), poly(methylmetacrilate) ($\kappa = 3.5$) and poly(vinyl phenol) ($\kappa = 4.5$) [84]—poly(vinyl alcohol) (PVA) is an effective choice because of its high κ (~ 8), solubility in water, non-toxicity, bio-degradability, cost-effective availability and mechanical flexibility [53,85,86]. Despite these advantages, PVA also has some disadvantages (like high hydrophilicity and high density of dipolar hydroxyl groups [53,86]) associated to its chemical structure (Figure 2.7a). The dipoles act as defects in the conducting channel of OFETs when PVA is used as the gate insulator layer [53] (this point will be discussed in detail in Section 2.5.1). Cross-linking of PVA with different chemical compounds (such as, ammonium bichromate [87], ammonium dichromate [10,53,86,88,89] and glutaraldehyde [90]) has proven to be an effective strategy to improve its insulating properties. In principle, cross-linking process is known to promote better inter–connections between the PVA chains [53], and at the same time, it significantly reduces the density of hydroxyl groups by conversion to other ether groups [89]. In addition, it also allows preparation of low roughness, low thickness/high capacitance films, and enhances immunity against moisture and solvent [53,91]. In this project, the cross-linking of PVA was performed using ammonium dichromate (AD, Figure 2.7b), following the optimal conditions reported by Benvenho *et al.* [53]. The dielectric
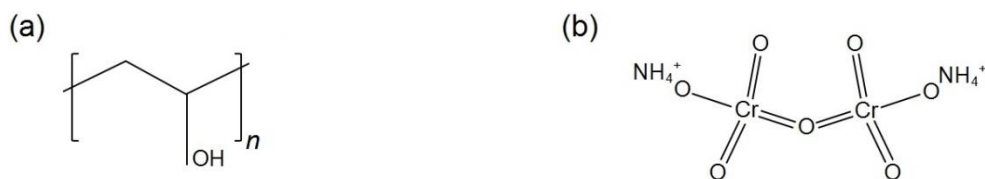
Figure 2.7 Chemical structures of (a) PVA, and; (b) ammonium dichromate (AD).

constant of cross-linked PVA (cr-PVA) was reported as ~7 [53], wherein the slight decrease of κ was attributed to the decrease in the density of hydroxyl groups [89].

Despite the fact that significant improvement of the insulating properties of PVA was obtained after the cross-linking process, it was observed that complete elimination of hydroxyl groups and water molecules is not achievable [53,86]. In fact, the cross-linking of PVA with AD was reported to result in the formation of dipolar ketone groups [53,92,93]. The presence of dipolar groups on the surface of cr-PVA has been electrically detected using capacitance measurements and admittance spectroscopy [53,86].

2.4 Organic field-effect transistors

2.4.1 Working principle

Figure 2.8 shows two commonly used geometries for the fabrication of OFET devices. Essentially, an OFET consists of a very thin organic semiconducting layer, sandwiched between two electrodes (source and drain), and isolated from a third electrode (gate) using an insulator layer. In effect, the insulator sandwiched between the semiconductor and gate forms a parallel-plate capacitor.

The idea of an OFET is to modulate the flow of current in the semiconductor between the source and drain electrodes, by applying a voltage to the gate electrode. In the case of a *p*-type semiconductor, the application of negative voltage between the gate and the source (V_{GS}) leads to accumulation of positive charges (holes) at the I/S interface. The density of accumulated charges is proportional to V_{GS} and the capacitance per unit area (C_i) of the gate insulator. However, not all accumulated charges are mobile, and first the traps need to be filled before additionally accumulated charges can become mobile. In other words, a V_{GS} has to be applied, which is higher than the threshold voltage (V_T). Once a substantial amount of mobile charge carriers are accumulated, it is said that a „conducting channel" is formed. If
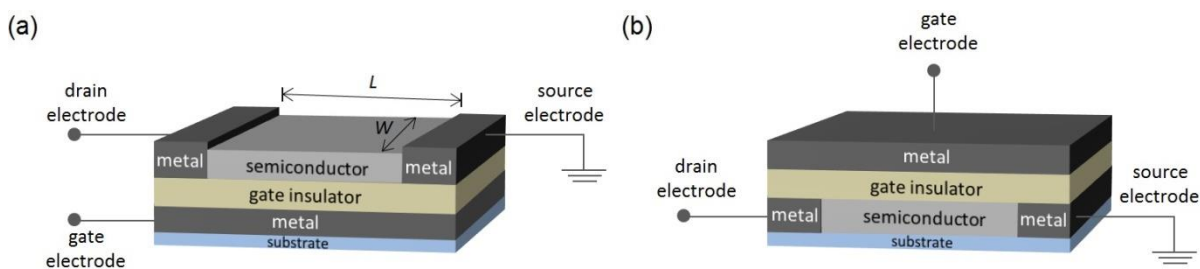
Figure 2.8 Schematic structures of (a) bottom-gate top-contact, and (b) top-gate bottom-contact OFETs in TFT architecture; *L*: channel length, *W*: channel width.

now a potential difference is applied between the source and the drain (V_{DS}), the mobile charge carriers flow in the semiconductor producing a drain current, I_D [6,94,95].

In order to obtain favorable charge transport in the conducting channel of OFET, optimal charge injection from the metal electrode, into the semiconductor, is required. In this context, the contact between metal and the semiconductor critically determines the charge injection properties. In OFET devices, such a contact is typically ohmic since the bulk resistance of organic semiconductors is much higher than that of the metal contact. Then, the contact acts as a reservoir of charge carriers [55]. The injection of holes into a *p*-type semiconductor requires the electrochemical potential (E_{Fm}) of the metal to be energetically close to the HOMO level of the semiconductor [19]. For instance, for injection of holes into P3HT (HOMO: ~ -5 eV; LUMO: ~ -3 eV), gold (Au) with E_{Fm} ~ -5.1 eV is an appropriate choice. On the other hand, the injection of electrons from Au into P3HT is unlikely since the LUMO of P3HT is energetically quite far from the E_{Fm} of Au (Figure 2.9).

Basic operating regimes of an OFET are illustrated in Figure 2.10, where three cases will be discussed. First a linear regime appears for a large V_{GS} and a small V_{DS} ($< V_{GS} - V_T$) is applied. The accumulated charge per unit area is almost uniform throughout the channel and I_D is proportional to V_{DS}. As V_{DS} is further increased, the voltage drop over the gate insulator and the semiconductor becomes a function of the position in the channel. When $V_{DS} = V_{GS} - V_T$, the voltage drop at the drain decreases, and provides a lower charge density in this region. Therefore, the accumulation layer near the drain electrode changes to a depletion layer, and the channel is said to be *pinched off* at the drain (Figure 2.10b). At the *pinch-off*, the channel depth at the drain reduces to zero. Further increase in V_{DS} ($V_{DS} > V_{GS} - V_T$) results in the
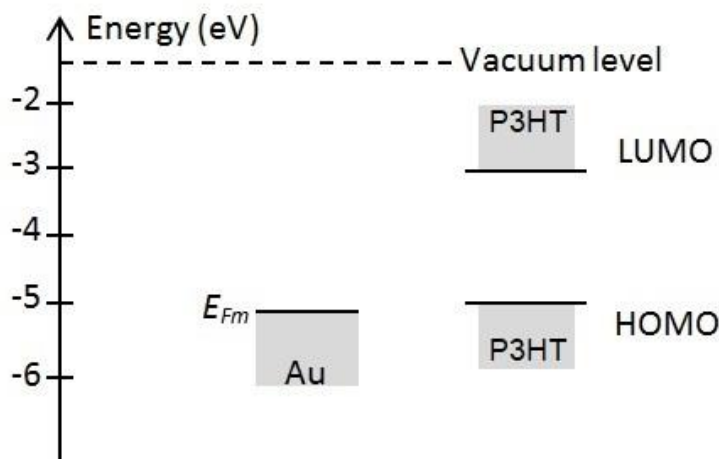
Figure 2.9 Energy diagram of the Au-P3HT interface [96–99].

expansion of the depletion region; the *pinch-off* point moves towards the source. The *pinch-off* region acts as a resistance to the charge transport, and the current saturates at a level I_{Dsat}. In the saturation regime, I_{Dsat} becomes independent of V_{DS} (Figure 2.10c) [6,100,101].

2.4.2 Current-voltage characteristics

The current-voltage characteristics of OFETs are typically interpreted according to the model developed for conventional metal-insulator-semiconductor FET (MISFET) devices [6]. However, the Equations quantifying the current-voltage characteristics of OFETs can also be derived in a few simple steps. Using the surface-charge notation [102], the current flow between the source and drain electrodes is given by:
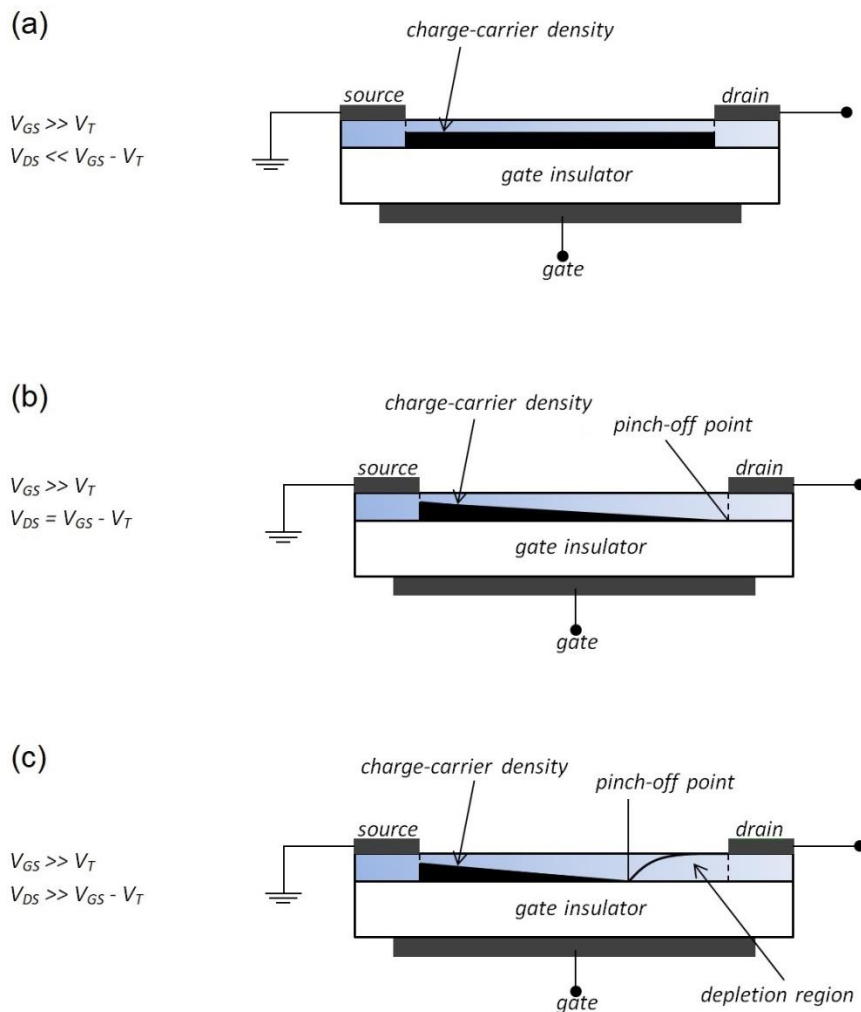
Figure 2.10 Schematic illustration of the operating regimes of an OFET; (a) linear regime; (b) start of the saturation regime at *pinch-off*, and; (c) saturation regime [83,101].

$$I_D = W\mu_{FET}Q\frac{dV}{dx}, \tag{2.2}$$

where, W is the channel width, μ_{FET} is the charge-carrier mobility, Q is the surface charge of free carriers injected from the electrodes, and $V(x)$ is the potential at position x from the source. Q is given by the capacitance per unit area of the gate insulator (C_i), which depends on the potentials (V_{GS}, V_T and $V(x)$). Equation 2.2 takes the form:

$$I_D = W\mu_{FET}C_i(V_{GS} - V_T - V(x))\frac{dV}{dx} \tag{2.3}$$

By making simple re-arrangements to Equation 2.3, we get:

$$\frac{I_D}{W\mu_{FET}C_i} = (V_{GS} - V_T - V(x))\frac{dV}{dx} \tag{2.4}$$

$V(x)$ starts from zero at the source electrode and reaches V_{DS} at the drain electrode. If L is the channel length (the distance between the source and drain electrodes), and the potentials at source and drain are $V(0) = 0$ and $V(L) = V_{DS}$, respectively, integrating Equation 2.4:

$$\frac{I_D}{W\mu_{FET}C_i}\int_0^L dx = \int_0^{V_{DS}}(V_{GS} - V_T - V(x))\,dV, \tag{2.5}$$

$$\frac{I_D}{W\mu_{FET}C_i}L = (V_{GS} - V_T)V_{DS} - \int_0^{V_{DS}}V(x)\,dV, \tag{2.6}$$

$$\frac{I_D}{W\mu_{FET}C_i}L = (V_{GS} - V_T)V_{DS} - \frac{1}{2}V_{DS}^2, \tag{2.7}$$

$$I_D = \frac{W\mu_{FET}C_i}{L}\left[(V_{GS} - V_T)V_{DS} - \frac{1}{2}V_{DS}^2\right] \tag{2.8}$$
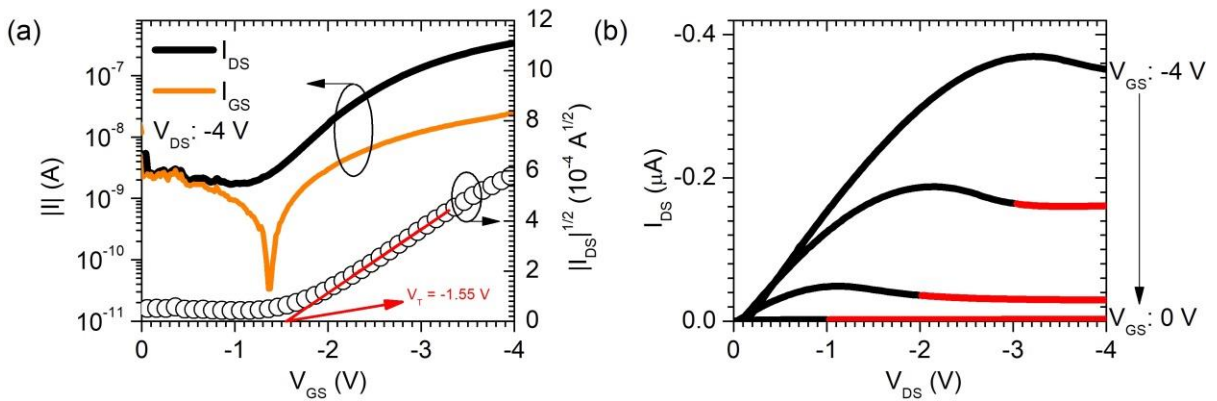
Figure 2.11 Typical electrical characteristics of a cr-PVA/P3HT based OFET device with $L = 100$ μm, $W = 2$ mm and $C_i = 17$ nF/cm^2; (a) $I_D \times V_{GS}$ in black solid line, $I_G \times V_{GS}$ in orange solid line, and linear best-fit plot in white open symbols (V_T = threshold voltage), and; (b) output curves ($I_D \times V_{DS}$) where black lines show the linear regime and the red lines show the saturation regime.

For $V_{DS} > V_{GS} - V_T$ (linear regime), Equation 2.8 beomes:

$$I_D = \frac{W\mu_{FET}C_i}{L}[(V_{GS} - V_T)V_{DS}] \tag{2.9}$$

In the linear regime, I_D is directly proportional to V_{GS}. However, when $V_{DS} > V_{GS} - V_T$, the channel is *pinched-off*, I_D does not exhibit significant increase and saturates. For this reason, Equation 2.9 is no more valid for I_D in the saturation regime (I_{Dsat}). If the channel shortening, because of the depletion region at the drain is neglected, for I_{Dsat}, Equation 2.9 is updated by substituting V_{DS} with $V_{GS} - V_T$ [6]:

$$I_D = \frac{W\mu_{FET}C_i}{2L}(V_{GS} - V_T)^2 \tag{2.10}$$

Figure 2.11 shows the electrical characteristics of a cr-PVA/P3HT type OFET device; transfer characteristics, $I_D \times V_{GS}$, in the saturation regime (black solid curve in Figure 2.11a), gate leakage current, $I_G \times V_{GS}$ (orange solid curve in Figure 2.11a), and output characteristics, $I_D \times V_{DS}$, for different V_{GS} values (Figure 2.11b). The linear and saturation regimes are evident in the output characteristics for low and high V_{DS} values, respectively (Figure 2.11b). Since P3HT is a *p*-type semiconductor, negative voltages are required to operate the OFETs.

The μ_{FET} in the saturation regime can be extracted using the linear best-fit method, by finding the slope of the plot $|I_D|^{1/2} \times V_{GS}$. This is done by taking a region where $|I_D|^{1/2} \times V_{GS}$ is a straight line (as shown in Figure 2.11a). The extrapolation of the linear-fit to $|I_D|^{1/2} = 0$ provides the V_T value of the OFET device (Figure 2.11a). The V_T is traditionally defined as the voltage after which the device turns on [83]. Among other reasons, the presence of V_T in OFETs can be attributed to energy level differences between the semiconductor and the contact, or static charges in the insulator layer or at the I/S interface [6].

Table 2.1 List of parameters required for the characterization of OFET devices.

Characteristic	Symbol	Units
Threshold voltage	V_T	V
Field-effect charge carrier mobility	μ_{FET}	cm^2/V.s
Gate insulator capacitance per unit area	C_i	F/cm^2
On-off current ratio	I_{on}/I_{off}	-
Subthreshold swing	SS	V/dec
Transconductance	g_m	S

On-off current ratio (I_{on}/I_{off}) is an important figure of merit for high performance OFETs, particularly when application in logic gates is aimed. I_{on}/I_{off} categorically distinguishes the capability of a particular OFET of providing lower I_{off} and higher I_{on}. It is defined as the ratio of the maximum value of I_D when the transistor is in its ON state (typically at the maximum value of V_{GS}) to the minimum value of I_D when the transistor is in its OFF state (typically at $V_{GS} \leq V_T$).

Transconductance (g_m) is the ratio of the change in drain current to the change in gate voltage over a defined, arbitrarily small interval on the $I_D \times V_{GS}$ curve. In general, the larger the g_m of an OFET device, the greater the gain (amplification) it is capable of delivering. If ΔI_D represents a change in drain current caused by a small change in gate voltage (ΔV_{GS}), then g_m is [83]:

$$g_m = \left.\frac{\partial I_{DS}}{\partial V_{GS}}\right|_{V_{DS}} \tag{2.11}$$

The subthreshold swing (*SS*) is defined as the V_{GS} required to change I_D by one decade while the device operates in linear regime [83].

$$SS = \left.\frac{\partial V_{GS}}{\partial \log(I_D)}\right|_{V_{DS}} \tag{2.12}$$

A list of important parameters that characterize the performance of OFET devices is shown in Table 2.1.

2.5 Effective thickness of the OFET conducting channel

In Section 2.4.1, it was briefly discussed that the accumulated charge density at the I/S interface of OFETs is a function of position in the conducting channel. This is related to the difference in potentials in different regions of the conducting channel, which influences the effective channel thickness. For OFETs based on high resistivity semiconductors, Seidel *et al.* and Koehler *et al.* described the theory of trap-filling transitions in order to quantify the
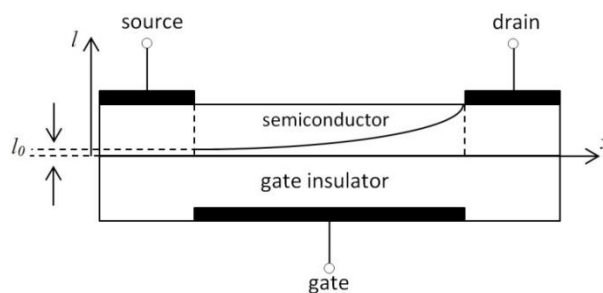
Figure 2.12 Schematic representation of OFET showing the channel bottleneck thickness [103].

effective channel thickness [104,105]. An illustration (out-of-scale) of the channel thickness is shown in Figure 2.12. The curve drawn inside the semiconductor layer represents the effective channel thickness (*l*), which contributes to the charge transport process. Essentially, the effective channel thickness in OFETs is the result of the electrical potential difference along the *x*-axis (as illustrated in Figure 2.12). The potential difference occurs due to the voltages applied between the electrodes. In this context, the voltage between gate and source (V_{GS}) tends to keep the accumulated charge carriers close to the I/S interface, while the voltage between source and drain (V_{DS}) tends to transport these charge carriers along the channel. Since the electrostatic force—that keeps the charge carriers close to the insulater/semiconductor interface—varies along the *x*–direction, the distribution of the charge carriers also varies in this direction [103].

In steady-state device operation, the potential near the source is much higher than the potential near the drain. Because of the high electric fields near the source, the contributing electrostatic forces in this region keep the charge carriers closest to the I/S interface. As a consequence, the effective channel thickness shows a minimum (*l* = 0, l_0) at the vicinities of source. This thickness (l_0) can be quantified by solving the drift-diffusion equation [104,105]. By ignoring the contribution of diffusion currents, and by assuming (1) a constant electric-field independent mobility; (2) injection of only one type of charge carriers through the ohmic contacts; (3) no current perpendicular to the I/S interface, and; (4) presence of discrete trapping levels, l_0 is expressed as [104,105][4]:

$$l_0 = \frac{4\varepsilon kT}{eC_i(V_{GS}-V_T)},$$
(2.13)

where, ε is the dielectric constant of the channel semiconductor, k is the Boltzmann constant, T is the absolute temperature and e is the electronic charge.

For typical values associated to cr-PVA/P3HT OFETs (C_i = 14 nF/cm^2, V_{GS} = 5 V and V_T = 1.5 V), the thickness (l_0) equals to ~5.5 nm. Whereas, the length of a P3HT *mer* in the alkyl stacking direction has been experimentally identified as ~1.6 nm [106]. This means that l_0 in cr-PVA/P3HT OFETs corresponds to the very first few monolayers of P3HT from the surface of cr-PVA. This, in turn, implies that the defects originating from the surface of cr-PVA (*e.g.* charged domains or dipoles [53,103,107,108]) can strongly modify the structural

---

[4] Other assumptions exist [104,105].

properties of P3HT and effect charge transport percolation paths [108,109]. Therefore, l_0 can be viewed as the bottleneck of the effective OFET conducting channel [103].

2.5.1 Role of cr-PVA surface traps in charge transport

As discussed in Section 2.3.1, the defects originating from the surface of cr-PVA mainly correspond to the hydroxyl and ketone groups of cr-PVA [53,86]. These groups (particularly hydroxyl) are known to exhibit a dipolar character [53,86,110,111]. The formation of a cr-PVA film would result in a random distribution and orientation of the dipoles at the cr-PVA surface. In the case of cr-PVA/P3HT OFETs, the manner in which the cr-PVA surface dipoles would influence the charge transport in the adjacent P3HT layer, depends on the relative energy levels (such as electron affinities and ionization potentials) of the dipoles and the neighboring P3HT molecules. During the charge transport process, the non-zero electric potentials produced by the cr-PVA surface dipoles would act as charge trapping or scattering sites for the mobile charge carriers transiting close to the cr-PVA/P3HT interface [112]. The dipolar sites producing high electric potentials can be considered as positively charged domains, whereas, the sites producing low electric potentials can be considered as negatively charged domains [108]. The positively charged domains would act as energy hills at the cr-PVA/P3HT interface of the OFET, thereby increasing the energy of charge carriers transiting through the channel interface (Figure 2.13). Consequently these energy hills would act as energy barriers for the charge carriers. On the other hand, the negatively charged domains would act energy wells, capable of reducing the energy of the charge carriers (Figure 2.13) [108].
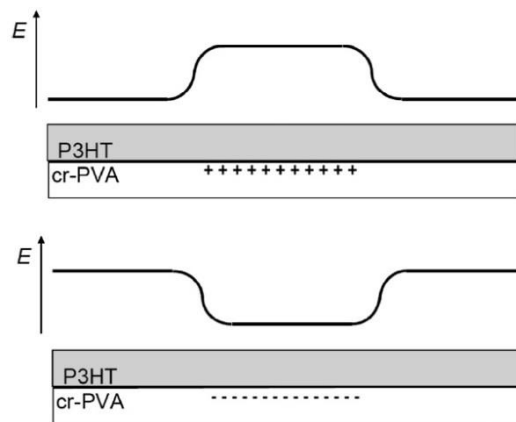
Figure 2.13 Illustration of the formation of energy hills and wells due to the presence of positively and negatively charged domains at the surface of cr-PVA [108].
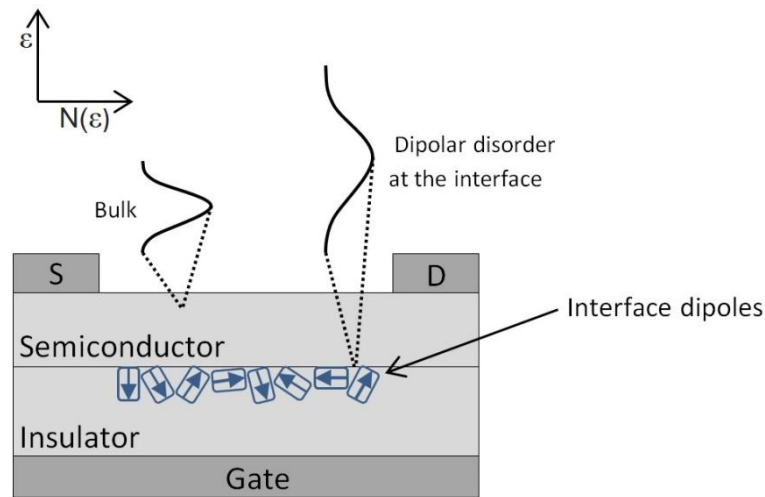
Figure 2.14 Schematic diagram of an OFET showing interface dipoles originating from the surface of the gate insulator. Local polarization due to gate insulator dipoles may lead to broadening of the DOS at the I/S interface (relative to the semiconductor bulk) [84].

In addition to the mechanisms discussed above, the dipole moments (produced by the surface dipoles of cr-PVA) can also contribute towards modifying the polarization energy of neighboring P3HT molecules. This can result in the localization of otherwise mobile charge carriers on the adjacent P3HT molecules (a review by Sworakowski *et al.* discusses this particular problem in detail [112]). Consequently, an increase in the density of localized sites at the cr-PVA/P3HT interface would be obtained. These strongly localized sites would add to the tail states of the Gaussian distributions (*vide-supra*: Section 2.1.1), resulting in the broadening of the electronic density of states (DOS), and higher potential energy variations at the cr-PVA/P3HT interface relative to P3HT bulk (Figure 2.14) [66,84]. This would result in the modification of charge transport properties, effecting critical device parameters, such as V_T, I_{on}/I_{off}, and particularly μ_{FET}.

2.6 Gate insulator surface treatments

The incremented disorder at the I/S interface (induced by the surface dipoles of cr-PVA) presents a physically complex problem, since the potential energy variations at the cr-PVA/P3HT interface depends on the position (positional disorder), orientation, and neighborhood distribution of cr-PVA surface traps. This leads to a distribution of trap binding energies (energetic disorder) [113]. The solution, however, is conceptually simple, since in principle it is only necessary to passivate the charge traps. In this project, the passivation of

cr-PVA surface traps was obtained by treating the cr-PVA surface using a cationic surfactant, hexadecyltrimethylammonium bromide (CTAB; Figure 2.15a).

Surface-active agent (surfactant) is a substance that can be adsorbed on the surface (or interface) of a system, and change its free energy [114]. Surfactants are amphiphilic substances whose molecules consist of a polar hydrophilic head group attached to a hydrophobic tail group. In the case of cationic surfactants, the surface-active part of the molecule is positively charged[5]. One of the most interesting and practical property of surfactants is their solubility in water and other commonly available solvents [114]. When dissolved in water at low concentrations, surfactants behave as electrolytes. The amphiphilic structure of the surfactant lowers the surface tension of water and causes the surfactant molecules to concentrate at the surface of water; the hydrophobic head oriented predominantly towards the air (Figure 2.15b). At higher concentrations, solubility increases and surfactants form organized aggregates called micelles in which the hydrophilic head is directed into the bulk solution and the hydrophobic tail is directed towards the inner space of the micelle (Figure 2.15b) [115,116]. The concentrations at (and above) which micelle formation occurs is known as the critical micelle concentration (CMC) [114].

Another important parameter that determines micelle formation and solubility is the Krafft point (T_k). Owing to the fact that surfactants have long hydrophobic tail groups, the solubility and micelle formation occurs above T_k [117]. T_k is usually defined as the temperature at which the CMC *vs.* temperature curve intersects the solubility *vs.* temperature curve (Figure 2.16) [118]. Keeping in view the importance of both the CMC and the T_k in terms of solubility and micelle formation, surfactants that exhibit low CMC and T_k can be considered as more convenient materials for practical purposes. Hence, CTAB was chosen for this project, whose CMC and T_k are 0.36 mg/mL and 25 °C, respectively [115,116].

The objective is to use the positively charged heads of the surfactant aiming at the passivation of negatively charged traps present on the surface of cr-PVA. Several models can be found in the literature which describe the adsorption of ionic surfactants on oppositely charged surfaces [119–125]. All of these models explain the adsorption process to be driven by the electrostatic interaction and to be strongly dependent on the surfactant concentration. Since the interactions among water and hydrophobic tails of surfactants is weaker compared

---

[5] Non-ionic and zwitterionic surfactants also exist [114].

to the interaction among water molecules, surfactant aggregation is promoted in both aqueous solution and at charged surfaces [125].
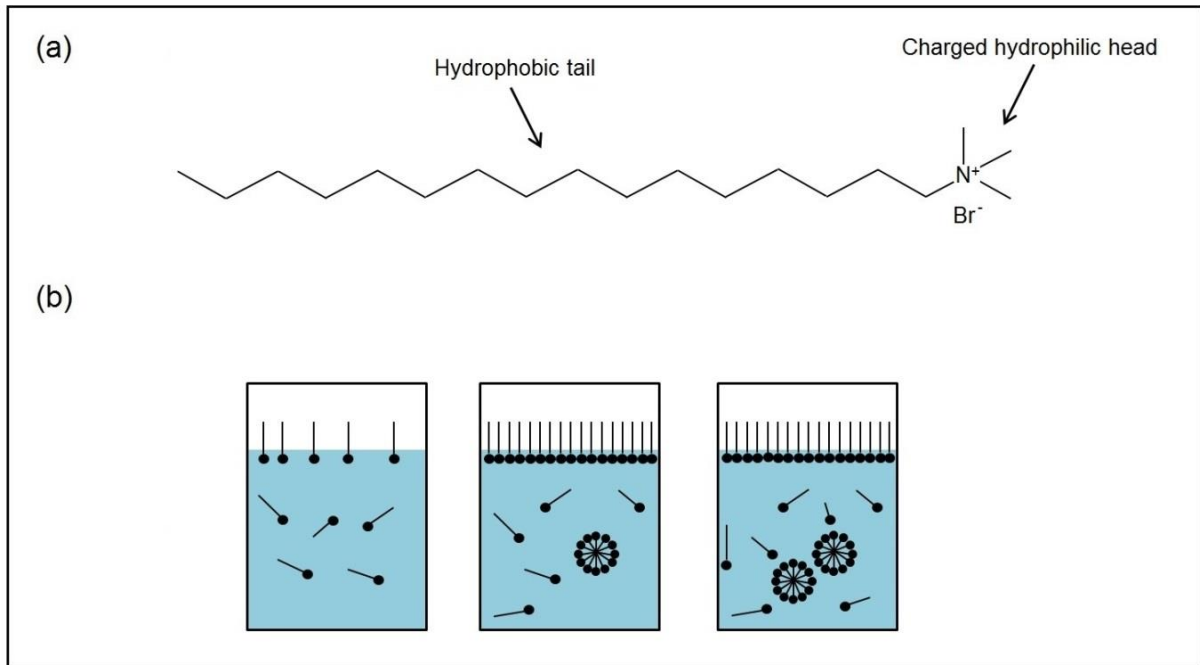
Figure 2.15 (a) Chemical structure of CTAB, and; (b) formation of micelles in aqueous solution.
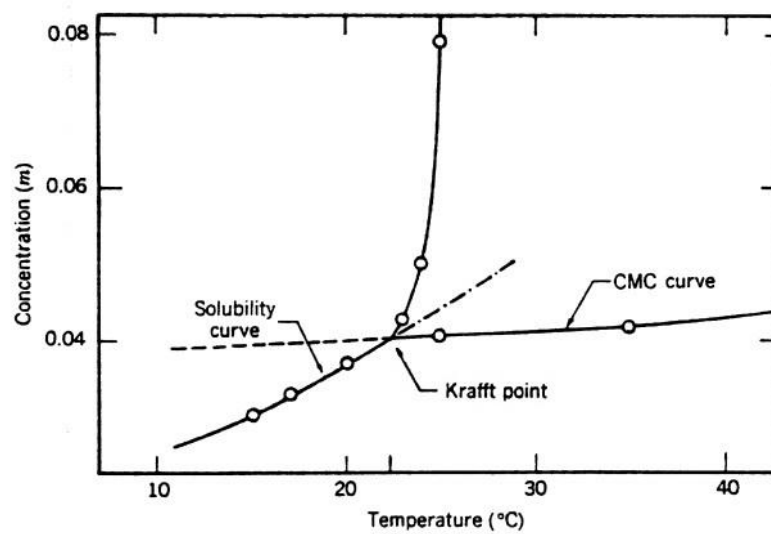
Figure 2.16 Surfactant solubilities, CMC and the T_k [118].
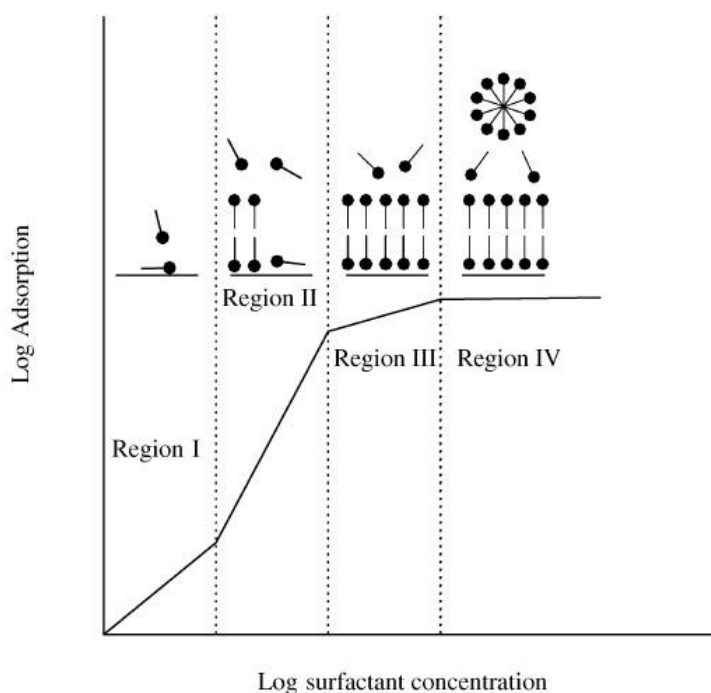
Figure 2.17 Illustration of adsorption of ionic surfactants according to the four-region adsorption model [124].

The models describing adsorption of ionic surfactant on charged substrates are based on two principal theories. The first kind of theory divides the adsorption process into various regions (below the CMC, and close to or above the CMC) [119,123–128]. For better understanding of the subsequent discussions, a four-region adsorption process is illustrated in Figure 2.17. In regions where the surfactant concentration is below the CMC, the surfactant head groups adsorb individually and the adsorption is primarily driven by the electrostatic interaction among the surfactant head groups and the charged solid substrate (Region I in Figure 2.17). At a certain CMC value, the surfactant hydrophobic tails also start to interact with each other, eventually leading to the formation of a surfactant monolayer on the substrate (where the hydrophilic heads are directed towards the charged substrate and the hydrophobic tails are directed upwards, in the opposite direction). This is illustrated as Region II in Figure 2.17. Further increase in surfactant concentration brings the regions close to (or above) the CMC. In these regions, the contribution due to electrostatic interaction disappears and adsorption takes place due to the interaction among hydrophobic tails. This leads to the formation of bilayer structure (Regions III and IV in Figure 2.17) [119]. Depending on a particular model, the process of bilayer formation comes to entirety in Region II, III or IV [119,123–128]. Nevertheless, in all the cases, the formation of bilayer structure has been identified to occur near the CMC [119,123–128].

The second kind of theory argues that the formation of surfactant bilayer on top of charged substrates depends on certain conditions [125,129–131]. In this theory, surfactant concentrations only above the CMC are considered. Accordingly, when the surfactant solution is deposited on a charged substrate, adsorption occurs in the form of aggregates of cylindrical micelles. Figure 2.18 shows an illustration of cylindrical micelles adsorbed on a charged mica substrate [125]. If the surfactant film is exposed to ambient environment for ~24 h, the adsorbed micellar structures transform to bilayer structures (as discussed for the first kind of theory). In this interpretation, the electrostatic forces—responsible for keeping the charged heads of surfactant micelles close to each other—slowly decrease, and the electrostatic interaction among the surfactant charged heads and the charged solid surface increases. In one possible explanation, the authors argue that solvent ions contribute towards this slow transformation [125]. When the surfactant is deposited, the potential solvent ions can adsorb onto the charged substrate *via* electrostatic interactions. When the surfactant film is stored for extended periods of time, the solvent slowly evaporates. As a consequence, numerous charges at the substrate (previously interacting with the solvent ions) are exposed and start interacting with the charged heads of the surfactant micelles. At a certain point in time, the interaction among the charged heads of the surfactant micelles and the substrate charges becomes strong enough to transform the micellar structures to bilayer structures.
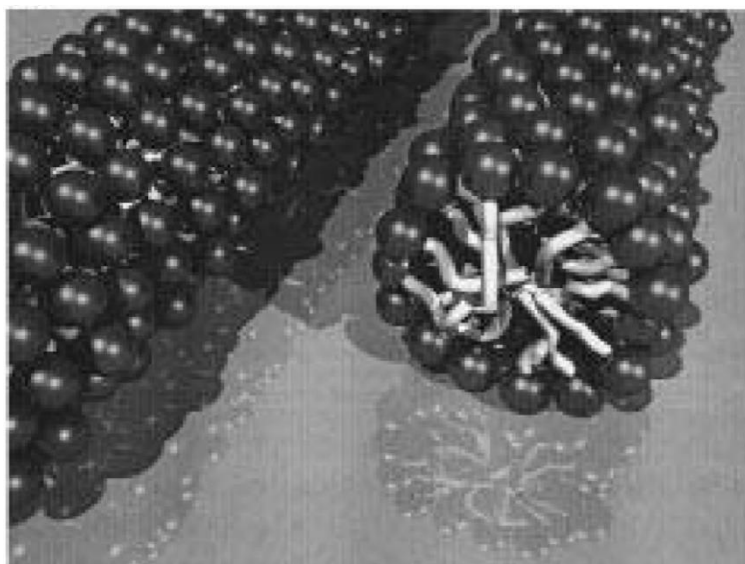
Figure 2.18 Schematic illustrations of cylindrically structured CTAB micelles adsorbed on a charged mica surface. Part of the structure on the right has been cut away to reveal the interior. The cylinders may be flattened on the bottom because of an attractive electrostatic force with the mica surface [125].

Depending on the surfactant concentration, solvent ions are also known to interrupt ordered arrangement of cylindrical micelles. Essentially, the solvent ions compete with the surfactant charged heads for surface sites. In the case of the adsorption of solvent ion, a surface site is occupied which could have been used for the adsorption of a surfactant micelle. This results in hindering the formation of well-ordered and organized cylindrical structures [125].

In light of the above discussions, we now return to the case of CTAB and cr-PVA. The electrostatic attraction between the positively charged heads of CTAB and the negatively charged domains (charge traps) of cr-PVA surface would promote the adsorption of CTAB micelles (or molecules). However, the passivation would strongly depend on the structural and morphological properties of the deposited CTAB films, which would predominantly depend on the concentration of CTAB.

In the case of adsorption *via* the first theory, CTAB concentration below the CMC would result in the formation of monolayer structures in regions of cr-PVA substrate where negatively charged domains (traps) are encountered. However, the concentration of CTAB solution would also determine the density of CTAB molecules relative to the density of cr-PVA surface traps. Hence, it is possible that until the CMC, surfactant monolayer formation occurs only on a small portion, leaving behind a large portion of untreated regions in the cr-PVA film. In such a case, when CTAB concentration at or above the CMC would be used, the surfactant molecules would form a mixture of monolayer and bilayer structures over the surface of cr-PVA. Hence, the concentration of CTAB would determine the relative densities of monolayer/bilayer structures, and consequently the passivation of cr-PVA surface traps.

The formation of bilayer structures may result in the interaction of CTAB molecules and adjacent P3HT molecules, leading to localization of charge carriers on the P3HT molecules. In addition, CTAB molecules on the upper layer may also contribute towards increasing the energy of transiting charge carriers. Hence, an optimal concentration of CTAB solution is required, which yields a structural order in the surfactant film that reduces (rather than incrementing) the potential energy variations at the cr-PVA/P3HT interface of OFETs.

Similarly, in the case of adsorption *via* the second theory, CTAB concentration would determine 1) the density of CTAB micelles relative to the density of cr-PVA surface traps, and; 2) the formation of well-ordered micellar structures. Therefore, even in this case,

concentration would play an important role in determining the effectiveness of CTAB treatment.

2.7 Problems addressed in this thesis

This thesis deals with the improvement of charge transport properties at the cr-PVA/P3HT interface of the OFET devices. Furthermore, it also discusses the effect of regioregularity defects on the interface properties. Keeping these main points in mind, the upcoming Chapters, that discuss the experimental results obtained during the project, are divided as follows.

In Chapter 3, first a simple comparison of OFET properties based on non-100% and 100% regioregular P3HT is presented. It is discussed how the absence of regioregularity defects results in significant improvement of μ_{FET} and other important device characteristics.

In Chapter 4, CTAB surfactant treatment for the passivation of cr-PVA surface traps is presented for both non-100% and 100% regioregular P3HT based OFETs. It is thoroughly discussed how the treatment modifies the potential energy variations and charge transport at the cr-PVA/P3HT interface. It is further observed that the interaction of regioregularity defects and cr-PVA surface traps is a critical factor in determining the effectiveness of the surfactant treatment and charge transport properties at the channel interface.

In order to address the above issue, molecular interactions at the cr-PVA/P3HT interface are investigated for both non-100% and 100% regioregular P3HT. The corresponding experimental results are discussed in Chapter 5. It is observed that, depending on the regioregularity, the intimate contact of P3HT molecules and cr-PVA surface traps influences the molecular order of P3HT differently. P3HT molecules produce dipole moments which depend on the regioregularity of P3HT. As a result, the interaction of non-100% or 100% regioregular P3HT molecules with cr-PVA surface dipoles has different contributions towards trap passivation at the cr-PVA/P3HT interface. The consequent effect on charge transport properties of OFETs is investigated for four thicknesses of non-100% and 100% regioregular P3HT.

The results discussed in Chapter 6 are related to a slightly different topic. A very simple experimental technique (floating–film transfer method) is presented to obtain supramolecular alignment in 100% regioregular P3HT films. The application of aligned films to OFET devices brings remarkable results, especially in terms of μ_{FET}.

It is constructive to mention that, in the following Chapters, whenever a direct comparison of results is made, the corresponding devices or thin films were prepared in the same day, under the same conditions.

3

Organic field-effect transistors based on non-100% and 100% regioregular poly(3-hexylthiophene-2,5-diyl)

3.1 Introduction

The effect of regioregularity of P3HT on its molecular order, crystalline structure and morphology has been extensively studied, and it has been demonstrated that improving the regioregularity of P3HT enhances its structural order [31,32,34–37]. Order in highly regioregular P3HT films is directly associated to reduction in the π–conjugation defects within the polymer chains, which results in enhanced edge-on orientation of the molecules [30]. Concomitantly, the electronic properties of the polymer also show improvements, such as widening of the bandwidth in the π–π stacking direction and reduction of bandgap (E_g) [35]. In addition, with increase in regioregularity, the edge-on oriented P3HT chains tend to organize into closely packed stacks resulting in the formation of larger crystallites [69]. Consequently, a stronger π–π overlap of adjacent molecules is obtained together with decrease in the density of amorphous phase in the thin films. These features result in improvement of charge transport properties of OFET devices. For instance, Bao *et al.* showed in 1996 that μ_{FET} ~0.05 cm^2/V.s can be obtained in OFETs by using 98.5% regioregular P3HT [50]. In 1999, Sirringhaus *et al.* established a direct correlation between regioregularity and μ_{FET} of OFET. They used 81% and 96% regioregular P3HT and demonstrated that improved self-organization and molecular order of 96% regioregular P3HT leads to significant improvement of μ_{FET} up to 0.1 cm^2/V.s [31]. In 2012 and sequentially in 2013, Machado *et al.* and Benvenho *et al.* demonstrated μ_{FET} of 0.08 cm^2/V.s and 0.15 cm^2/V.s, respectively, in low-voltage OFET devices [10,53]. Similarly, quite recently, in 2015, Mazzio *et al.* reported that improving regioregularity of P3HT from 93% to 99% results in an improvement in μ_{FET} by a factor of 4 [132].

In addition to the above reports, several other groups have been investigating improvement of μ_{FET} in OFET devices through modification of deposition conditions of

P3HT. In 2003, Wang *et al.* showed that mobilities up to 0.2 cm^2/V.s can be achieved by depositing 98.5% regioregular P3HT *via* dip-coating method [39]. In 2004, Chang *et al.* reported μ_{FET} of 0.1 cm^2/V.s by depositing 98% regioregular P3HT from high boiling point solvents [40]. In 2005, Yang *et al.* reported their results on OFETs in which > 90% regioregular P3HT was deposited using different boiling point solvents. In this way, they were able to control the mesoscale crystalline structure in P3HT thin films, which led to the fabrication of OFETs with mobilities as high as 0.01 cm^2/V.s [28].

The performance of P3HT based OFETs has also been demonstrated to depend strongly on the molecular weight of P3HT. In 2003, Kline *et al.* performed a systematic study on the effect of molecular weight of P3HT on its crystalline structure and on the properties of OFET devices. For optimal conditions, they demonstrated that mobilities as high as 0.1 cm^2/V.s could be obtained [133]. In 2004, and sequentially in 2006, Zen *et al.*, Zhang *et al.* and Verilhac *et al.* also reported dependence of molecular weight of regioregular P3HT on μ_{FET} of OFET devices [32,134,135].

Improvement in the μ_{FET} of P3HT based OFETs has also been achieved through improvement of insulator/semiconductor (I/S) interface properties. In 2005, Kim *et al.* demonstrated that, by controlling interface properties through the use of functionalized self-assembled monolayers over the gate insulator, mobilities up to 0.28 cm^2/V.s can be achieved in 98% regioregular P3HT OFETs. Quite recently, in 2014, Cruz-Cruz *et al.* demonstrated that the passivation of gate insulator charge traps through interfacial insertion of poly(3,4-ethylenedioxythiophene):poly(styrenesulfonate) layer can result in μ_{FET} as high as 0.57 cm^2/V.s in low-voltage OFET devices based on 93% regioregular P3HT [91].

Literature review of OFETs based on P3HT provide a clear indication that regioregularity is a prime factor in obtaining high mobility devices. However, even when highly regioregular P3HT and optimized fabrication conditions were used, μ_{FET} values less than 1 cm^2/V.s were reported [39–48]. It will be demonstrated in this Chapter that the use of 100% regioregular defect-free P3HT (DF-P3HT) in OFET devices can lead to remarkable improvement in μ_{FET} values without the use of any additional fabrication step. Firstly, the molecular order, crystalline structure and morphology of DF-P3HT thin films will be compared with non-100% regioregular P3HT thin films. Later, the electrical properties of DF-P3HT and non-100% regioregular P3HT based OFETs will be presented.

3.2 Experimental

OFETs were fabricated in bottom-gate top-contact geometry (Figure 3.1a). Soda-lime glass slides were used as substrates; cleaned sequentially with acetone, ultra-pure deionized water (resistivity > 18.2 MΩ/cm) and isopropanol in ultrasonic bath for 20 min each. For the formation of gate electrode, ~50 nm aluminum (Al) layer was thermally evaporated in vacuum at a base pressure of 10^{-6} Torr. Gate insulator layer was prepared using cross-linked poly(vinyl alcohol) (cr-PVA). PVA, obtained from Sigma-Aldrich (M_w = 130 kDa) was dissolved in ultra-pure deionized water at a concentration of 60 mg/mL, followed by magnetic stirring on a pre-heated hot plate (60 ºC) for ~2 h. Sequentially, ammonium dichromate (AD, also obtained from Sigma-Aldrich) was dissolved in PVA at a concentration of 15 mg/mL [53], followed by magnetic stirring for ~1 h. The PVA:AD solution was spin coated over the Al substrates at 4000 rpm for 60 s. The films were then exposed to ultraviolet radiation (8 W, wavelength of 365 nm) in order to produce the cross-linking. The Al/cr-PVA substrates were thermally annealed in oven under vacuum for ~2 h at 100 ºC. The resulting
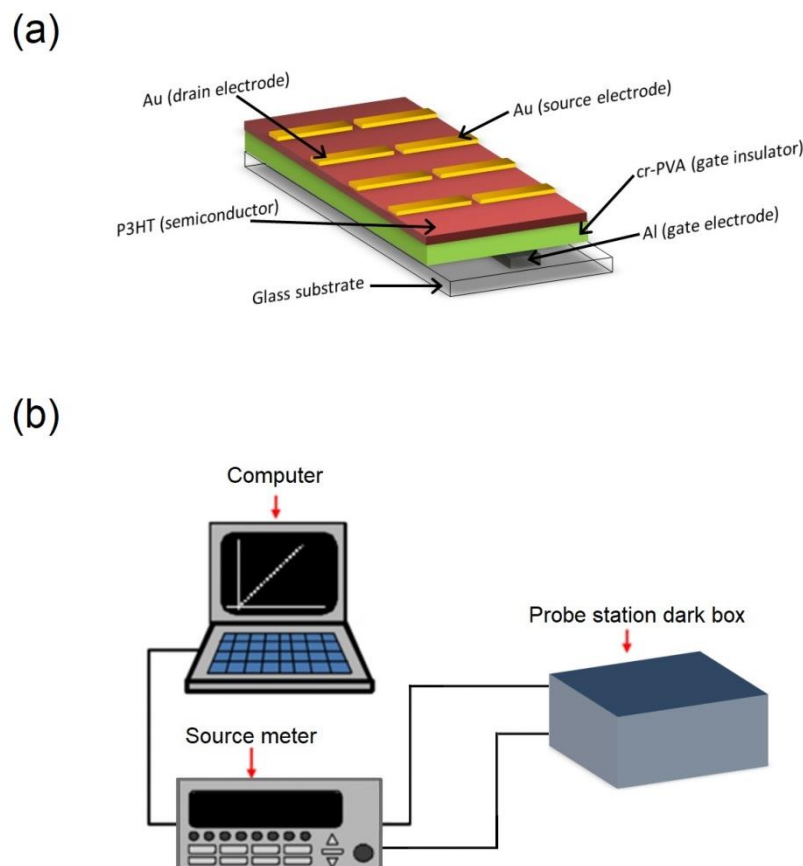
Figure 3.1 (a) Schematic structures of 4 OFET devices fabricated over a glass substrate, and; (b) illustration of the experimental setup utilized for the electrical characterization of OFETs. Part of the Figure 3.1b is reproduced from [136].

thickness of cr-PVA layer was ~300 nm. For the deposition of active layer, 98% and 100% regioregular P3HT were used. 98% regioregular electronic-grade P3HT (EG-P3HT) was purchased from Sigma-Aldrich (M_n ~ 75 kDa), while 100% regioregular defect-free P3HT (DF-P3HT) was synthesized by the group of Prof. Anil Kumar (Indian Institute of Technology, Bombay, India) using continuous flow synthesis method (M_n: 41 kDa) [81]. P3HT solutions were prepared in toluene at concentrations of 7 mg/mL at 60 °C, sequentially spin coated over the cr-PVA substrates. P3HT films were then thermally annealed in vacuum at 100 °C for 30 min. The thicknesses of the P3HT films were measured to be ~40 nm. Finally, ~50 nm thick gold (Au) source and drain electrodes (channel length of 100 μm and channel width of 2 mm) were deposited by thermal evaporation at ~15 Å/s (base pressure of 10^{-6} Torr).

The electrical characterization of OFETs was performed in dark ambient environment using a Keithley 2602 source meter. The experimental setup is illustrated in Figure 3.1b.

It has been demonstrated previously that Au diffuses into polymer layers [137,138]. One of the probable consequences of Au diffusion is the formation of an additional layer of Au over the underlying polymer layer. This would decrease the effective thickness of the polymer layer. In the case of polymer gate insulators (such as cr-PVA), this is particularly problematic, since the decreased thickness of the gate insulator would result in an increased capacitance. In order to avoid this problem, high evaporation rates must be used such that the Au particles order themselves uniformly at the surface of the polymer instead of diffusing into it. Alternatively, Al can be evaporated onto the polymer, since the diffusion of Al is less
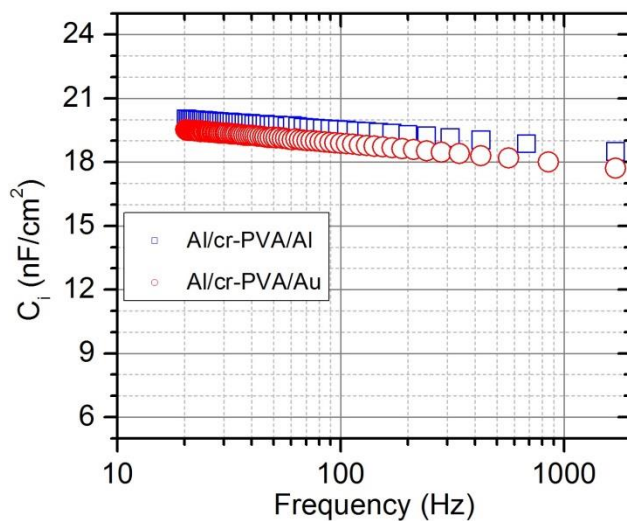
Figure 3.2 $C_i \times f$ of cr-PVA in Al/cr-PVA/Au and Al/cr-PVA/Al sandwich structures (active area = 0.1 cm^2).

probable. Both these points were experimentally confirmed by measuring the capacitance of cr-PVA in Al/cr-PVA/Au and Al/cr-PVA/Al sandwich structures using an Agilent 4284-A inductance, capacitance, resistance (LCR) meter (operating at 1 kHz [139]). In the case of Al/cr-PVA/Au structure, Au was evaporated at ~15 Å/s and the capacitance values were similar to those obtained from Al/cr-PVA/Al structure (Figure 3.2).

The thickness of the thin films was measured using a BrukerDektakXT surface profiler. UV-vis absorbance spectroscopy was performed at Laboratório de Propriedades Ópticas, Eletrônicas e Fotônica – UFPR using a Perkin Elmer LAMBDA 950 UV/Vis/NIR Spectrophotometer. The deposition conditions for the preparation of thin films are similar as mentioned before. X-ray Diffraction (XRD) measurements were performed at Pontifícia Universidade Católica do Paraná, in an XRD 7000 Shimadzu X-Ray Diffractometer, using Cu Kα X-ray radiation with an incident angle of 0.2°. The diffraction patterns were calibrated relative to the Si(111) diffraction peak of the powder reference sample. The inter–planar spacing of 16.5 Å in the direction parallel to the substrate was calculated from the (100) diffraction peak, positioned at $2\theta = 5.36°$. Atomic force microscopy (AFM) images of the

In order to compare P3HT films were taken at the Centre for Electronic Microscopy (CME-UFPR), using a Shimadzu SPM-9500J3 scanning probe microscope.

3.3 Results and discussions

Figure 3.3 shows the absorbance spectra in the region of π–π* absorption of EG-P3HT and DF-P3HT thin films deposited over cr-PVA substrates. The first, second and third absorption peaks are labeled as A_{0-0}, A_{0-1} and A_{0-2}, respectively, and the spectra are normalized to A_{0-2}. According to the literature, A_{0-0} is related to inter–chain absorption of P3HT [33,140,141], and A_{0-1} is related to intra–chain absorption [33]. The shift of A_{0-1} to lower energies (red-shit) is correlated with the formation of extended and planarized chains [33,142,143], and increase in the effective conjugation lengths [33]. Similarly, A_{0-2} is related to absorption from disordered unaggregated molecules or short oligomers [40,141,144]. The absorbance data, in Figure 3.3, shows that increase in regioregularity of P3HT results in an increase in the intensity of A_{0-0} absorption peak, red-shift of A_{0-1} peak and reduction in the intensity of A_{0-2} absorption peak. This suggests improvement of both inter– and intra–chain order in DF-P3HT film. An interesting feature of the absorbance spectrum of DF-P3HT is the significant (relative) reduction in the A_{0-2} absorption peak *i.e.* the absorption from disordered unaggregated molecules or segments with shorter conjugation lengths (Figure 3.3). This
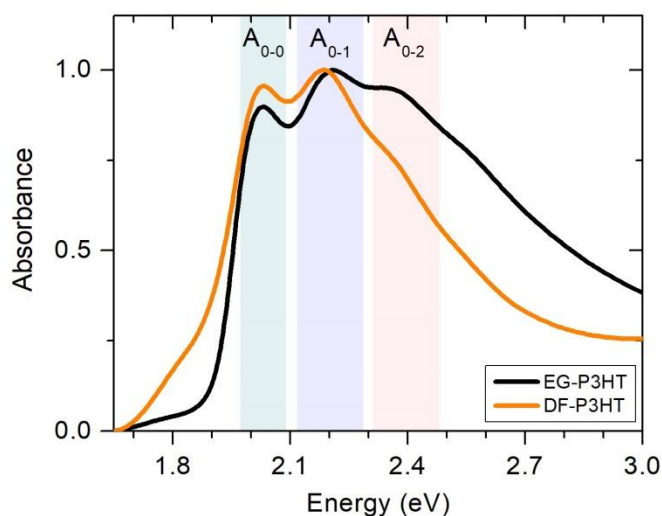
Figure 3.3 UV-vis absorbance spectra of EG-P3HT and DF-P3HT thin films deposited over cr-PVA substrates.

indicates that—apart from the formation of extended and planarized polymer chains within the crystalline regions—the complete elimination of regioregularity defects helps in the significant reduction of disordered unaggregated chains. In other words, the absence of regioregularity defects helps in the formation of well-defined and bigger crystallites.

In order to compare the crystallite sizes of EG-P3HT and DF-P3HT, XRD experiments on the thin films were performed (Figure 3.4). The diffraction peaks appearing at $2\theta \approx 5.3°$ correspond to the (100) alkyl side chain direction of P3HT molecules [41,134]. Using the Scherer formula [145], the crystallite diameter sizes of EG-P3HT and DF-P3HT were estimated to be ~30 Å and ~80 Å, respectively. This finding is in agreement with the absorbance data (Figure 3.3) that DF-P3HT film consists of bigger crystallites, and at the same time, it highlights the influence of the absence of regioregularity defects on polymer's structural order.

Figure 3.5 shows the AFM height images of P3HT thin films deposited over cr-PVA substrates. The morphology of P3HT is known to be dependent on its molecular weight and processing conditions. Low molecular weight P3HT is known to form nanofibrils or nanorods, whereas, such a morphology becomes less defined as the molecular weight increases. This has been previously demonstrated by Kline *et al.* and Verilhac *et al.* [32,41,133], where low molecular weight P3HT (M_n < 4 kDa) showed nanorod-like morphology, while high molecular weight P3HT (M_n > 30 kDa) showed isotropic nodule-like morphology. In the present case, the morphologies of P3HT thin films are similar to those

reported for high molecular weight samples by Kline *et al.* (Figure 3.5) [41,133]. It is evident that absence of regioregularity defects results in the formation of much bigger grains in DF-P3HT thin film compared to the EG-P3HT thin film.
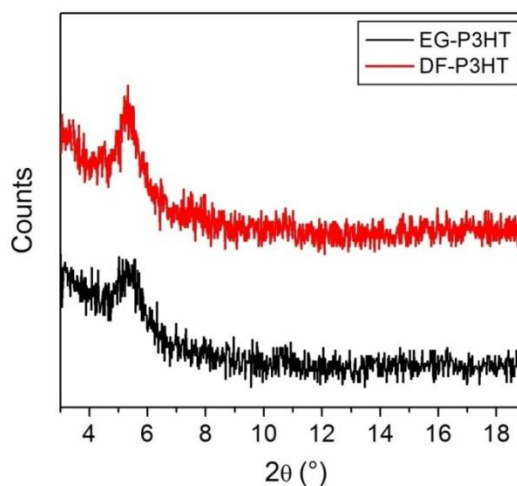
Figure 3.4 XRD patterns of EG-P3HT and DF-P3HT thin films. Base line of the spectra was displaced in order to avoid superposition [81].
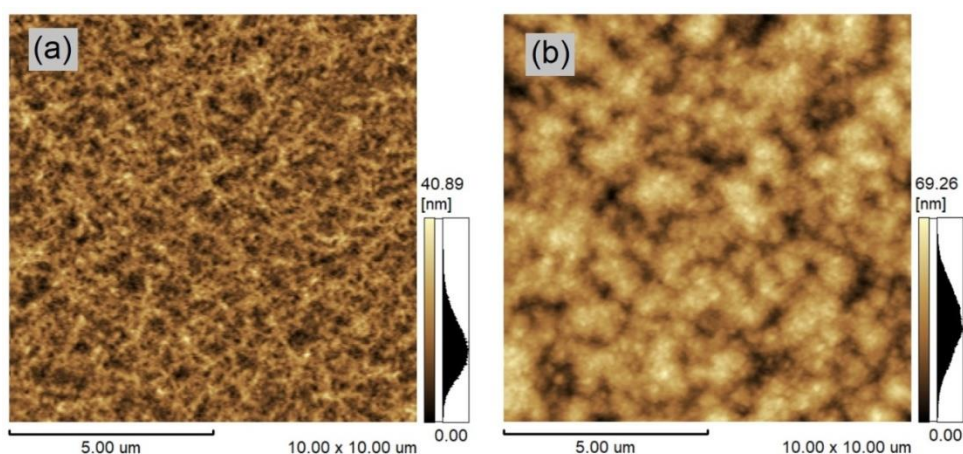
Figure 3.5 AFM height images of (a) EG-P3HT (average surface roughness, Ra: 4 nm), and; (b) DF-P3HT (Ra: 9 nm). The thin films were deposited over cr-PVA substrates.
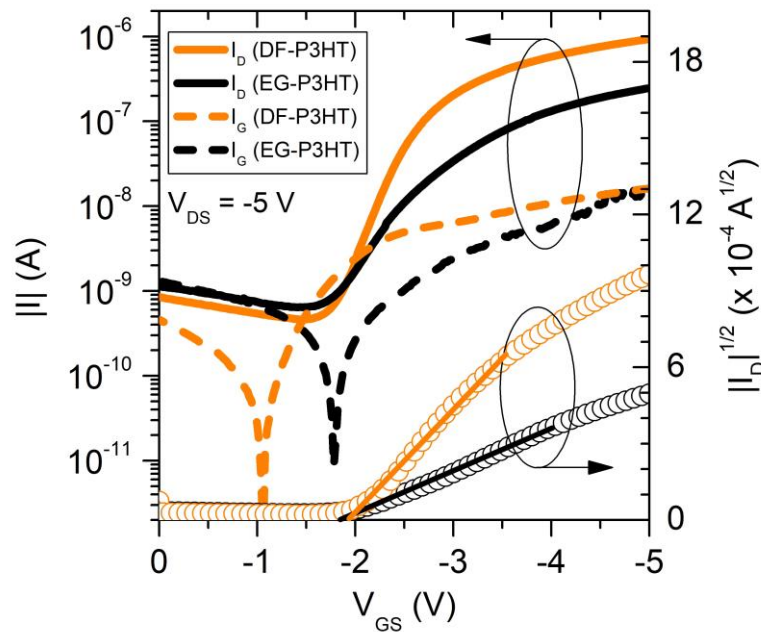
Figure 3.6 $I_D \times V_{GS}$ and $|I_D|^{1/2} \times V_{GS}$ of 98% regioregular EG-P3HT based OFETs and 100% regioregular DF-P3HT based OFETs [81].
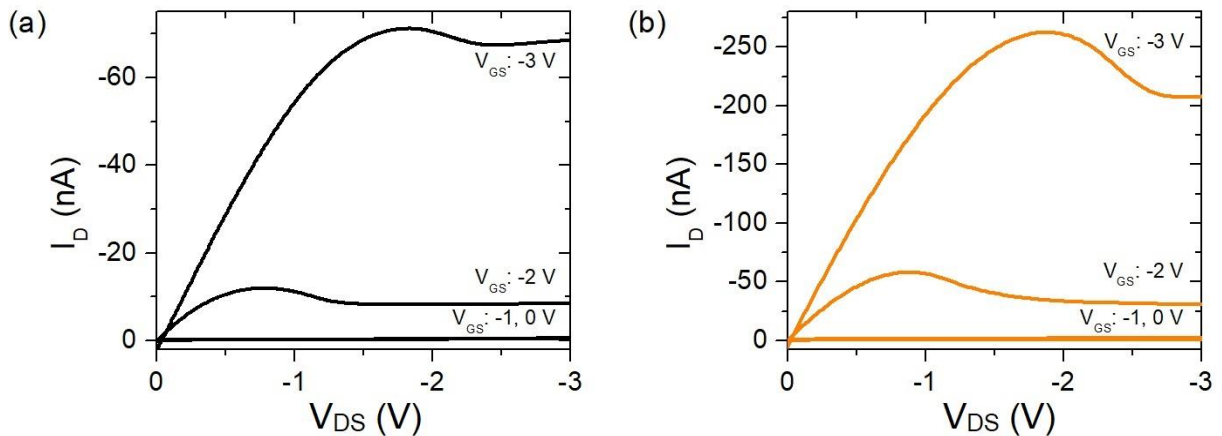
Figure 3.7 $I_D \times V_{DS}$ of (a) 98% regioregular EG-P3HT based OFETs, and; (b) 100% regioregular DF-P3HT based OFETs [81].

The electrical characteristics of OFETs based on 98% regioregular (EG-P3HT) and 100% regioregular (DF-P3HT) are presented in Figure 3.6 and 3.7. The μ_{FET} of these devices was extracted by taking the slope of linear-fit in the $|I_D|^{1/2} \times V_{GS}$ curves (Figure 3.6). The summary of electrical results averaged from the data of 10 OFET devices, fabricated and measured in the same day, is given in Table 3.1. DF-P3HT based devices show an increase in μ_{FET} by a factor of 10 when compared to EG-P3HT devices. This can be attributed to the absence of regioregularity defects in DF-P3HT thin films, which results in an improved molecular order, crystalline structure and morphological order (as demonstrated by the

absorbance, XRD and AFM data in Figure 3.3, 3.4 and 3.5, respectively). In addition, it is interesting to note that the on-off current ratio (I_{on}/I_{off}) and subthreshold swing (*SS*) also show improvement in DF-P3HT devices (Table 3.1). These results indicate better I/S interface properties when DF-P3HT is used as the active layer.

As shown in Figure 3.6, the gate leakage current ($I_G \times V_{GS}$) was observed to be ~20 nA in the scanned V_{GS} regime (0 to -5 V). This is in agreement with the initial reports on cr-PVA/P3HT type OFETs by Wagner *et al.* [10,146], Benvenho *et al.* [53] and Cruz-Cruz *et al.* [91].

Table 3.1 Performance parameters of 98% regioregular EG-P3HT and 100% regioregular DF-P3HT based OFET devices [81].

Device	μ_{FET} (cm^2/V.s)	V_T (V)	I_{on}/I_{off}	*SS* (V/dec)	g_m (µS)
EG-P3HT	0.12 ± 0.03	1.94 ± 0.22	60 ± 10	1.05 ± 0.23	0.11 ± 0.04
DF-P3HT	1.20 ± 0.11	1.97 ± 0.17	2145 ± 300	0.71 ± 0.28	0.35 ± 0.03

An important performance parameter for the use of OFET devices in practical applications is transconductance (g_m), which is useful in determining, for instance, voltage gain of amplifiers [83]. The g_m of the OFET devices was calculated from the transfer characteristics using Equation 2.5. It can be seen in Table 3.1; the use of DF-P3HT as the active layer in OFETs leads to an improvement of g_m by a factor of ~3, which implies that the modulation capability of these devices is ~3 times better when compared to EG-P3HT based devices.

The output characteristics in Figure 3.7 show the presence of a lump near the *pinch-off* regime. Although the exact mechanism causing this behavior has not been investigated during this project, it has previously been attributed to the presence of water molecules or polar group at the I/S interface [147]. The appearance of lump is particularly observed in devices fabricated in ambient environments using hydrophilic gate insulators, such as cr-PVA [108], collagen hydrolysate [148], and gelatin [149]. Sworakowski *et al.* have also theoretically correlated the lump of output characteristics with the μ_{FET} of OFET devices [109]. Detailed discussion in this context will be made in the next Chapter.

3.4 Summary

The absence of π–conjugation defects in 100% regioregular DF-P3HT results in improvement of the molecular order, the crystalline structure and the morphological order in polymer thin films. Through the absorbance data, it was observed that even the 98% regioregular EG-P3HT films consist of relatively much larger fraction of disordered unaggregated molecules. The XRD and AFM results also demonstrated much bigger crystallite and grain sizes in DF-P3HT films when compared to EG-P3HT films. As a consequence, when the DF-P3HT films were used as the active layer in cr-PVA/P3HT type OFETs, the devices demonstrated ten-fold improvement in μ_{FET} compared to EG-P3HT based devices.

4

Gate insulator surface treatment for performance enhancement of transistors, and influence of the regioregularity of poly(3-hexylthiophene-2,5-diyl)

4.1 Introduction

In this Chapter, OFET results will be discussed in which cr-PVA surface was treated with CTAB surfactant for the passivation of surface traps and improvement of charge transport properties at the insulator/semiconductor (I/S) interface. Firstly, it will be demonstrated how the critical micelle concentration (CMC) of CTAB affects its morphology. Sequentially, the influence of CTAB treatment on the electrical properties of OFETs will be discussed. In this Chapter, 98% regioregular P3HT (EG-P3HT), and 100% regioregular P3HT (DF-P3HT) are considered as the organic semiconductors.

4.2 Experimental

OFETs were fabricated in bottom-gate top-contact geometry (Figure 4.1a). The deposition techniques and conditions until the cr-PVA layer are described in Section 3.2. For cr-PVA surface treatment, CTAB solutions were magnetically stirred in ultra-pure deionized water at concentrations of 0.3, 3 and 7 mg/mL at 60 ºC for 1 h. Sequentially, the CTAB solutions were spin coated over the cr-PVA substrates at 1500 rpm for 60 s. The treated cr-PVA films were then annealed at 100 °C for 30 min. The deposition of active layer was performed using either 98% regioregular electronic-gtrade P3HT (EG-P3HT, $M_n \sim 75$ kDa) or
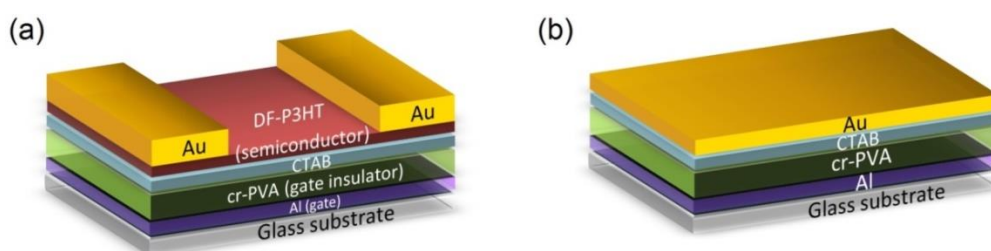
Figure 4.1 Schematic structures of (a) OFET device, and; (b) capacitor, where cr-PVA layer is treated with CTAB.

100% regioregular defect-free P3HT (DF-P3HT, M_n: 41 kDa). P3HT solutions were prepared in toluene at a concentration of 7 mg/mL at 60 °C, sequentially spin coated over the untreated and treated cr-PVA films at 1500 rpm for 60 s. P3HT films were then thermally annealed in vacuum at 100 °C for 30 min. The thicknesses of the P3HT films were measured to be ~40 nm. Finally, ~50 nm thick source and drain electrodes (channel length of 100 μm and channel width of 2 mm) were deposited by thermal evaporation of Au at ~15 Å/s (base pressure of 10^{-6} Torr). Capacitance was measured in Al/cr-PVA/Au and Al/cr-PVA/CTAB/Au sandwich structures. Deposition techniques and conditions for capacitor layers are the same as described above. Atomic force microscopy (AFM) images of the CTAB thin films were taken at the Centre for Electronic Microscopy (CME-UFPR).

4.3 Results and Discussions

4.3.1 Surface morphologies

It was discussed in Chapter 2 that micelle formation in CTAB surfactant occurs after its critical micelle concentration (CMC = 0.36 mg/mL). In order to analyse the effect of the CMC on the morphology of CTAB, atomic force microscopy (AFM) experiments were
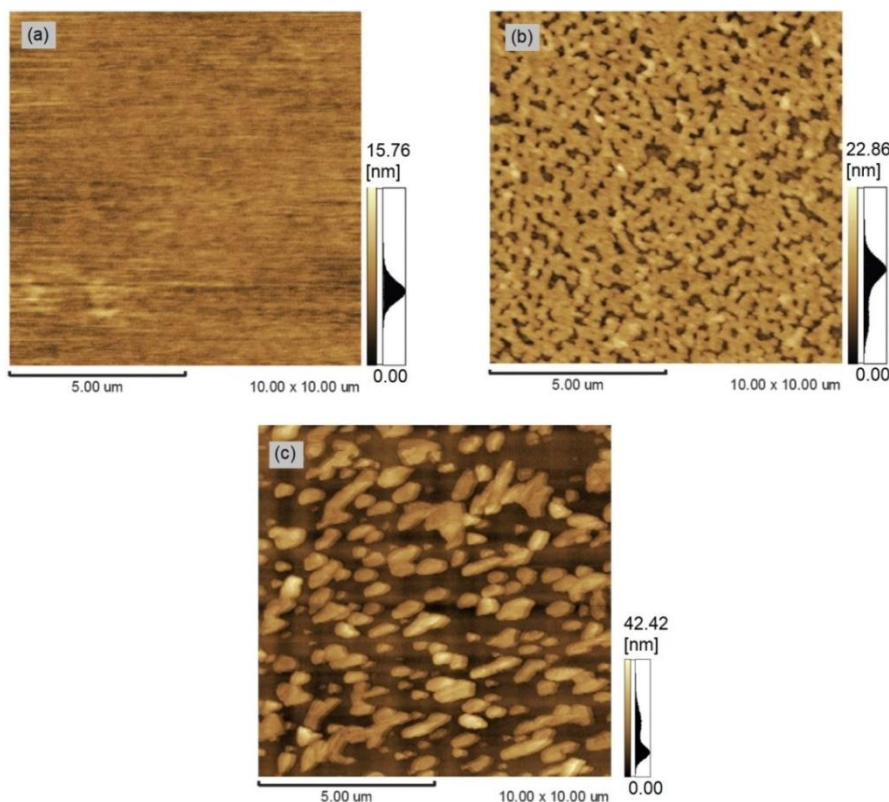
Figure 4.2 AFM images of CTAB surfactant films deposited over cr-PVA; (a) 0.3 mg/mL CTAB; (b) 3 mg/mL CTAB, and; (c) 7 mg/mL CTAB [113].

performed on the thin films prepared with three different concentrations of CTAB (0.3, 3 and 7 mg/mL). In these experiments CTAB was deposited over cr-PVA substrates and the Krafft temperature (T_k) for CTAB solution preparation was maintained 60 ℃ in each case. The results are shown in Figure 4.2. Since the solubility and micelle formation in surfactants is limited below the CMC, when 0.3 mg/mL of CTAB is deposited over cr-PVA, a flat morphology is observed with no evident agglomerate formation. Hence, it appears that micelle formation is an essential pre-requisite to obtain well-connected agglomerate formation over the surface of cr-PVA. However, when the concentration of CTAB is increased above the CMC (3 mg/mL, Figure 4.2b), the surface of cr-PVA is covered with connected agglomerates. It is interesting to note that, when the concentration is further increased above CMC (7 mg/mL, Figure 4.2c), although an increase in agglomerate size is observed, the agglomerates adopt a scattered morphology and lack evident interconnections.

4.3.2 Surfactant treatment in non-100% regioregular P3HT based OFETs

The effect of CTAB treatment of cr-PVA surface on the electrical properties of non-100% regioregular P3HT OFETs was investigated for concentrations below and above the CMC of CTAB (0.3, 3 and 7 mg/mL). In the case of 0.3 mg/mL, the corresponding AFM image in Figure 4.2a does not show any prominent aggregate formation of CTAB. Consequently, when cr-PVA surface was treated with 0.3 mg/mL of CTAB, the electrical characteristics of OFET devices also did not show improvement when compared to OFETs in which untreated cr-PVA was used ($I_D \times V_{GS}$ shown in Figure 4.3). On the other hand, when the cr-PVA surface was treated with 3 mg/mL CTAB, improvement in OFET device characteristics was obtained (results discussed in detail in the subsequent paragraph). Quite interestingly, when the cr-PVA surface was treated with 7 mg/mL CTAB, further degradation in OFET device characteristics was observed when compared to untreated devices. These results indicate that increasing the concentration of CTAB does not guarantee improvement of OFET performance. Similarly, the deposition of 7 mg/mL CTAB also shows a scattered morphology when compared to the 3 mg/mL case in which the OFET device characteristics showed improvement. This indicates that well-connected agglomerate formation over the surface cr-PVA is one of the important parameters for obtaining improvement in OFET device characteristics.
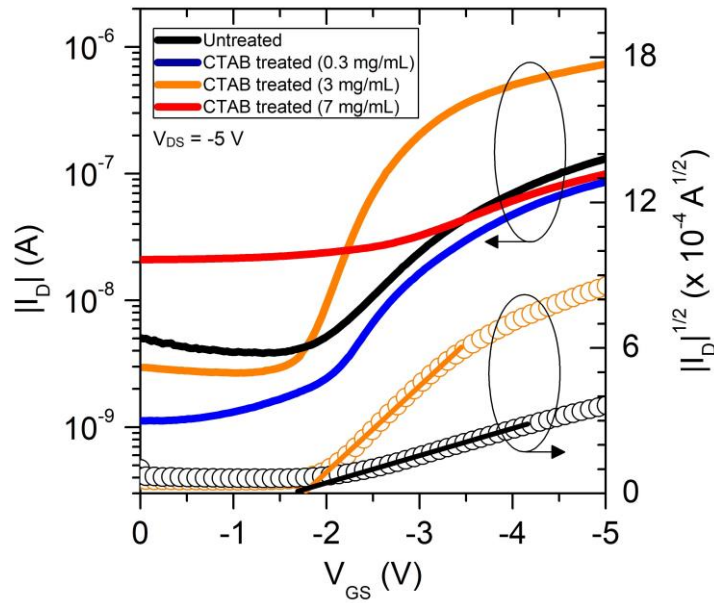
Figure 4.3 $I_D \times V_{GS}$ and $|I_D|^{1/2} \times V_{GS}$ of 98% regioregular EG-P3HT based OFETs with untreated and CTAB treated cr-PVA layers [113]. $|I_D|^{1/2} \times V_{GS}$ of OFETs treated with 0.3 and 7 mg/mL of CTAB are not shown for clarity. Gate leakage current ($I_G \times V_{GS}$) in all of the cases was observed as ~20 nA.
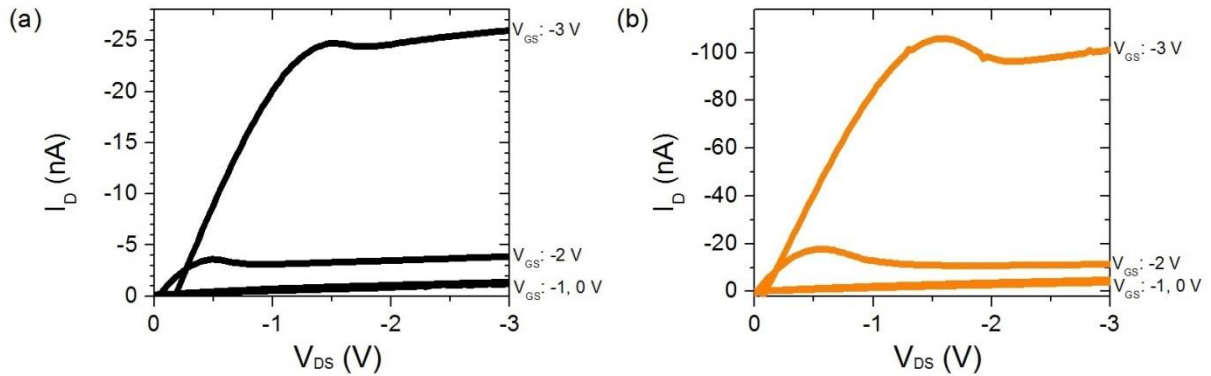
Figure 4.4 $I_D \times V_{DS}$ of 98% regioregular EG-P3HT based OFETs with; (a) untreated cr-PVA layer, and; (b) CTAB treated (3 mg/mL) cr-PVA layer [113].

Table 4.1 Performance parameters of 98% regioregular EG-P3HT based OFET devices prepared with untreated cr-PVA layer and cr-PVA layer treated with CTAB (3 mg/mL) [113].

Device	μ_{FET} (cm^2/V.s)	V_T (V)	I_{on}/I_{off}	SS (V/dec)	C_i (nF/cm^2)
Untreated	0.13 ± 0.02	1.93 ± 0.05	285 ± 30	1.77 ± 0.33	23
CTAB treated (3 mg/mL)	0.44 ± 0.05	1.88 ± 0.10	395 ± 202	1.43 ± 0.18	33

The electrical characteristics of OFET devices in which the cr-PVA layer was treated with 3 mg/mL CTAB are shown in Figure 4.3 and 4.4, and the corresponding results are summarized in Table 4.1. The capacitance per unit area (C_i) of the treated cr-PVA shows significant improvement when compared to the untreated cr-PVA, which indicates passivation of the cr-PVA traps, and thus higher charge carrier density at the cr-PVA/P3HT interface of the OFETs. In agreement, the subthreshold swing (*SS*) of treated devices also shows improvement (Table 4.1), indicating lower interfacial trap density. Consequently, CTAB treatment (3 mg/mL) results in an improvement in I_D and μ_{FET} by a factor ~4 in OFETs when compared to the devices in which cr-PVA layer is untreated.

The V_T of treated and untreated devices can be directly correlated to the passivation of cr-PVA surface traps. The higher V_T of untreated devices indicates that a larger V_{GS} is required to initially fill the traps present at the I/S interface until the ratio of free to trapped carriers increases and the conducting channel can be formed. In the case of treated devices, the partial passivation of negatively charged traps by CTAB results in the presence of more free holes at the OFET interface, such that a lower V_{GS} is required to form the conducting channel. In this context, the lower V_T for treated devices is consistent with the improved hole accumulation (increased C_i) observed for CTAB treated cr-PVA (Table 4.1).

The *lump* or *protrusion* feature near the *pinch-off* regime observed in the output characteristics (Figure 4.4) has been attributed to the adsorption of water or presence of polar groups at the I/S interface [109,147,149–151]. OFETs fabricated and measured in ambient environments are considered more prone to this behavior, since various device layers are exposed to the environment [150,152,153]. In the case of cr-PVA, this is particularly expected because of its strong hydrophilic nature [103,154]. The presence of CTAB on top of cr-PVA increases the hydrophilicity even more, making the adsorption of water more likely. This could be a reason why the lump feature is enhanced in treated devices (Figure 4.4b). Essentially, water is polar in nature (dipole moment, η(D) = 1.94 D), such that its adsorption on the surface of gate insulator can result in the modification of polarization energies at the OFET channel interface.

The lump in the output characteristics has also been theoretically associated to a lower μ_{FET} of charge carrier close to the I/S interface, by assuming [109]:

$$\mu_{FET} \propto 1 - \exp(-\frac{z}{\lambda}), \tag{4.1}$$

where, z is the distance perpendicular from the I/S interface, and λ is a characteristic length constant [109]. The presence of traps at the I/S interface can result in spatially inhomogeneous distribution of molecules in the semiconductor; the effect being greatest in the vicinities of the I/S interface. Consequently, this results in μ_{FET} that varies with the distance from the I/S interface, with lowest magnitude near the I/S interface [109]. As a result, the output characteristics may exhibit a *lump* near the *pinch-off* regime [109]. According to this theory, the output characteristics of CTAB treated devices should demonstrate a reduction in the intensity of lump, since the lower interfacial trap density after CTAB treatment (as indicated by improved C_i and *SS*, Table 4.1), would, in principle, improve device μ_{FET} at the I/S interface. On the contrary, the more enhanced *lump* in treated devices (Figure 4.4) indicates that there is (are) another mechanism(s) causing this behavior. In this context, a particularly extensive investigation (regarding the *lump* of the output characteristics) is still required, which goes beyond the scope of the current work.

Behavior of μ_{FET} close to the cr-PVA/P3HT interface of the OFETs can be analysed by plotting μ_{FET} as a function of the channel bottleneck thickness (l_0). In steady-state operation of OFET devices, the high electric fields in the vicinities of the source cause charge carriers to transit in very thin regions of the conducting channel (l_0). By solving the drift-diffusion Equation, l_0 can be expressed as [105]:

$$l_0 = \frac{4\varepsilon kT}{eC_i(V_{GS}-V_T)}, \tag{4.2}$$

where, ε is the dielectric constant of the channel semiconductor, k is the Boltzmann constant, T is the absolute temperature and e is the electronic charge. Gate voltage dependent μ_{FET} in saturation regime can be calculated using Equation 4.3:

$$\mu_{FET} = \left[\frac{d(I_D)^{\frac{1}{2}}}{dV_{GS}}\right]^2 \frac{2L}{WC_i} \tag{4.3}$$

The $\mu_{FET} \times l_0$ plot of untreated and CTAB treated devices is shown in Figure 4.5. This plot essentially provides information regarding the variation of μ_{FET} as the thickness of the accumulation layer, close to the source, changes with V_{GS}.

Several informations can be deduced through the analysis of $\mu_{FET} \times l_0$ curves for treated and untreated devices (Figure 4.5). Firstly it can be seen that, apart from the magnitude of μ_{FET}, the shape of $\mu_{FET} \times l_0$ curve in the case of the treated device is also
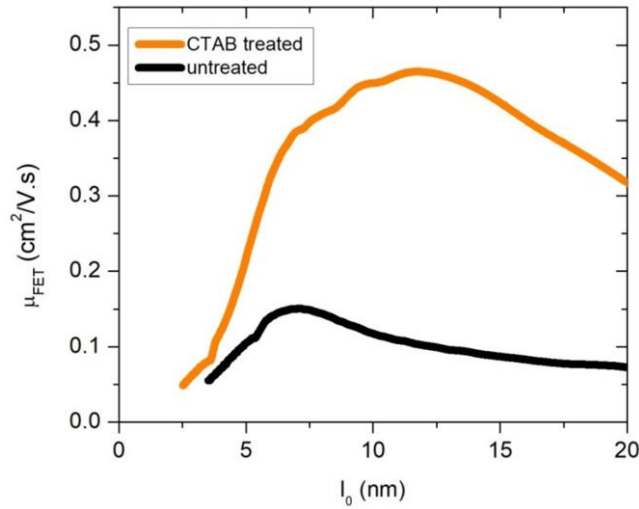
Figure 4.5 $\mu_{FET} \times l_0$ of 98% regioregular EG-P3HT based OFETs with untreated and CTAB treated cr-PVA layers.

different. This indicates that CTAB treatment involves an additional mechanism that is affecting the way charge carriers are accumulated and transported along the channel. Secondly, the common behavior among the two curves involves the decrease in μ_{FET} as $l_0 \to 0$. This behavior is in qualitative agreement with the theoretical model proposed by Sworakowski *et al.* [109] (Equation 4.1), that μ_{FET} depends on the distance from the I/S interface. The lower μ_{FET} observed close to the interface can be seen as a result of the interaction between mobile charge carriers and dipolar charged traps at the I/S interface. These traps are capable of producing potential energy variations at the interface which limits charge transport in this region. According to the multiple trapping and release (MTR) model [11,155], the mobile charge carriers would interact with the traps through trapping and thermal release. In this interpretation, the charge carriers arriving at a trap are immediately trapped, while their release is controlled by a thermally activated process. Hence, the μ_{FET} is then proportional to the rate at which charge carriers are thermally excited over the electrostatic barriers created by the interaction of the charge carriers and the traps [154]. The resulting μ_{FET} is related to the average height of the electrostatic barrier between charge carrier and charge trap by an expression of the following form [11,155]:

$$\mu_{FET} \propto n \, exp(-\frac{\bar{U}}{kT}), \qquad (4.4)$$

where, n is the charge carrier density and $\bar{U}$ is the average height of the electrostatic barrier between two elementary charges. n and $\bar{U}$ can be assumed as:

$$n \approx \frac{C_i(V_{GS}-V_T)}{el},$$ (4.5)

$$\bar{U} \approx \frac{e^2}{4\pi\varepsilon l},$$ (4.6)

where, l corresponds to the average distance between the charge carriers and the charge traps. At low V_{GS} (producing high values of l), the barrier height $\bar{U}$ between the charge carriers and the charge traps is small and the μ_{FET} increases steadily. Further increase in V_{GS} results in an increase in n; however, at this point V_{GS} also narrows the thickness of the accumulation layer. The consequent enhancement of $\bar{U}$ tends to restrict the charge flow. At a certain V_{GS}, this effect prevails over the rise of n and the μ_{FET} decreases after obtaining a peak value (at $l_0 \approx 7$ nm for the untreated device and $l_0 \approx 12$ nm for the treated device; Figure 4.5) [154]. Although decrease in μ_{FET} very close to the I/S interface is persistent for both untreated and CTAB treated devices, the peak μ_{FET} in treated devices is ~4 times higher (Figure 4.5). This indicates that the treatment produces, at least, a partial passivation of charge traps, which results in lower potential energy variation at the interface.

The $\mu_{FET} \times l_0$ curves in Figure 4.5 also show that peak μ_{FET} in the case of CTAB treated device is shifted towards thicker values of l_0. This indicates that the CTAB treatment displaces the region of the channel where effective transport takes place. In this interpretation, the CTAB layer would produce a barrier, increasing the average distance between the charge carriers flowing in the channel and the charge traps originating from the surface of cr-PVA.
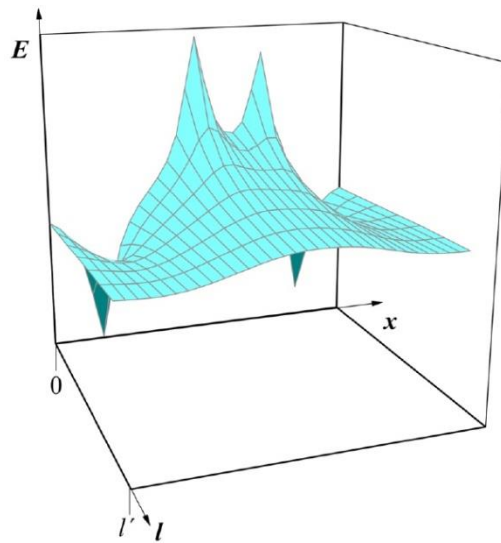
Figure 4.6 Schematic illustration of the potential energy variations for charge carriers transiting in the conducting channel. Carriers transported along the channel in the x direction encounter larger potential energy variations when flowing at $l = 0$, compared to when flowing at $l = l'$ [103].

Simultaneously, there would be a reduction in the Coulomb interaction between the charge carriers and the charge traps. The effective charge transport along the channel (l) in the x-direction would then occur in thicker regions of the channel ($l = l'$). At l', the charge carriers would be able to avoid the potential energy variations caused at $l = 0$ by the cr-PVA surface traps (Figure 4.6). As a result of the displacement of channel from $l = 0$ to $l = l'$, there would be a smoother energy profile along the channel in the x direction (Figure 4.6), concomitantly improving the μ_{FET} of the treated devices (Table 4.1).

4.3.3 Surfactant treatment in defect-free P3HT based OFETs

The influence of CTAB surfactant treatment (3 mg/mL) was also investigated for 100% regioregular DF-P3HT based OFETs [81]. The corresponding transfer characteristics of untreated and treated devices are shown in Figure 4.7, and the results are summarized in Table 4.2. Contrary to what was observed in the case of EG-P3HT devices, the surfactant treatment of cr-PVA surface in DF-P3HT devices results in degradation of the μ_{FET}. Similarly, the degradation of V_T, I_{on}/I_{off} and SS in treated devices indicates decremented properties of the I/S interface. Hence, apparently, the gate insulator surface treatment that passivates I/S interface charge traps is only effective in the case of EG-P3HT, and not in case of DF-P3HT. This indicates that, may be the increase in disorder produced by CTAB overcomes the treatment benefits when DF-P3HT is used. Similarly, it also raises a concern regarding the interaction of cr-PVA surface traps and regioregularity defects, and its effect on charge transport at the cr-PVA/P3HT interface. The latter was investigated in this project, and the corresponding results will be discussed in the next Chapter.

4.4 Summary

CTAB surfactant treatment was used to passivate cr-PVA surface traps and hence improve charge transport at the cr-PVA/P3HT interface of the OFET devices. In the case of 98% regioregular EG-P3HT based devices, when cr-PVA was treated using the optimal concentration of CTAB (3 mg/mL), the results indicated lower trap density and higher charge carrier density at the cr-PVA/P3HT interface. Consequently, these devices demonstrated improvement in μ_{FET} by a factor of ~3 when compared to untreated devices. On the other hand, when CTAB treatment was applied in 100% regioregular DF-P3HT based devices, degradation in μ_{FET} (and other performance parameters) was observed when compared to untreated devices. These results opened yet other venue to be investigated: the effect of the

interaction between cr-PVA surface traps and regioregularity defects on charge transport properties of P3HT based devices.
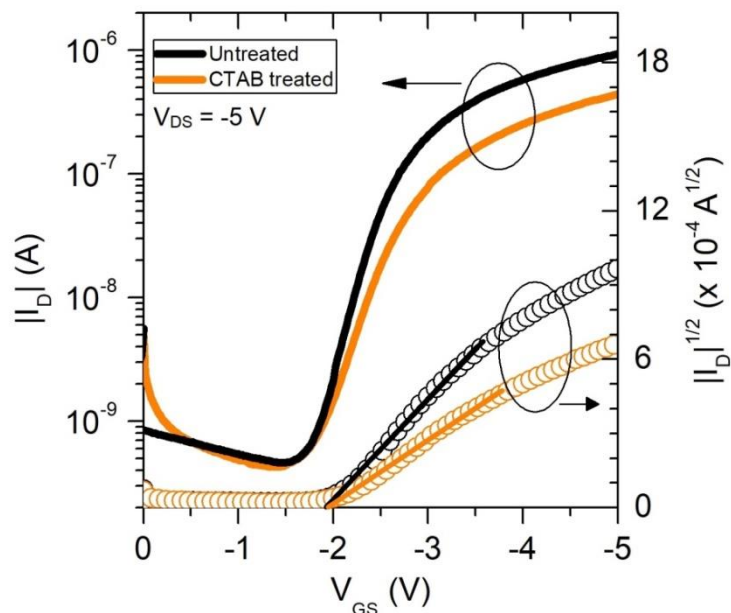
Figure 4.7 $I_D \times V_{GS}$ and $|I_D|^{1/2} \times V_{GS}$ of 100% regioregular DF-P3HT based OFETs with untreated and CTAB treated cr-PVA layers [81]. Gate leakage current ($I_G \times V_{GS}$) in both the cases was observed as ~20 nA.

Table 4.2 Performance parameters of 100% regioregular DF-P3HT based OFETs prepared with untreated and CTAB treated (3 mg/mL) cr-PVA layer [81].

Device	μ_{FET} (cm^2/V.s)	V_T (V)	I_{on}/I_{off}	SS (V/dec)	C_i (nF/cm^2)
Untreated	1.20 ± 0.11	1.97 ± 0.17	2145 ± 300	0.71 ± 0.28	18
CTAB treated (3 mg/mL)	0.25 ± 0.01	2.04 ± 0.13	820 ± 400	1.21 ± 0.33	28

5

Polymer-insulator molecular interactions, their dependence on the regioregularity of poly(3-hexylthiophene-2,5-diyl), and their consequences on transistor charge transport properties

5.1 Introduction

The interaction of dipolar functional groups of gate insulators with P3HT molecules, and their consequences on charge transport properties of OFETs has been investigated for various insulators, including SiO_2, sol-gel silica and low-κ risens [42,84,156]. For instance, the interaction of P3HT molecules with the hydroxyl groups of SiO_2 surface has been demonstrated to alter the degree of orientation of P3HT chains [42,157]. However, the investigation of polymer-insulator interactions in the above mentioned studies has mainly been limited to understanding the effects related to the use of various (low or high–polarity) gate insulators. On the other hand, the effect of regioregularity of P3HT on these polymer-insulator interactions has not yet been addressed, particularly for the case of 100% regioregular DF-P3HT. In this Chapter, it is investigated how polymer molecules of DF-P3HT and 93% regioregular P3HT interact with the surface dipoles of cr-PVA, and how these interactions affect charge transport properties of OFETs. Keeping in view that overgrown polymer layers can influence the organization and packing of underlying layers, four different thicknesses (20, 40, 80 and 120 nm) of DF-P3HT and 93% regioregular P3HT are considered. Initially, the charge transport properties of OFETs (prepared with all four thicknesses of P3HTs) are discussed. Sequentially, results from UV-vis absorbance spectroscopy, AFM, and quantum chemical calculations are discussed, in order to understand how molecular interactions at the cr-PVA/P3HT interfaces influence the charge transport properties of OFETs.

5.2 Experimental

OFETs were fabricated in bottom-gate top-contact geometry (Figure 3.1a). The deposition techniques and conditions until the cr-PVA layer are described in Section 3.2. For

the deposition of the active layers, 93% regioregular P3HT (LT-P3HT[6], $M_n \sim$ 27 kDa) and 100% regioregular defect-free P3HT (DF-P3HT, M_n: 70 kDa) were used. P3HT solutions were prepared in toluene at concentrations of 3, 7, 11 and 15 mg/mL at 60 °C, sequentially spin coated over the cr-PVA substrates. P3HT films were then thermally annealed in vacuum at 100 °C for 30 min. The thicknesses of the P3HT films were measured to be ~20 nm (3 mg/mL), ~40 nm (7 mg/mL), ~80 nm (11 mg/mL) and ~120 nm (15 mg/mL). Finally, ~50 nm thick source and drain electrodes (channel length of 100 µm and channel width of 2 mm) were deposited by thermal evaporation of Au at ~15 Å/s (base pressure of 10^{-6} Torr).

UV-vis absorbance spectroscopy and AFM measurements were performed at Laboratório de Propriedades Ópticas, Eletrônicas e Fotônica – UFPR and Centre for Electronic Microscopy (CME-UFPR), respectively.

Quantum chemical calculations were performed using density functional theory with B3LYP and 3-21G as exchange correlation functional and basis set, respectively, as per implemented in Gasussian03 package [158]. The electronic structure and dipole moments were obtained by running single point calculations of the optimized structures at the same level of theory.

5.3 Results and discussions

5.3.1 OFET electrical characteristics

Figure 5.1 shows the $I_D \times V_{GS}$ curves of the DF-P3HT and LT-P3HT OFETs, while the devices operated in the saturation regime. The performance parameters of all the measured
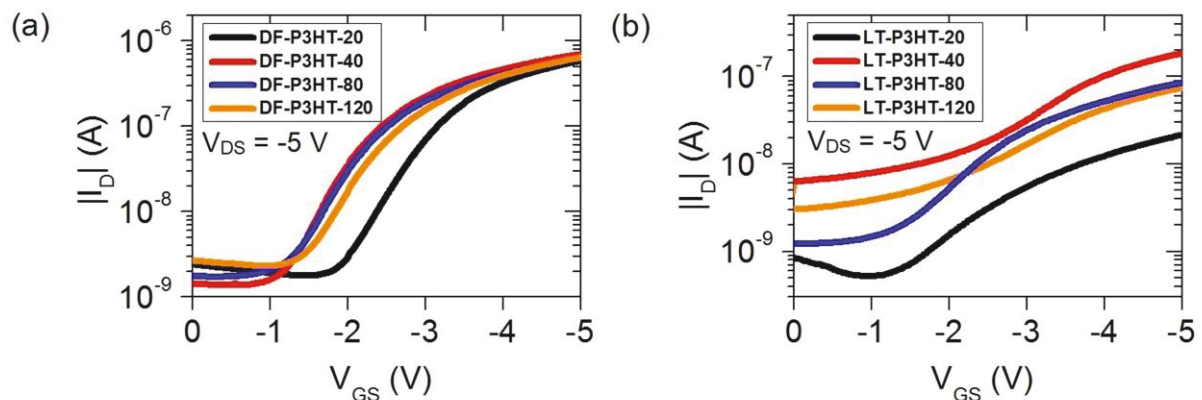
Figure 5.1 $I_D \times V_{GS}$ of OFETs with varying thicknesses of (a) DF-P3HT, and; (b) LT-P3HT [160]. Gate leakage current ($I_G \times V_{GS}$) in all of the cases was observed as ~20 nA.

---

[6] LT = Luminescene Technology (LUMTEC).

OFETs are summarized in Table 5.1. Many electrical parameters appear to be dependent on the thickness of the P3HT films. For instance, in the case of the DF-P3HT devices, μ_{FET} and V_T show a decreasing trend, whereas, I_{on}/I_{off} and *SS* show an increasing trend as a function of the thickness of DF-P3HT. The decrease in μ_{FET} with increasing DF-P3HT thickness may be attributed to the deteriorating morphology caused by the overgrowing layers of DF-P3HT, since the growth of one polymer layer on top of another layer can produce perturbations in the morphology of the semiconductor film, thereby inducing charge traps [105,159]. In such a situation, as more monolayers are grown over each other, the most affected are the underlying layers where the effective charge transport has to take place. This would result in relatively inferior insulator/semiconductor (I/S) interface properties and higher concentration of traps at this interface, which is indeed manifested by the higher *SS* values of the 80 nm and 120 nm DF-P3HT devices (Table 5.1). Since the I/S interface properties of thicker DF-P3HT devices are relatively weaker, the relatively higher I_{on}/I_{off} and lower V_T in these devices (Table 5.1) are perhaps related to better metal/semiconductor interface properties. Possibly the evaporation of Au over the thicker DF-P3HT films is resulting in the formation of a more uniform interface, which improves the charge injection compared to thinner DF-P3HT films. In the case of LT-P3HT devices, somewhat similar trends are observed except for 20 nm LT-P3HT devices where the performance dramatically degrades.

Table 5.1 Performance parameters of OFET devices prepared with varying thicknesses of DF-P3HT and LT-P3HT [160].

OFET based on	μ_{FET} (cm^2/V.s)	V_T (V)	I_{on}/I_{off}	*SS* (V/dec)
DF-P3HT (20 nm)	0.51 ± 0.11	1.92 ± 0.52	364 ± 100	1.46 ± 0.12
DF-P3HT (40 nm)	0.48 ± 0.05	1.63 ± 0.28	321 ± 103	1.41 ± 0.08
DF-P3HT (80 nm)	0.44 ± 0.07	1.27 ± 0.09	578 ± 117	1.76 ± 0.08
DF-P3HT (120 nm)	0.43 ± 0.05	1.33 ± 0.09	545 ± 117	1.83 ± 0.02
LT-P3HT (20 nm)	0.01 ± 0.01	2.01 ± 0.01	7 ± 2	2.59 ± 0.31
LT-P3HT (40 nm)	0.08 ± 0.01	1.89 ± 0.09	35 ± 10	1.84 ± 0.07
LT-P3HT (80 nm)	0.03 ± 0.01	1.24 ± 0.20	37 ± 10	1.89 ± 0.10
LT-P3HT (120 nm)	0.03 ± 0.01	1.33± 0.04	37 ± 10	1.89 ± 0.14
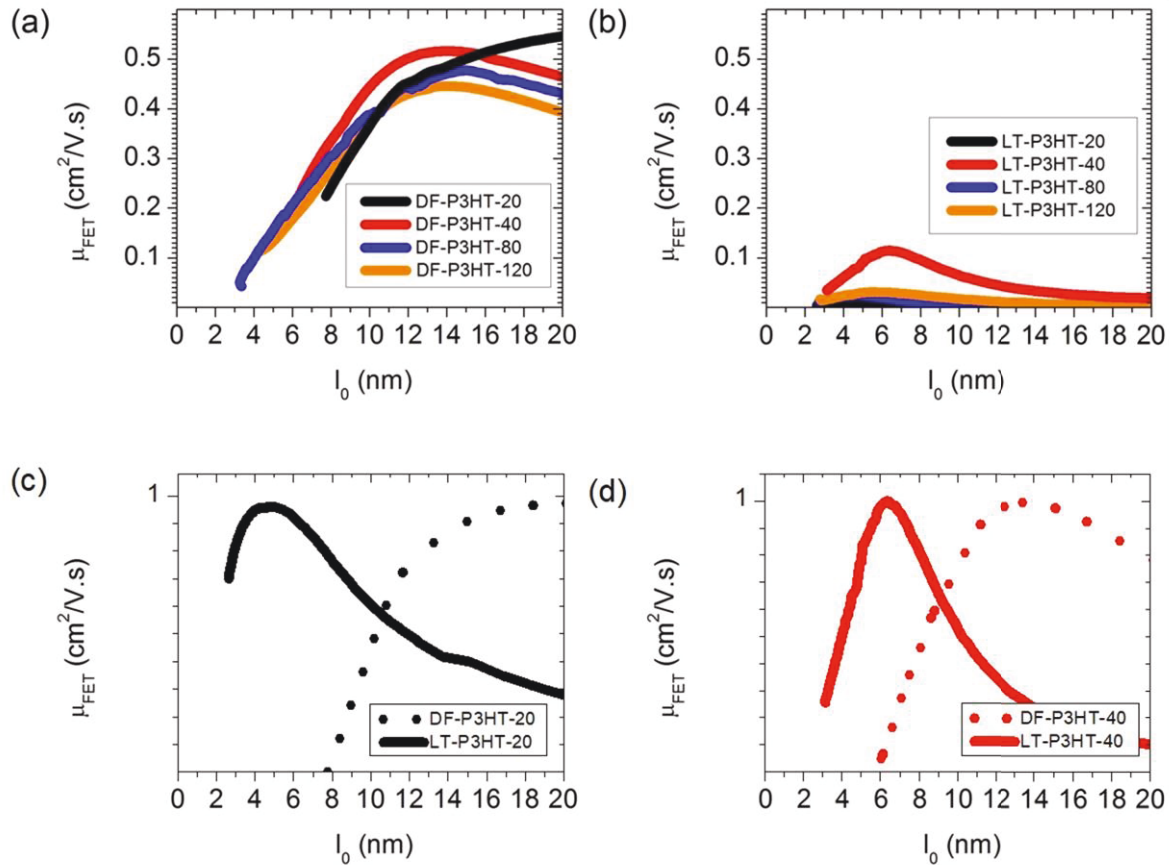
Figure 5.2 $\mu_{FET} \times l_0$ of (a) DF-P3HT OFETs, and; (b) LT-P3HT OFETs. Normalized $\mu_{FET} \times l_0$ of (c) 20 nm DF- and LT-P3HT OFETs, and; (d) 40 nm DF- and LT-P3HT OFETs [160].

The behavior of μ_{FET} as a function of channel bottleneck thickness (l_0) is analyzed using the model proposed by Koehler *et al.* (Equation 2.13) [105]. The corresponding $\mu_{FET} \times l_0$ curves are shown in Figure 5.2a,b. Generally it was observed for all the devices that μ_{FET} initially increases with decreasing l_0, eventually reaching a maximum beyond which it decreases. This trend was discussed in detail in Chapter 4, and the decrease in μ_{FET} at low l_0 values (close to the I/S interface) can be attributed to the presence of the dipolar traps at the surface of cr-PVA [53,108,113,160]. It is interesting to note that the sharp decrease in μ_{FET} as $l_0 \rightarrow 0$ is relatively less pronounced in the case of LT-P3HT devices (Figure 5.2a,b). In order to clearly demonstrate this behavior, a direct comparison of normalized $\mu_{FET} \times l_0$ curves of 20 nm and 40 nm P3HT devices are presented in Figure 5.2c,d.
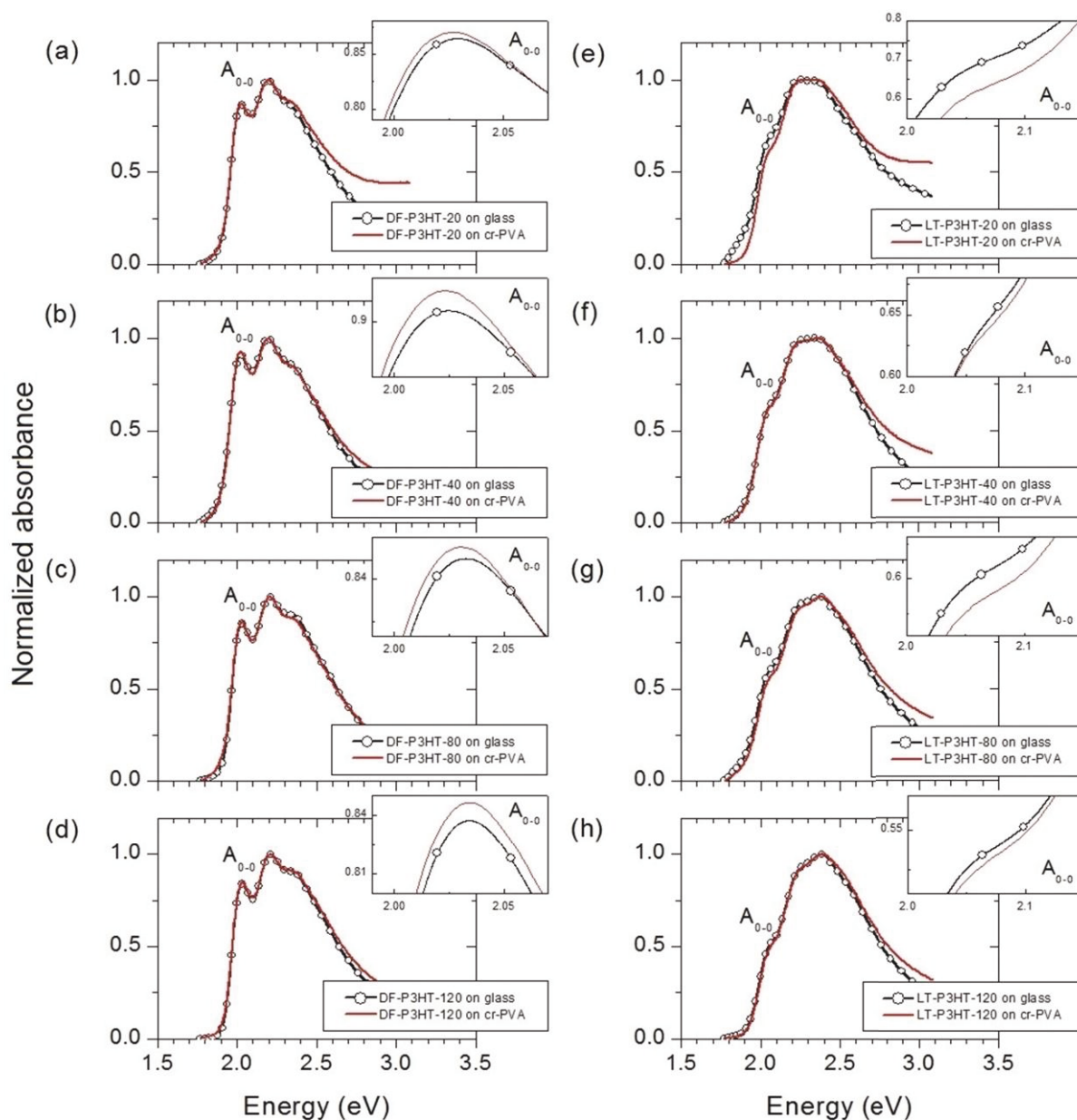
Figure 5.3 Comparison of absorbance spectra of thin films deposited over glass and cr-PVA substrates, (a-d) DF-P3HT, and; (e-h) LT-P3HT films of varying thicknesses. The insets show magnified A_{0-0} absorption peaks, where increase (decrease) in the intensity of A_{0-0} implies improvement (degradation) of the inter–chain order [33,160].

5.3.2 UV-vis absorbance spectroscopy

UV-vis absorbance spectra of DF- and LT-P3HT thin films deposited over glass and cr-PVA substrates are shown in Figure 5.3. It can be seen that, irrespective of the thickness of P3HTs, the intensity of A_{0-0} absorption peak increases when DF-P3HT thin films are deposited over cr-PVA substrates (the opposite occuring for LT-P3HT thin films). This is an

indication that the intimate contact of DF-P3HT molecules with the surface dipoles of cr-PVA results in further improvement of the molecular order of DF-P3HT, while the molecular order of LT-P3HT deteriorates upon intimate contact with the surface dipoles of cr-PVA. In particular, the relative intensity of the A_{0-0} absorption peak refers to the degree of inter–chain molecular order [33]. Similarly, since the torsional angles between adjacent repeat units control the inter–chain order, the degree of inter–chain molecular order is also related to the molecular orientation. In this context, the increase/decrease of A_{0-0} absorption peak observed in Figure 5.3 suggests that there are potential changes in molecular orientations of P3HT molecules after intimate contact with the surface dipoles of cr-PVA.

5.3.3 Surface morphologies

Figure 5.4 shows the surface morphologies of DF-P3HT and LT-P3HT thin films, deposited over glass (insets) and cr-PVA substrates (main images). The deposition of DF-P3HT over cr-PVA substrates results in an increase in average surface roughness (Ra), compared to deposition over glass (Figure 5.4a-d). Increase in roughness has previously been correlated with improved molecular order in P3HT films [82,161]. Although exact mechanism causing this behavior is not yet identified, however, these AFM results agree with the UV-vis absorbance results in Figure 5.3a-d, which also indicated improvement of molecular order in DF-P3HT films when deposited over cr-PVA substrates relative to the deposition on glass.

On the other hand, the deposition of LT-P3HT over cr-PVA substrates results in a decrease in Ra compared to deposition over glass (Figure 5.4e-h). Quite interestingly, this trend is similar to the one observed in UV-vis absorbance spectroscopy (Figure 5.3e-h). Hence, there could possibly be a correlation between molecular disorder and decrease in roughness, however, it is not completely clear at this point, and requires further investigation. The flat amorphous-like morphology observed for the 20 nm LT-P3HT film (Figure 5.4e) is a possible explanation of the drastic decrease in μ_{FET} observed for 20 nm LT-P3HT OFETs (Table 5.1).

5.3.4 Quantum chemical calculations

The electrostatic contributions to charge transport at cr-PVA/P3HT interface were investigated using quantum chemical calculations performed by the group of Prof. Marlus Koehler. P3HT oligomers with 9 repeated units were considered; one set consisting of a defect-free regioregular structure with 100% head-tail (HT) coupling, while the other set was
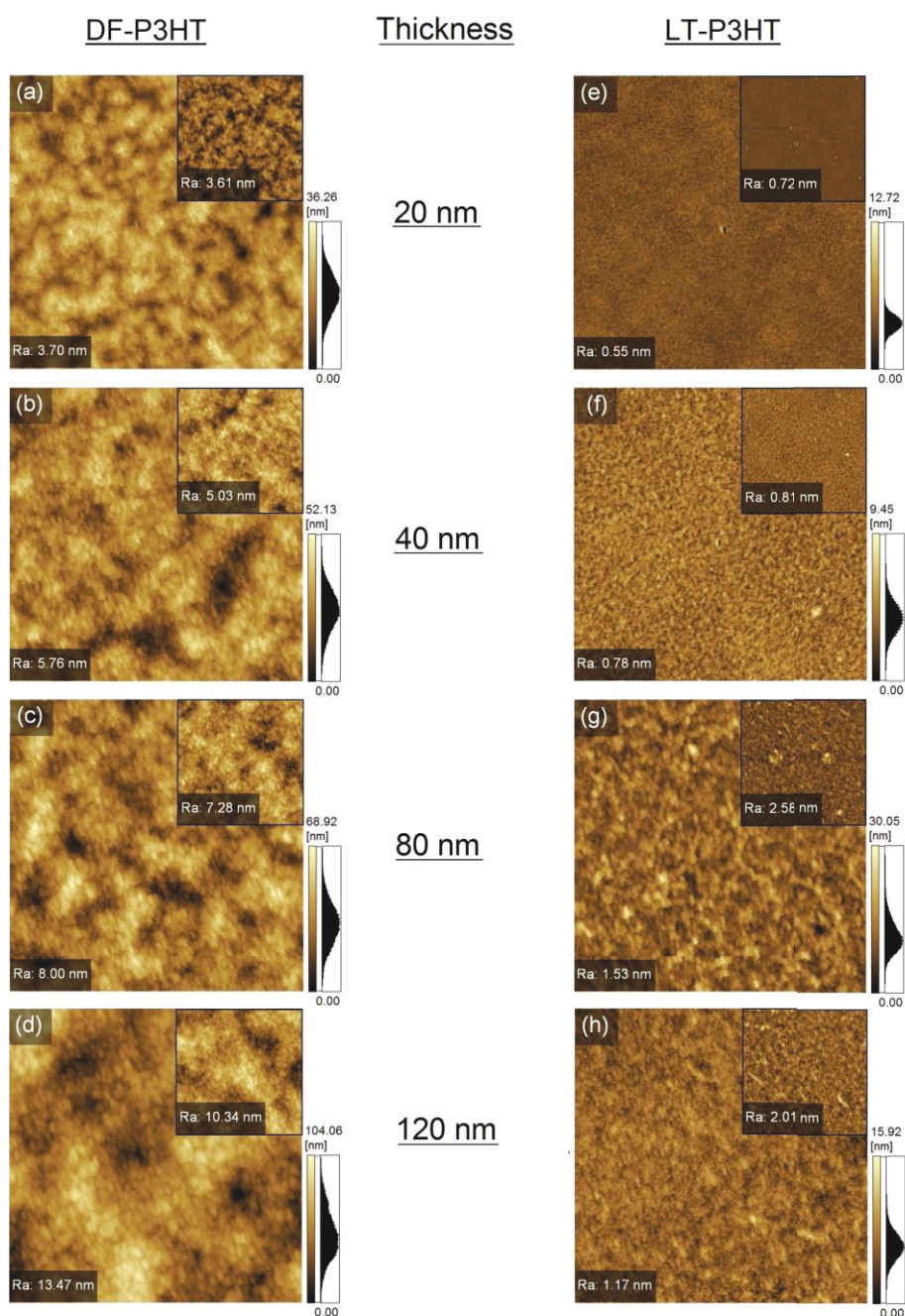
Figure 5.4 AFM height images (10×10 μm^2) of (a-d) DF-P3HT and; (e-h) LT-P3HT, deposited over cr-PVA substrates (main images), and over glass substrates (insets) [160].

simulated with a TT-HT regioregularity defect. The optimized structures of the 9-unit P3HT oligomers with a 100% regioregular configuration (left), and with a non-100% regioregular configuration (right) are shown in Figure 5.5.

The results showed that, in non-100% regioregular chains, the torsional angle at the central thiophene ring is 68.65°, which practically divides the chains in two segments with

different planes of orientation. This distortion partially breaks the π–conjugation of the chain, decreasing the delocalization of the frontier orbitals. In this case, the average theoretical

HOMO-LUMO energy gap of the non-100% regioregular structure was calculated as 2.95 eV. At the same time, the higher torsional angle between adjacent thiophene rings results in a non-planar backbone, thereby producing a high dipole moment (η(D)) per thiophene ring (0.107). In the case of 100% regioregular P3HT chains, the torsional angle between adjacent thiophene rings smoothly fluctuates around 30°. In this case, the average theoretical HOMO-LUMO energy gap was calculated as 2.70 eV. The high planarity of the 100% regioregular
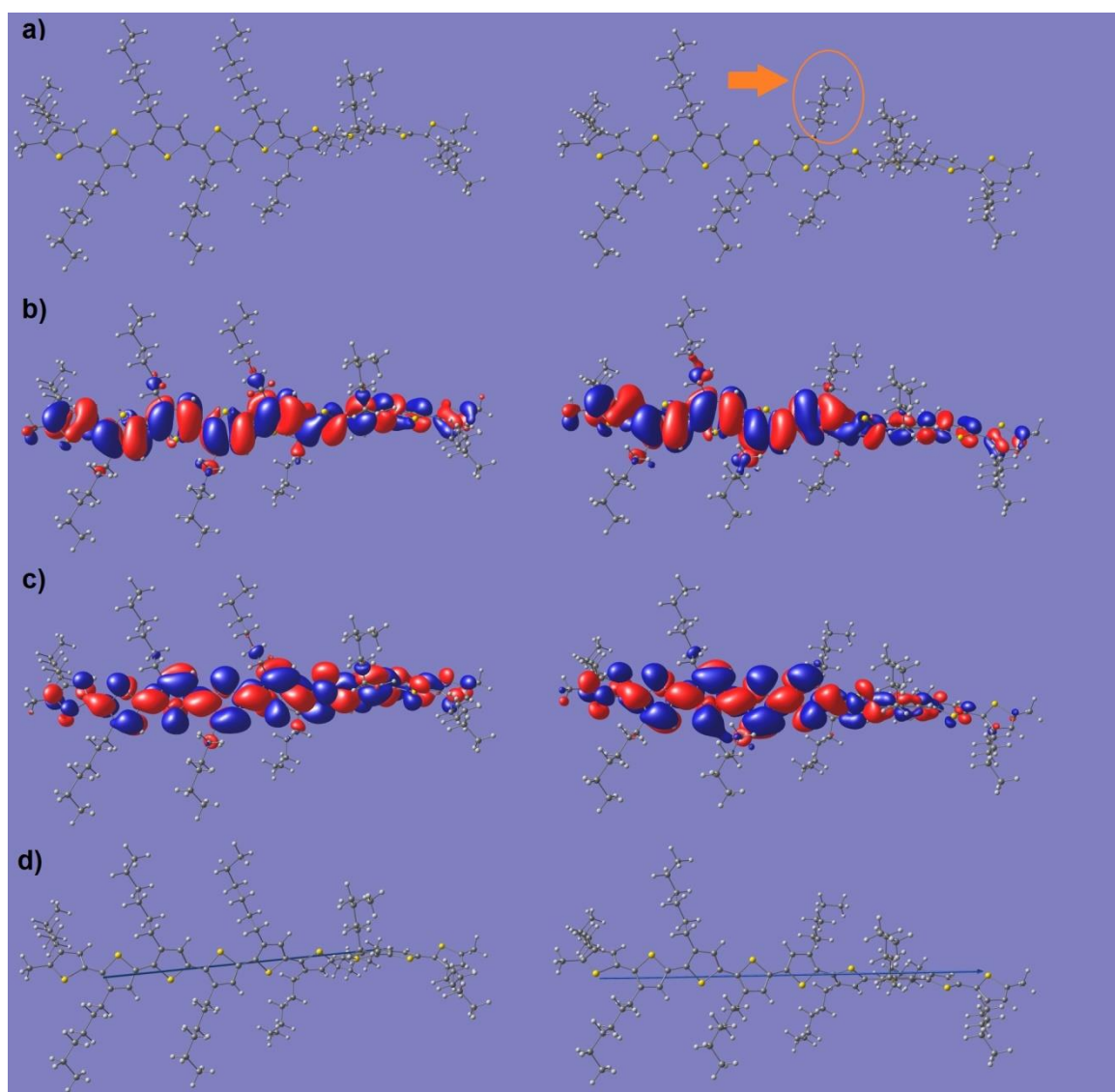
Figure 5.5 (a) Optimized structure of the 9-unit P3HT oligomer with 100% regioregular structure (left), and with non-100% regioregular structure (right). The arrow points toward the inverted position of the hexyl group in the central unit of the right structure; (b) spatial distribution of the HOMO level, and; (c) LUMO level for the 100% regioregular structure (left) and for the non-100% regioregular structure (right). (d) The orientation of the dipole moment vector in the negative to positive charge convention [160].

structure results in high delocalization of the frontier orbitals. producing a lower η(D) per thiophene ring (0.053) [160]. The results are summarized in Table 5.2.

The lower (theoretical) HOMO-LUMO energy gap obtained for 100% regioregular structure is in qualitative agreement with the absorbance results of Figure 5.3, which also showed improved inter–chain order in the case of DF-P3HT. However, the difference in dipole moments can be considered as the key factor in understanding the difference in electrostatic interactions at the cr-PVA/P3HT interfaces. LT-P3HT molecules, having a larger density of stronger dipole moments, may have more regioregularity defects positioned in regions of the cr-PVA substrate where strong dipole moments occur. The abrupt distortion of the LT-P3HT molecules at regioregularity defects, and the strong interaction between the large dipole moments of the LT-P3HT molecules with the dipole moments of cr-PVA can provide stabilization to the partial face-on orientation of molecules (orientation parallel with respect to the substrate, as illustrated in Figure 5.6). This would hinder molecular ordering and large crystallite formation, leading to lower molecular mobility (as observed for the LT-P3HT case; overall μ_{FET} is much lower than DF-P3HT OFETs; *vide supra*, Table 5.1). However, the interaction of these regioregularity defect dipoles with cr-PVA surface dipoles may also reduce the amplitude of electric potential that is capable of trapping charge carriers flowing at the cr-PVA/LT-P3HT interface. This partial passivation of electrostatic traps would favor the charge transport near the interface.

Table 5.2 Dipole moment magnitude per thiophene ring and average HOMO-LUMO energy gap of P3HT oligomers with 9 repeated units, as obtained by DFT method at the B3LYP/3-21G level of theory [160].

	Non-100% regioregular configuration	100% regioregular configuration
η(D) per thiophene ring	0.107	0.053
Average HOMO-LUMO gap	2.95 eV	2.70 eV
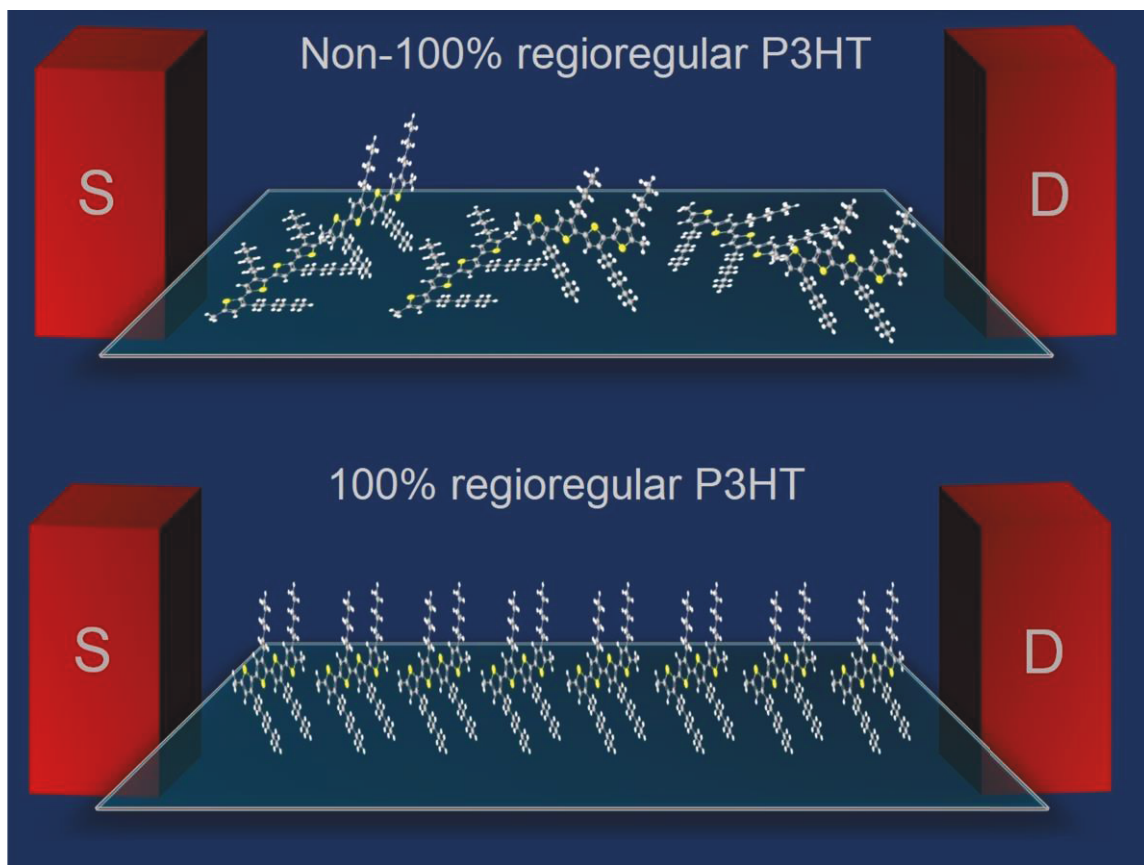
Figure 5.6 Illustration (lateral view) of P3HT molecular orientation (top) mixed edge-on and face-on orientation of non-100% regioregular P3HT molecules, and; (bottom) edge-on orientation of 100% regioregular P3HT molecules. S and D correspond to source and drain electrodes of OFET [160].

On the other hand, the lower torsional angles between adjacent thiophene rings, resulting in a highly planar structure of 100% regioregular structure, would cause the DF-P3HT chains to adopt an orientation perpendicular with respect to the substrate (edge-on orientation, as illustrated in Figure 5.6). This would result in improved π–conjugation lengths and close inter–molecular packing, leading to higher molecular mobility (as observed for the DF-P3HT case; overall μ_{FET} is much higher than LT-P3HT OFETs; *vide supra*, Table 5.1). However, the relatively low dipole moments produced by the 100% regioregular P3HT molecules, and the unfavorable orientation of the polymer's dipole relative to the cr-PVA surface dipoles, would not contribute to smooth the profile of the electrostatic potential at the cr-PVA/DF-P3HT interface. As a consequence, the charge transport near the cr-PVA/DF-P3HT interface would still be restricted by the presence of a higher density of electrostatic traps [160].

In summary, the less pronounced decrease in μ_{FET} (as $l_0 \rightarrow 0$) for LT-P3HT OFETs (Figure 5.2) is consistent with the above discussions of quantum chemical calculations. Face-

on oriented non-100% regioregular molecules bear high dipole moments and their interaction with cr-PVA dipoles contributes to the passivation of electrostatic traps at the cr-PVA/LT-P3HT interface. This passivation lowers the potential energy variations at the interface such that the decrease in μ_{FET} in this region is less pronounced (Figure 5.2). On the other hand, the lower dipole moments of DF-P3HT molecules do not contribute in passivating the electrostatic traps caused by the dipolar groups of cr-PVA. Hence, the potential energy variations are incremented at the cr-PVA/DF-P3HT interface, resulting in a sharp decrease in μ_{FET} (Figure 5.2).

5.4 Summary

Experimental results indicated that the interaction of DF-P3HT molecules with cr-PVA surface dipoles results in improvement of molecular order. As a result even for 20 nm DF-P3HT films, the OFET devices show high μ_{FET} values. However, the low dipole moments produced by highly planar DF-P3HT molecules are unfavorable for the passivation of dipolar traps produced by the surface of cr-PVA. Therefore, charge transport in these devices is still restricted by the presence of a higher density of electrostatic traps at the cr-PVA/DF-P3HT interface. On the other hand, the non-planar LT-P3HT molecules interact with the cr-PVA surface dipoles to stabilize the face-on orientation of the polymer molecules. The high disorder caused by the regioregularity defects resulted in an amorphous-like morphology when 20 nm LT-P3HT was used. Therefore, 20 nm LT-P3HT OFETs demonstrated a dramatic decrease in μ_{FET} when compared to thicker LT-P3HT devices. However, because of the regioregularity defects, the non-100% regioregular molecules produce relatively higher dipole moments, which interact with the dipoles of cr-PVA to reduce the potential energy variations at the cr-PVA/LT-P3HT interface, and slightly improve charge transport in this region. These results help in understanding the diverse mobility values reported in literature with various regioregularities of P3HT.

6

Ultra-high mobilities in defect-free poly(3-hexylthiophene-2,5-diyl) based transistors through application of supra-molecularly aligned polymer films

6.1 Introduction

Molecular alignment has proved to be an efficient approach to bring significant improvements in the crystallinities in P3HT thin films, and in the charge transport properties in OFETs [106,162–166]. One recently developed, cost-effective and simple, method to achieve molecular alignment in polymer films is the floating–film transfer method (FTM) [165,167–171]. In principle, FTM involves the formation of a thin floating–film of P3HT on top of a viscous hydrophilic substrate. Control over a few important parameters yields a uniform floating–film consisting of stretched and aligned macromolecules. The hydrophilic substrate can be water, ethylene glycol (Eg) and/or glycol (Gl); its choice may vary depending on the polymer whose floating–film has to be formed [168,171]. Initially, the polymer solution is dropped on top of the hydrophilic substrate, which rapidly expands followed by solidification and formation of a floating polymer film. The propagation of the polymer solution is controlled by the viscosity of the hydrophilic substrate, and the molecular interaction between the top layers of the hydrophilic substrate and the hydrophobic polymer molecules [169,171]. The viscosity of the hydrophilic substrate acts as a compressive external force, hindering the expansion of the polymer solution [169,171]. The resultant force due to simultaneous compression/expansion allows the alignment of polymer molecules perpendicular to the spreading direction of the polymer solution (as illustrated in Figure 6.1) [169,171]. The floating–film is then transferred onto the desired substrate by stamping, which permits the choice of aligning polymer molecules either parallel or perpendicular to the stamping direction.

In this Chapter, FTM is applied to align 100% regioregular DF-P3HT molecules, with the aim of producing high performance OFET devices.

6.2 Experimental

OFETs were prepared in bottom-gate top-contact geometry on top of glass substrates (schematic structure shown in Figure 3.1a). Fabrication procedure until the deposition of the gate insulator (cr-PVA) is described in Section 3.1. 100% regioregular defect-free P3HT (DF-P3HT; M_n: 41 kDa) was used as the active semiconducting layer of the OFETs. DF-P3HT was prepared in toluene, at a concentration of 7 mg/mL, by magnetically stirring the solution for 30 min at 60 °C. The deposition of DF-P3HT over the cr-PVA substrates was performed either by spin coating or by FTM. In the case of spin coating, the deposition was performed at 1500 rpm for 60 s. In the case of FTM deposition (flow chart shown in Figure 6.1), firstly a viscous solution of ethylene glycol (Eg) and glycerol (Gl) was prepared in a ratio of 3:1 by magnetically stirring the Eg:Gl solution at 60 °C. The DF-P3HT and Eg:Gl solutions were then cooled down to room temperature, and the Eg:Gl solution was poured into a petri dish. A droplet (~10 µL) of the DF-P3HT solution was dropped on top of the viscous Eg:Gl solution, which instantly expanded outward. The evaporation of solvent resulted in solidification of the DF-P3HT solution. ~1 cm^2 cr-PVA substrates were stamped onto the floating–film (Figure 6.1). Please note that the substrates were stamped on top of the floating–film, at the film/air
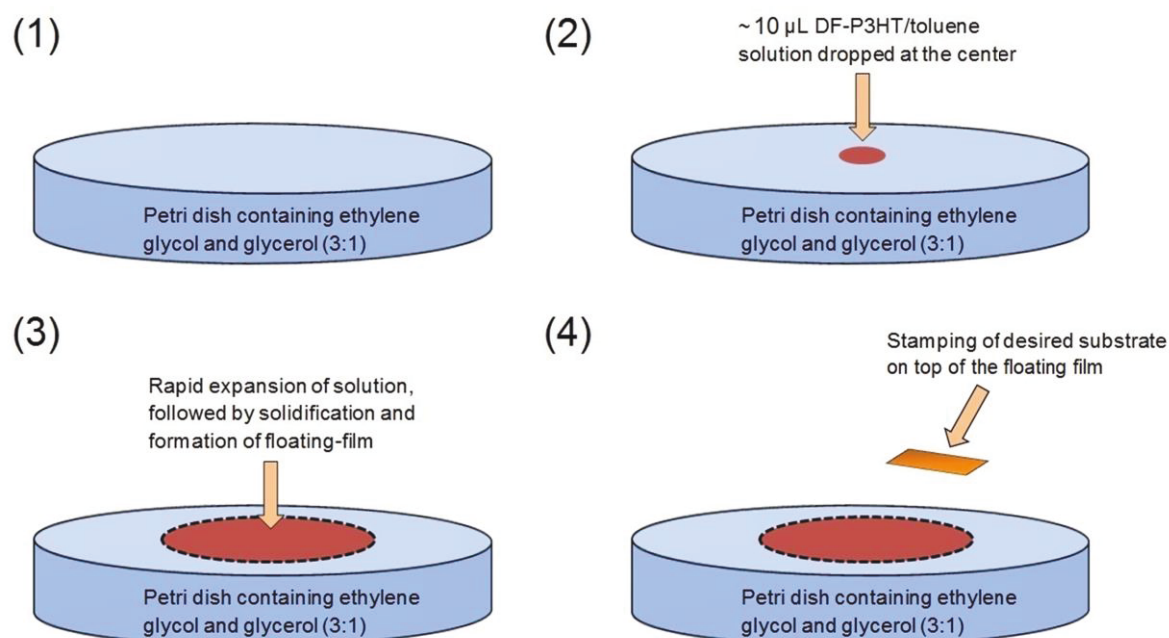
Figure 6.1 Flow diagram of the FTM deposition used for the formation of DF-P3HT floating–film over Eg:Gl hydrophilic substrate. The black dashed lines in (3) and (4) show the direction of molecular alignment.

interface. After the stamping of the floating–film, the substrates were dried by blowing air to remove any Eg:Gl residues. Both spin coated and FTM deposited DF-P3HT substrates were thermally annealed in vacuum for 30 min at 100 ºC. The thickness of the DF-P3HT layer was measured to be ~50 nm. Source and drain electrodes were formed by thermal evaporation of ~50 nm Au at a base pressure of 10^{-6} Torr.

Electrical characterization of OFETs was performed in dark ambient environment using a Keithley 2602 dual source meter. Capacitance was measured in Al/cr-PVA/Au (11 nF/cm^2) structure using an Agilent 4284-A LCR meter (operating at 1 kHz [139]). Capacitance of cr-PVA was also measured at 10 Hz (18 nF/cm^2) using a series RC circuit with R = 10 MΩ. An input voltage signal of the form $V = V_0 + V_A sin(2\pi ft)$ was applied where V_0 was adjusted to 1 V and V_A = 10 mV. Using a function generator, input signal of f = 10 Hz was applied to the capacitor, and the output across the resistor was analyzed using an oscilloscope. The time difference (δ) between the input and output sinusoidal waves was recorded in order to calculate the phase difference (∅), and thereafter the capacitance (Equations 6.1 and 6.2).

$$\emptyset = \frac{\delta 2\pi}{T},$$
(6.1)

$$C = \frac{1}{\omega R tan\emptyset}$$
(6.2)

The thicknesses of the thin films were measured using a BrukerDektakXT surface profiler. UV-vis absorbance spectra were analyzed using a Perkin Elmer LAMBDA 950 UV/Vis/NIR Spectrophotometer, and AFM images were taken using a Shimadzu SPM-9500J3 scanning probe microscope at Laboratório de Propriedades Ópticas, Eletrônicas e Fotônica – UFPR and Centre for Electronic Microscopy (CME-UFPR), respectively. X-ray Diffraction (XRD) patterns of DF-P3HT films were recorded over SiO$_2$ substrates using Cu Kα X-ray radiation (λ: 1.5406 Å) at Laboratório de Óptica de Raios X e Instrumentação – UFPR. In the case of out-of-plane XRD measurements, a D8 ADVANCE BRUKER Diffractometer was used. The incident angle was fixed at 2.5°, while 2θ varied from 3° to 25°. In the case of in-plane XRD measurements, a D8 DISCOVER BRUKER Diffractometer was used; the incident angle was fixed at 5°, while 2θ varied from 15° to 45°.

6.3 Results and Discussions

The photographic image of solidified DF-P3HT floating–film over Eg:Gl (3:1) hydrophilic substrate is shown in Figure 6.2a. The surface morphologies obtained by stamping cr-PVA substrates onto the three regions of the floating–film (central, intermediate and outer) are shown in Figure 6.2b-d. The central region of the floating–film shows the presence of densely packed grains having average sizes of ~3-4 μm. The intermediate region shows highly stretched branch-like structures (some structures longer than 10 μm), while the outer region shows smaller grains typically of sizes less than 1 μm. The morphology obtained for the spin coated film shows a nodule-like morphology with grain sizes of ~2 μm (Figure 6.2e).

The different morphologies observed for the three regions of the floating–film suggest that different mechanisms are present in the formation of each region. This can be understood by analyzing the process through which the floating–film solidifies over the Eg:Gl substrate. It was observed during the experiments that, after the expansion of the polymer solution, the solidification starts from the outer region of the floating–film and proceeds towards the inner region (also reported earlier [168]). The solidification of the outer region starts from its outside boundaries and goes until the onset of the intermediate region. The compression force applied by the hydrophilic substrate causes majority of the polymer solution to accumulate and form the intermediate and the central regions of the floating–film. This results in the formation of a very thin film in the outer region. After the outer region, the intermediate region starts solidifying from its outside boundaries and goes until the onset of the central region. In this context, the solidification process of the outer and the intermediate region follows the same order (from their outside boundaries to the onset of the next region). For this reason similar surface morphology is observed in these regions, in that, alignment of polymer grains is present in both cases. However, the intermediate region not only exhibits presence of alignment, but also large and stretched domains (Figure 6.2c), which means that the formation of this region constitutes the optimal rate of expansion/compression and solvent evaporation. On the other hand, the central region solidifies at the end, from its outside boundaries to the center of the floating–film. Unlike the intermediate region, the solidification of the central region does not meet the required conditions for the polymer chains to organize into aligned domains (Figure 6.2b). Nevertheless, grain size in the central region (~3-4 μm, Figure 6.2b) is still bigger compared to the spin coated film (~2 μm, Figure 6.2e).
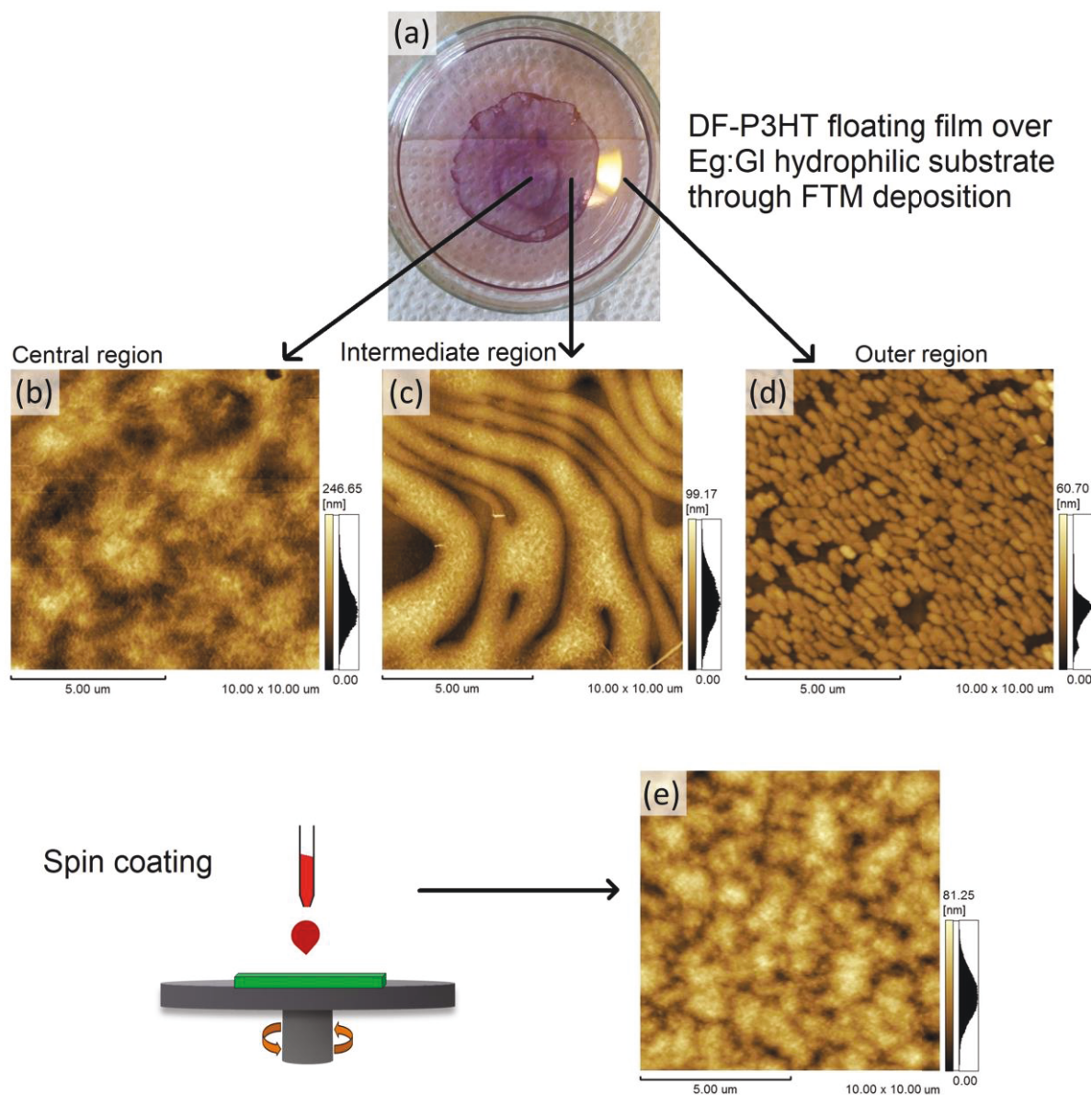
Figure 6.2 (a) Image of solidified DF-P3HT film floating over Eg:Gl (3:1) hydrophilic substrate. Tapping mode AFM images of (b) the central region of the floating–film (R_{rms}: 34 nm); (c) the intermediate region of the floating–film (R_{rms}: 15 nm); (d) the outer region of the floating–film (R_{rms}: 7 nm), and; (e) the spin coated film (R_{rms}: 12 nm) [161].

Alignment of DF-P3HT molecules in the intermediate region of the floating–film was investigated using UV-vis polarized absorbance spectroscopy (Figure 6.3). Figure 6.3a illustrates the direction of the alignment of polymer molecules with respect to the expansion of polymer solution; Figure 6.3b illustrates the direction of FTM deposited DF-P3HT films with respect to the linearly polarized light, and; Figure 6.3c shows the polarized absorbance spectra. In the case of FTM deposited films, it can be seen that, when the direction of polymer
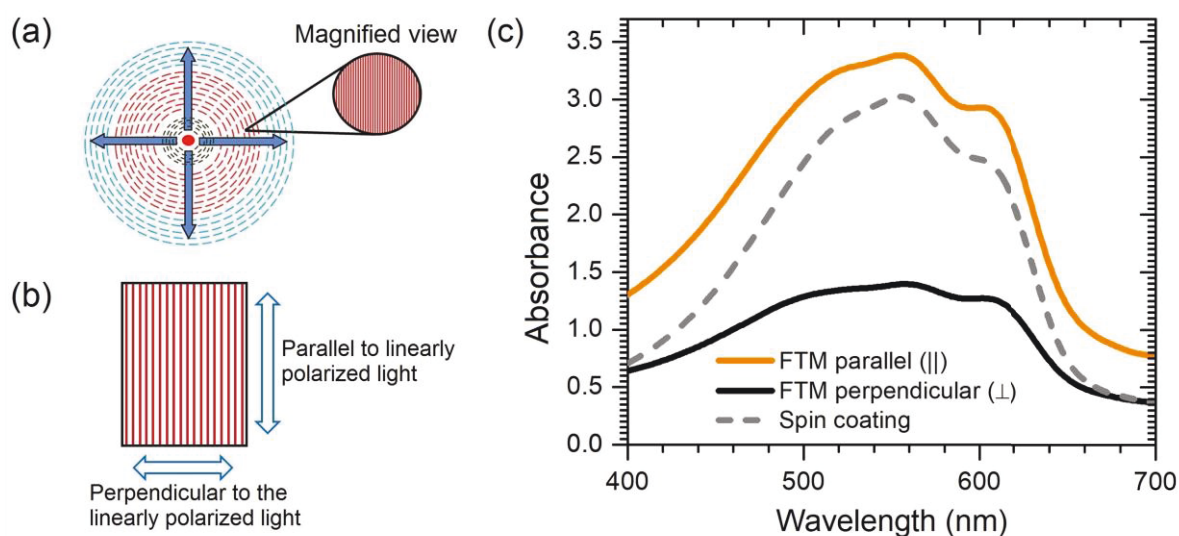
Figure 6.3 (a) Schematic illustration of film formation. Dashed lines correspond to polymer chain alignment direction, and blue arrows correspond to the direction of solution expansion; (b) schematic illustration of DF-P3HT film direction showing the predominant direction of polymer chains with respect to the linearly polarized light during polarized absorbance spectroscopy, and; (c) polarized light UV-vis absorbance spectra of FTM deposited DF-P3HT films (intermediate region), where the direction of aligned polymer chains is parallel (∥) or perpendicular (⊥) to the electric field. For comparison, the absorbance spectrum of spin coated DF-P3HT film is also shown [161].

molecules is parallel to the linearly polarized light, the absorption peak at ~550 nm is ~2.5 times more intense than the perpendicular direction. The anisotropic absorbance spectra evidences directional aligment of polymer molecules in FTM deposited films (Figure 6.3c). Compared to the absorbance spectrum of the spin coated film, the absorbance spectrum of the FTM deposited film shows an increase in the relative intensity of the first vibronic peak (at ~610 nm), which indicates improvement of the inter–chain molecular order [33].

The structural order in spin coated and FTM deposited DF-P3HT thin films was further investigated using out-of-plane XRD experiments (Figure 6.4). The diffraction peaks at $2\theta \approx 5.3°$ correspond to the (100) alkyl chain direction [133]. The crystallite sizes for DF-P3HT deposited through FTM and spin coating were estimated to be equal (~80 Å). Furthermore, the peak positions of (100) diffraction peaks are also equal for both cases. This is an indication that FTM deposition does not effect the crystallite size or the crystal structure in the (100) alkyl chain direction.
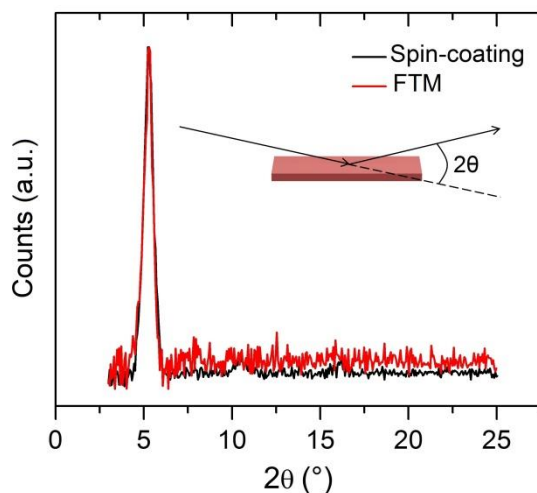
Figure 6.4 Bragg-Brentano θ-2θ out-of-plane XRD patterns of DF-P3HT thin films prepared with spin coating and FTM. Inset shows the geometry of the XRD experiment. Note that the patterns are normalized [161].

In-plane XRD experiments were performed on the spin coated and FTM deposited films to further investigate the alignment of polymer molecules. These experiments were performed in four sample directions, as illustrated in the insets of Figure 6.5. The sample was rotated 90° each time, while the incident ray was fixed. For the case of FTM deposited DF-P3HT film, when the sample was positioned such that the molecules were aligned perpendicular to the incident ray, a diffraction peak at 2θ ≈ 28° was recorded, which can be attributed to diffraction from the (010) π–π stacking direction of DF-P3HT molecules (Figure 6.5a,c). On the other hand, when the sample was positioned such that the molecules were aligned parallel to the incident ray, no diffraction peak was recorded (Figure 6.5b,d). This is another indication—in addition to the polarized absorbance results—of unidirectional molecular alignment in FTM deposited films.

In the case of spin coated film, the in-plane XRD results are shown in Figure 6.6, together with the corresponding sample positions. In this case, the diffraction peaks at 2θ ≈ 29° and 2θ ≈ 34° were recorded in all four directions of the sample, which was expected, since spin coating produces random alignment of polymer crystallites. Furthermore, the in-plane diffraction data shows difference in both the shape and the positions of the diffraction peaks of the FTM deposited and spin coated films. These features suggest that FTM deposition modifies both the crystal size and the crystal structure in the (010) π–π stacking direction.
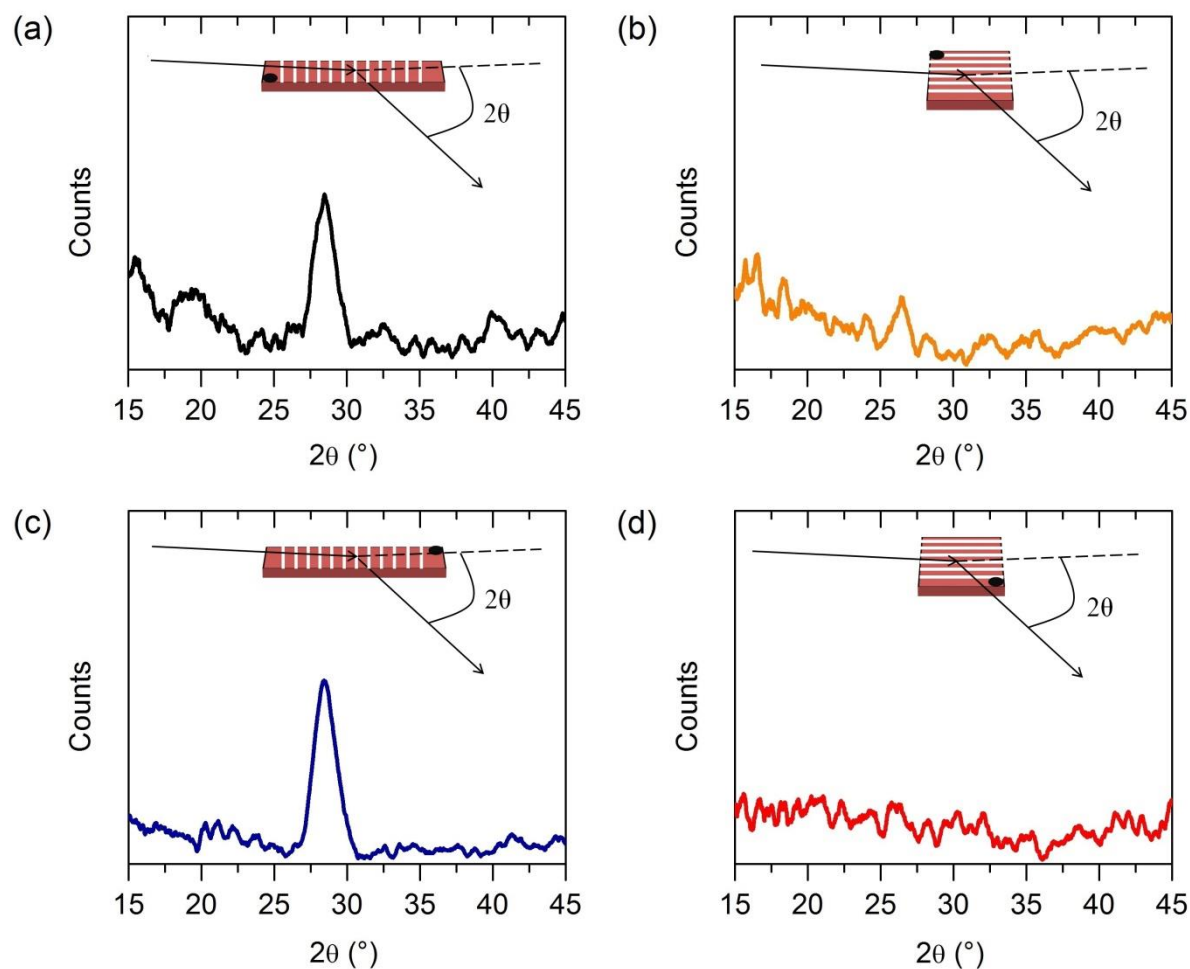
Figure 6.5 θ-2θ in-plane XRD patterns of FTM deposited DF-P3HT thin film in four sample positions with respect to the incident ray. The sample positions are shown in the insets, where the white lines correspond to the direction of molecular alignment. The measurements were performed in the following order: (a) Position 1, molecular alignment perpendicular to the incident ray; (b) position 2, molecular alignment parallel to the incident ray; (c) position 3, molecular alignment perpendicular to the incident ray, and; (d) position 4, molecular alignment parallel to the incident ray [161].
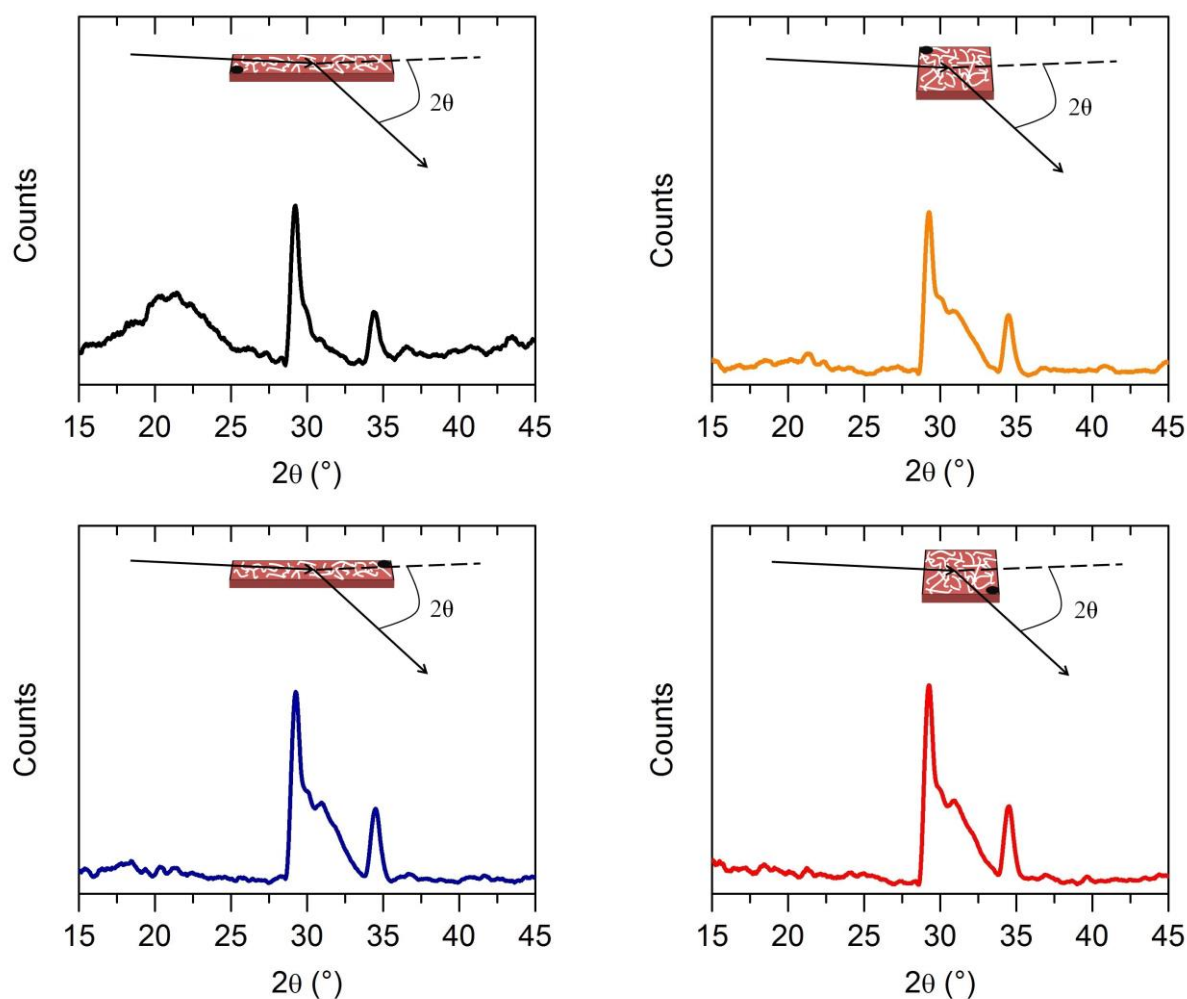
Figure 6.6 θ-2θ in-plane XRD patterns of spin coated DF-P3HT thin film showing molecular isotropy, since scattering peaks are recorded in all four sample positions. Insets show the geometries of the XRD experiments. The black dots indicate the relative positions of the sample, while it was rotated 90 degrees each time. The white lines illustrate the random organization of DF-P3HT molecules [161].

Before the discussion of OFET electrical characteristics, it is important to remember that the deposition of DF-P3HT through FTM was performed by stamping the cr-PVA substrates on top of the floating–film (as shown in Figure 6.7a). The other main point is that polymer molecules in the floating–film align perpendicular to the expansion of the polymer solution (Figure 6.7a). The top electrodes of OFET devices were then deposited over the DF-
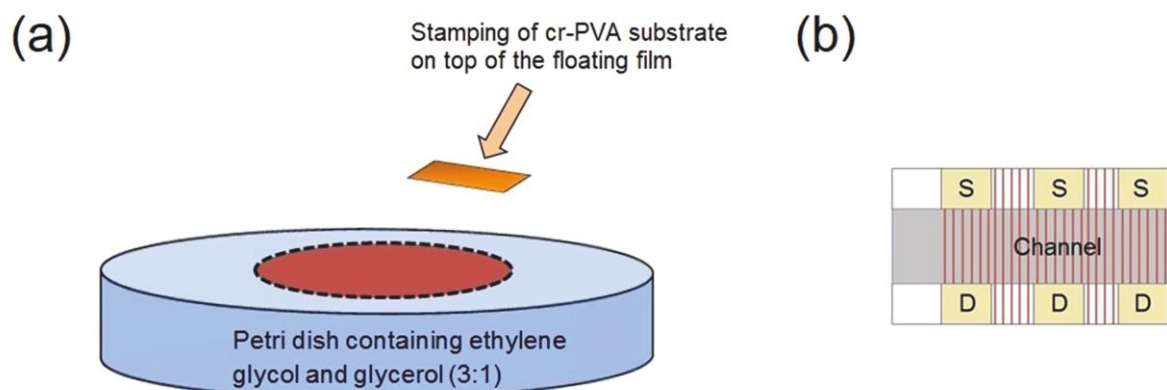
Figure 6.7 (a) For OFET devices, deposition of DF-P3HT through FTM is performed by stamping the cr-PVA substrates on top of the floating–film. Please note that the direction of molecular alignment is perpendicular to the expansion of the solution (represented by the black dashed lines), and; (b) source and drain electrodes are then deposited over the DF-P3HT films, such that the molecules are aligned in the charge transport direction (as illustrated by the red stripes) [161].
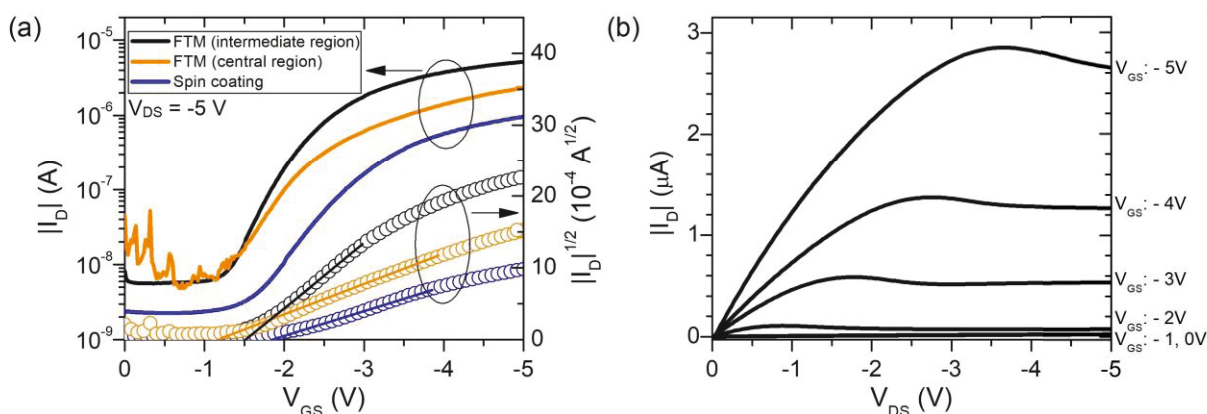
Figure 6.8 OFET electrical characteristics: (a) $I_D \times V_{GS}$ and $|I_D|^{1/2} \times V_{GS}$ of OFETs prepared with spin coating and FTM (gate leakage current ($I_G \times V_{GS}$) in all of the cases was observed as ~20 nA), and; (b) I_D-V_{DS} of OFET prepared with FTM (intermediate region of the floating–film).

P3HT film, such that the alignment of polymer chains is in the charge transport direction between the source and drain electrodes (as illustrated in Figure 6.7b). Then, the application of longitudinal electric field corresponds to the direction of aligned molecular assemblies, and the charge carriers are transported dominantly through the lower resistance intra–chain pathway (along the π–conjugated backbone) [172].

Figure 6.8 shows the electrical characteristics of OFETs where DF-P3HT was deposited either through FTM (intermediate and central regions of the floating–film (Figure

6.2a for reference)) or through spin coating. The devices prepared with the outer region of the floating–film showed low I_D (~1 × 10^{-7} A). Compared to the spin coated devices, improvement in I_D by a factor of ~4 and μ_{FET} by a factor of ~6 was observed when DF-P3HT was deposited using the intermediate region of the floating–film in FTM. The OFETs prepared with the central region of the floating–film also showed improvement in I_D (by a factor of ~2) and μ_{FET} (by a factor of ~3) when compared to the spin coated devices. The results are summarized in Table 6.1. FTM deposition has also previously been applied for the deposition of few other polymeric materials, where successful alignment of polymer molecules and improvement in μ_{FET} was demonstrated (Table 6.2).

Table 6.1 Summary of the performance parameters of OFET devices prepared with FTM deposition and spin coating [161].

OFET prepared with	ι_{FET} (cm^2/V.s)	V_T (V)	I_{on}/I_{off}	SS (V/dec)	g_m (μS)
Spin coating	1.1 ± 0.2	1.9 ± 0.2	1040 ± 620	1.1 ± 0.2	0.6 ± 0.1
FTM (intermediate region)	6.3 ± 1.5	1.9 ± 0.6	1830 ± 900	1.3 ± 0.5	1.1 ± 0.3
FTM (central region)	3.1 ± 0.4	1.4 ± 0.3	1320 ± 400	1.1 ± 0.2	0.8 ± 0.2

Table 6.2 Dichroic ratio (DR) of various polymers deposited using FTM and μ_{FET} of corresponding OFET devices.

Polymer	Deposition	DR	μ_{FET} (cm^2/V.s)	Ref.
DF-P3HT	Spin coating	-	1.2	[81]
	FTM	~2.5	8.0	This project
P3HT	Spin coating	-	2.1×10^{-5}	[165]
	FTM	8.3	3.4×10^{-3}	
P3HT	FTM	5.8	-	[169]
PQT-C12	FTM	6.4	-	[169]
PBTTT-C14	FTM	5.1	-	[169]
P3HT	FTM	1.5	-	[169]
P3HT	Spin coating	-	2.5×10^{-3}	[170]
	FTM	-	5.3×10^{-2}	
F8T2	Spin coating	-	2.2×10^{-4}	[173]
	FTM	~3	2.6×10^{-3}	

In addition to the molecular alignment, there is a possibility that the FTM deposition also promotes improvement in self-organization and edge-on orientation of DF-P3HT molecules. In principle, during the floating–film formation, the FTM deposition allows slower solvent evaporation, which is known to facilitate slower film growth, providing a longer time for the polymer molecules to self-organize [50]. On the other hand, in the case of spin coating, self-organization of polymer molecules is hindered because of the rapid solvent evaporation and radial velocity of the polymer solution during the drying process [39]. The other important point is the orientation of polymer molecules at the polymer/air and polymer/insulator interfaces. It is known that the polymer/air interface consists of much more pronounced edge-on orientation of P3HT molecules (with lower torsional angles, higher π– conjugation lengths and better inter–molecular packing) when compared to the polymer/insulator interface [174,175]. Contrary to spin coating, in the case of FTM deposition, before the DF-P3HT floating–film is stamped onto the desired substrate, it forms an interface with air. After the stamping of the floating-film, the former polymer/air interface—consisting of much more pronounced edge-on oriented molecules—becomes the polymer/insulator interface, which would concomitantly improve the charge transport properties in the conducting channel of the transistors. In view of the above, it is possible that the slow solvent evaporation and the action of polymer/air interface may also be playing a role in the improvement of μ_{FET} in FTM processed OFETs.

It was previously reported that PVA gate insulator contains mobile ions [176]. The synthesis of PVA, in principle, results in the incorporation of sodium acetate (NaAc) in its chemical structure that contains Na^+ ions. These ions exhibit a low mobility [176], and therefore, when the transistors are electrically characterized, the ions may contribute to
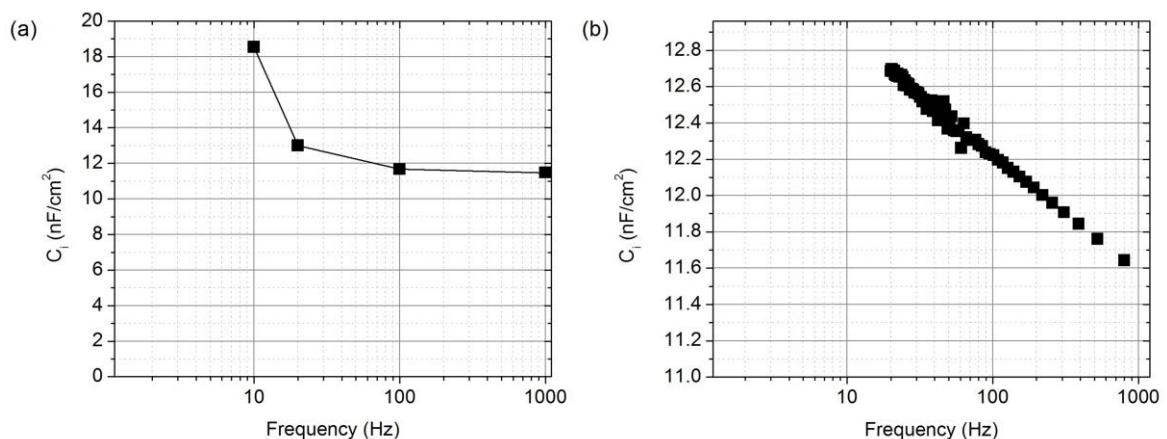
Figure 6.9 $C_i \times f$ of cr-PVA; (a) measured down to 10 Hz using an RC circuit, and; (b) measured down to 20 Hz using an LCR meter.

changing the capacitance of cr-PVA, and the effective charge transport, by diffusing into the DF-P3HT layer. In this work, the capacitance of cr-PVA was measured at 1 kHz, while the transistors were measured relatively slowly (sweeping rate of 200 ms per point), which could allow for ionic motion and hence higher charge carrier density. In order to remove this discrepancy, the capacitance measurements were additionally performed at 10 Hz (experimental procedure described in Section 6.2). The capacitance of cr-PVA measured at 10 Hz (18 nF/cm^2) was found to be only ~1.5 times higher compared to when measured at 1 kHz (11 nF/cm^2) (Figure 6.9). This indicates that, until 10 Hz, the contribution of mobile ions is not dominant. The average μ_{FET} of OFET devices for the capacitance value obtained at 10 Hz was calculated as 3.8 cm^2/V.s.

Table 6.3 μ_{FET} values of P3HT based OFETs obtained by some other groups.

P3HT regioregularity	Gate insulator	μ_{FET} (cm^2/V.s)	Ref.
91%	SiO$_2$	0.10	[31]
98.5%	SiO$_2$	0.20	[39]
98%	SiO$_2$	0.12	[40]
98%	SAM/SiO$_2$	0.28	[42]
P3HT from Reike materials	Ion gel[7]	1.80	[177]
98%	PMMA	0.40	[45]
P3HT from Plextronics Plexcore	SiO$_2$	0.10	[178]

Table 6.4 μ_{FET} values of cr-PVA/P3HT based OFETs obtained in the Group of Organic Optoelectronic Devices. The processing of cr-PVA followed the same procedure, while only the P3HT supplier or batch was changed.

P3HT regioregularity	Supplier	μ_{FET} (cm^2/V.s)	Ref.
90%	Sigma-Aldrich	0.08	[10]
90%	Sigma-Aldrich	0.13	[53]
90%	Sigma-Aldrich	0.05	[113]
90%	Sigma-Aldrich	0.07	[179]
98%	Sigma-Aldrich	0.12	[81]
100%	Kumar´s Group	1.20	[81]
100%	Kumar´s Group	0.50	[160]

---

[7] The authors applied an ion-gel as the gate insulator, which strongly influenced the μ_{FET} value.

The cross-linking process of PVA was developed in the Group of Organic Optoelectronic Devices precisely to control the effect of impurities and defects on electrical properties of transistor devices [53]. For this reason, even at substantially low frequencies (10 Hz), where the mobile ions tend to be more active [53], the increase in capacitance is only by a factor of ~1.5. In addition, the capacitance of cr-PVA measured at 1 kHz follows the IEEE standard for test methods for the characterization of organic transistors and materials [139], and it allows a direct comparison with the results available in the literature. In this context, a few μ_{FET} values obtained by other groups are listed in Table 6.3, and the published μ_{FET} values obtained in the Group of Organic Optoelectronic Devices are listed in Table 6.4. It can be seen that the μ_{FET} values obtained in the Group of Organic Optoelectronic Devices are comparable to those of other groups, except in the case of 100% regioregular material when results are better (Table 6.3 and 6.4). Keeping in view the above discussions and the comparison of results in Table 6.3 and Table 6.4, one can directly infer that the remarkably high μ_{FET} values obtained in the present work are principally due to the FTM deposition of DF-P3HT. In this context, to allow a direct comparison with the results available in the literature, it is more appropriate to consider the μ_{FET} values calculated for capacitance at 1 kHz (Table 6.1).

6.4 Summary

In this work, floating–film transfer method (FTM) was used to prepare supra-molecularly aligned films of DF-P3HT. OFETs based on FTM deposited DF-P3HT demonstrate μ_{FET} values as high as 8 cm^2/V.s, which is the highest ever reported for P3HT based OFETs, and among one of the highest reported for polymeric semiconductor based OFETs (Table 6.5; next page). Majority of the previously reported high μ_{FET} values arise from sophisticated and high-cost experimental techniques. Comparatively, P3HT is an extensively available and investigated polymer, and the synthesis of DF-P3HT *via* continuous flow method is reasonably cost-effective and facile. Similarly, FTM is an inexpensive and environmentally friendly deposition technique, and results in much less wastage of material when compared to many other deposition techniques. For this reason, the high μ_{FET} of the current work is an attractive prospect for the integration of DF-P3HT OFETs in next-generation flexible electronic applications like OLED displays.

Table 6.5 Some of the highest reported μ_{FET} values for polymer based OFET devices. Highlighted rows indicate μ_{FET} values obtained during this project.

OFETs based on polymer	Gate insulator	μ_{FET} (cm^2/V.s)	Ref.
PDPP-TNT	OTS/SiO$_2$	1.00	[180]
DF-P3HT	cr-PVA	1.20	[81]
RP33	ODTS/SiO$_2$	1.37	[181]
PDBFBT	OTS/SiO$_2$	1.54	[182]
PSeDPP	ODTS/SiO$_2$	1.62	[24]
P3HT	Ion-gel	1.80	[177]
pDPPT2TT-OD	ODTS/SiO$_2$	1.93	[183]
PDPPCp	CYTOP	3.00	[184]
PDPPF-DTT	OTS/SiO$_2$	3.56	[26]
IIDDT-C3	–	3.62	[185]
DF-P3HT	cr-PVA	8.00	[161]
PDVT-10	OTS/SiO$_2$	8.00	[25]
DPP-DTT	OTS/SiO$_2$	10.50	[186]
C20, P2 substituted CDT-BTZ	SiO$_2$	11.40	[27]
PCDTPT	DTS/SiO$_2$	23.70	[18]

7

Conclusions

This project aimed at the performance enhancement of cr-PVA/P3HT based OFETs through improvement of charge transport properties. Experimental investigations were performed using both non-100% and 100% regioregular P3HT. The 100% regioregular DF-P3HT was synthesized by the group of Prof. Anil Kumar. It was observed that DF-P3HT based OFETs demonstrate significantly improved performances when compared to non-100% regioregular P3HT based devices. The field-effect mobility (μ_{FET}) in DF-P3HT devices, without any additional treatment, was obtained as 1.20 cm^2/V.s (on average), which is ~10 times higher than non-100% regioregular P3HT based devices. The remarkable improvement in device performance originates from the absence of regioregularity or π–conjugation defects, which otherwise appear along the polymer chains in the non-100% regioregular material. Correspondingly, the UV-vis absorbance spectroscopy, XRD and AFM experiments demonstrated that, when compared to non-100% regioregular P3HT films, the DF-P3HT films consist of a much lesser fraction of disordered unaggregated molecules, which consequently helps in the formation of well-defined and bigger crystallites.

In order to investigate improvement of charge transport properties at the insulator/semiconductor (I/S) interface of OFETs, surface treatment for the gate insulator (cr-PVA) layer was applied using a cationic surfactant, hexadecyltrimethylammonium bromide (CTAB). The idea was to passivate the cr-PVA surface traps (dipoles) that modify the polarization energies of adjacent polymer molecules, and consequently result in the localization of charge carriers at the I/S interface. In the case of 98% regioregular EG-P3HT based devices, the surfactant treatment resulted in improvement of μ_{FET} by a factor of ~3, and the subthreshold swing (*SS*) values indicated lower density of charge traps at the I/S interface, when compared to untreated devices. Similarly, careful analysis of $\mu_{FET} \times l_0$ data suggested that the CTAB treatment results in a decrease in the potential energy variations at the I/S interface. On the other hand, when the same treatment was applied in DF-P3HT based

OFETs, the devices showed reduction in μ_{FET}. This point raised a concern regarding the interaction of cr-PVA surface traps and P3HT"s regioregularity defects.

In order to address this issue, molecular interactions at the cr-PVA/P3HT interface were investigated for 93% regioregular LT-P3HT and DF-P3HT. The experimental results and quantum chemical calculations demonstrated that non-100% regioregular P3HT molecules consist of higher torsional angles between adjacent thiophene rings, which results in a non-planar polymer backbone. Consequently, the molecules partially adopt a face-on orientation (parallel with respect to the substrate), and in addition produce high dipole moments. This was an interesting finding, since the interaction of the high dipole moments produced by non-100% regioregular P3HT molecules with cr-PVA surface dipoles would, in principle, play a strong role in the passivation of electrostatic traps at the I/S interface. In comparison, 100% regioregular P3HT molecules demonstrated highly planar structure and low dipole moments, which would not contribute to smooth the profile of the electrostatic potential energy variations at the I/S interface. Correspondingly, the analysis of OFET charge transport properties showed that decrease in μ_{FET} close to the I/S interface is less pronounced in LT-P3HT devices compared to the DF-P3HT devices.

In the last part of the research project, the deposition technique (floating–film transfer method (FTM)) was experimented to prepare molecularly aligned films of DF-P3HT. Compared to other sophisticated and expensive techniques reported in the literature, FTM is an extremely simple and inexpensive technique. By dropping the polymer solution on top of a hydrophilic substrate (ethylene glycol + glycerol), unidirectional alignment was obtained in a floating–film. Sequentially, desired substrates were stamped on top of the floating–film to complete the deposition process. Molecular alignment was confirmed through AFM, polarized absorbance spectroscopy and in-plane XRD experiments. The application of aligned DF-P3HT films in OFET devices resulted in significantly improved device performances, showing μ_{FET} values as high as 8 cm^2/V.s. The μ_{FET} values reported in this project are the highest ever reported for P3HT based OFETs. This can be considered as an important breakthrough since it implies that, with DF-P3HT, slight modifications of experimental methods can lead to remarkable device performances. Among other important industrial applications, the μ_{FET} values obtained in this project are sufficient for integration of these OFETs in organic light emitting diode (OLED) displays.

Future directions

Following are some of the potential future works associated to this project:

1. Investigation regarding the affect of different molecular weights of DF-P3HT on OFET performance. It would be interesting to study the role of the regioregularity of P3HT in this investigation.

2. In the case of surfactant treatment of cr-PVA, it would be interesting to investigate how the surfactant molecules (or micelles) affect the morphology of the P3HT layer.

   - Surfactant molecules (or micelles) may also be producing polarization effects at the I/S interface, since it was observed in the beginning of this project that CTAB treated devices, utilizing non-100% regioregular P3HT, can demonstrate (under certain conditions) μ_{FET} of ~3 cm^2/V.s.

3. At the start of this project, it was also observed that CTAB treated OFET devices (in some cases) demonstrate a big hysteresis in the transfer characteristics ($I_D \times V_{GS}$). The hysteresis in some cases corresponded to ~4 V (V_{GS}), and in addition, the I_{on}/I_{off} was recorded as several orders of magnitude (~10^4). It appears that CTAB molecules (or micelles) have the tendency to trap charge carriers. Controlling certain experimental conditions may lead to the preparation of memory devices.

4. In the case of device processing through FTM, it would be interesting to produce aligned films of CTAB. Aligned and organized morphology of CTAB would potentially further improve OFET properties (particularly μ_{FET}).

5. FTM deposition can also be investigated to prepare thicker or thinner floating–films of P3HT, and how it influence OFET properties.

6. FTM deposition may also be experimented on other materials, such as carbon nanotubes.

7. FTM processed OFETs, when operated in the linear regime (V_{DS} = - 0.5 V) always demonstrated very low I_{off} and large hysteresis. This behavior may be controlled to develop memory devices.

8. In the case of the influence of cr-PVA ions on OFET μ_{FET}, it would be constructive to experiment other polymer gate insulators, aiming towards reducing the effect of mobile ions on charge accumulation and OFET μ_{FET}.

9. It may be considered necessary to perform an experimental investigation regarding the stability of P3HT based OFETs. In order to improve the stability, the devices can be encapsulated using polyisobutene, as reported by Toniolo *et al.* [187]. In addition, a device encapsulation can also be achieved by using a particular device structure (*e.g.* top-gate bottom-contact), such that the gate dielectric layer encapsulates the active polymer layer.

10. In order to further investigate the μ_{FET} of OFETs, it would be interesting to consider if/how the diffusion of Au atoms into the P3HT layer (during the thermal evaporation) influences the μ_{FET} behavior as a function of channel bottleneck thickness (l_0).

References

[1]   J. Bardeen, W.H. Brattain, Phys. Rev. 74 (1948) 230–231.

[2]   D. Kahng and M. M. Atalla, in:, IRE Solid-State Device Research Conference, Carnegie Institute of Technology, Pittsburgh, 1960.

[3]   J. E. Lilienfield, US Patent, 1745174, 1930.

[4]   D.F. Barbe, C.R. Westgate, J. Phys. Chem. Solids 31 (1970) 2679–2687.

[5]   H. Koezuka, A. Tsumura, T. Ando, Synth. Met. 18 (1987) 699–704.

[6]   G. Horowitz, X. Peng, D. Fichou, F. Garnier, J. Appl. Phys. 67 (1990) 528–532.

[7]   A. Dodabalapur, L. Torsi, H.E. Katz, Science 268 (1995) 270–271.

[8]   H. Sirringhaus, N. Tessler, R. Friend, Science 280 (1998) 1741–4.

[9]   R.C.G. Naber, C. Tanase, P.W.M. Blom, G.H. Gelinck, A.W. Marsman, F.J. Touwslager, S. Setayesh, D.M. de Leeuw, Nat. Mater. 4 (2005) 243–248.

[10]   W.S. Machado, I.A. Hümmelgen, IEEE Trans. Electron Devices 59 (2012) 1529–1533.

[11]   G. Horowitz, Adv. Mater. 10 (1998) 365–377.

[12]   W.S. Wong, A. Salleo, Flexible Electronics: Materials and Applications, Springer US, 2009.

[13]   S. Utsunomiya, S. Inoue, T. Shimoda, J. Soc. Inf. Disp. 10 (2002) 69.

[14]   H. Klauk, Organic Electronics: Materials, Manufacturing, and Applications, Wiley-VCH, 2006.

[15]   D. Braga, G. Horowitz, Adv. Mater. 21 (2009) 1473–1486.

[16]   H. Sirringhaus, Adv. Mater. 26 (2014) 1319–1335.

[17]   Y. Yuan, G. Giri, A.L. Ayzner, A.P. Zoombelt, S.C.B. Mannsfeld, J. Chen, D. Nordlund, M.F. Toney, J. Huang, Z. Bao, Nat. Commun. 5 (2014) 3005.

[18]   H.-R. Tseng, H. Phan, C. Luo, M. Wang, L.A. Perez, S.N. Patel, L. Ying, E.J. Kramer, T.-Q. Nguyen, G.C. Bazan, A.J. Heeger, Adv. Mater. 26 (2014) 2993–2998.

[19]   R. H. Friend, in:, I.L. and B.R. W. R. Salaneck (Ed.), Oxford Science Publications, 1993.

[20]   G. P. Crawford, Flexible Flat Panel Display Technology, Wiley-VCH, New York, 2005.

[21] C.K. Chiang, C.R. Fincher, Y.W. Park, A.J. Heeger, H. Shirakawa, E.J. Louis, S.C. Gau, A.G. MacDiarmid, Phys. Rev. Lett. 39 (1977) 1098–1101.

[22] T. Ito, H. Shirakawa, S. Ikeda, J. Polym. Sci. Polym. Chem. Ed. 12 (1974) 11–20.

[23] P. Bernier, G. Bidan, S. Lefrant, Advances in Synthetic Metals: Twenty Years of Progress in Science and Technology, 1999.

[24] H.-W. Lin, W.-Y. Lee, W.-C. Chen, J. Mater. Chem. 22 (2012) 2120–2128.

[25] H. Chen, Y. Guo, G. Yu, Y. Zhao, J. Zhang, D. Gao, H. Liu, Y. Liu, Adv. Mater. 24 (2012) 4618–4622.

[26] P. Sonar, J. Chang, Z. Shi, E. Gann, J. Li, J. Wu, C.R. McNeill, J. Mater. Chem. C 3 (2015) 9299–9305.

[27] Y. Yamashita, F. Hinkel, T. Marszalek, W. Zajaczkowski, W. Pisula, M. Baumgarten, H. Matsui, K. Müllen, J. Takeya, Chem. Mater. 28 (2016) 420–424.

[28] H. Yang, T.J. Shin, L. Yang, K. Cho, C.Y. Ryu, Z. Bao, Adv. Funct. Mater. 15 (2005) 671–676.

[29] R. Hamilton, M. Heeney, T. Anthopoulos, I. McCulloch, in:, Franky So (Ed.), Taylor & Francis, 2010.

[30] T.J. Prosa, M.J. Winokur, J. Moulton, P. Smith, A.J. Heeger, Macromolecules 25 (1992) 4364–4372.

[31] H. Sirringhaus, P.J. Brown, R.H. Friend, M.M. Nielsen, K. Bechgaard, B.M.W. Langeveld-Voss, A.J.H. Spiering, R.A.J. Janssen, E.W. Meijer, P. Herwig, D.M. de Leeuw, Nature 401 (1999) 685–688.

[32] J.M. Verilhac, G. LeBlevennec, D. Djurado, F. Rieutord, M. Chouiki, J.P. Travers, A. Pron, Synth. Met. 156 (2006) 815–823.

[33] P.J. Brown, D.S. Thomas, A. Köhler, J.S. Wilson, J.-S. Kim, C.M. Ramsdale, H. Sirringhaus, R.H. Friend, Phys. Rev. B 67 (2003) 64203.

[34] Y.-K. Lan, C.H. Yang, H.-C. Yang, Polym. Int. 59 (2010) 16–21.

[35] A. Salleo, R.J. Kline, D.M. DeLongchamp, M.L. Chabinyc, Adv. Mater. 22 (2010) 3812–3838.

[36] D.P. McMahon, . . heung, . or is, J. a cu a, . alleo, . Troisi, J. Phys. hem. C 115 (2011) 19386–19393.

[37] C. Poelking, D. Andrienko, Macromolecules 46 (2013) 8941–8956.

[38] P. Kohn, S. Huettner, H. Komber, V. Senkovskyy, R. Tkachov, A. Kiriy, R.H. Friend, U. Steiner, W.T.S. Huck, J.U. Sommer, M. Sommer, J. Am. Chem. Soc. 134 (2012) 4790–4805.

[39]   G. Wang, J. Swensen, D. Moses, A.J. Heeger, J. Appl. Phys. 93 (2003) 6137–6141.

[40]   J.-F. Chang, B. Sun, D.W. Breiby, M.M. Nielsen, T.I. Sölling, M. Giles, I. McCulloch, H. Sirringhaus, Chem. Mater. 16 (2004) 4772–4776.

[41]   R.J. Kline, M.D. McGehee, E.N. Kadnikova, J. Liu, J.M.J. Fréchet, M.F. Toney, M.J. Jean, Macromolecules 38 (2004) 3312–3319.

[42]   D.H. Kim, Y.D. Park, Y. Jang, H. Yang, Y.H. Kim, J.I. Han, D.G. Moon, S. Park, T. Chang, C. Chang, M. Joo, C.Y. Ryu, K. Cho, Adv. Funct. Mater. 15 (2005) 77–82.

[43]   Y.D. Park, D.H. Kim, J.A. Lim, J.H. Cho, Y. Jang, W.H. Lee, J.H. Park, K. Cho, J. Phys. Chem. C 112 (2008) 1705–1710.

[44]   K.A. Singh, G. Sauvé, R. Zhang, T. Kowalewski, R.D. McCullough, L.M. Porter, Appl. Phys. Lett. 92 (2008) 263303.

[45]   K.-J. Baeg, D. Khim, D.-Y. Kim, J.B. Koo, I.-K. You, W.S. Choi, Y.-Y. Noh, Thin Solid Films 518 (2010) 4024–4029.

[46]   Y.-D. Jiang, T.-H. Jen, S.-A. Chen, Appl. Phys. Lett. 100 (2012) 23304.

[47]   P.H. hu, . hang, . . olella, . u, J. . Park, . rinivasarao, . . rise o, . Reichmanis, ACS Appl. Mater. Interfaces 7 (2015) 6652–6660.

[48]   N. Kleinhenz, N. Persson, Z. Xue, P.H. Chu, G. Wang, Z. Yuan, M.A. McBride, D. Choi, M.A. Grover, E. Reichmanis, Chem. Mater. 28 (2016) 3905–3913.

[49]   H.E. Katz, Z. Bao, J. Phys. Chem. B 104 (2000) 671–678.

[50]   Z. Bao, A. Dodabalapur, A.J. Lovinger, Appl. Phys. Lett. 69 (1996) 4108–4110.

[51]   P.R. Gray, P.J. Hurst, S.H. Lewis, R.G. Meyer, Analysis and Design of Analog Integrated Circuits, 5th ed., Wiley-VCH, 2009.

[52]   M.E. Roberts, A.N. Sokolov, Z. Bao, J. Mater. Chem. 19 (2009) 3351.

[53]   . . . envenho, . . a chado, I. ruz- ruz, I. . H mmelge n, J. pp l. Phys. 113 (2013) 214509.

[54]   H. Bässler and A. Köhler, Electronic Processes in Organic Semiconductors: An Introduction, Wiley-VCH, 2015.

[55]   K.-C. Kao and W. Hwang, Electrical Transport in Solids: With Particular Reference to Organic Semiconductors, Oxford, 1979.

[56]   L. Salem, H.C. Longuet-Higgins, Proc. R. Soc. A 255 (1960) 435–443.

[57]   J.L. Brédas, G.B. Street, B. Thémans, J.M. André, J. Chem. Phys. 83 (1985) 1323–1329.

[58]   W. Barford, Electronic and Optical Properties of Conjugated Polymers, Second, Oxford Science Publications, Oxford, 2013.

[59] D.M. Ivory, G.G. Miller, J.M. Sowa, L.W. Shacklette, R.R. Chance, R.H. Baughman, J. Chem. Phys. 71 (1979) 1506–1507.

[60] G. Barbarella, A. Bongini, M. Zambianchi, Macromolecules 27 (1994) 3039–3045.

[61] H. Bässler, Phys. Status Solidi 107 (1981) 9–54.

[62] H. Sirringhaus, Adv. Mater. 17 (2005) 2411–2425.

[63] H. Bässler, Phys. Status Solidi 175 (1993) 15–56.

[64] M. Van der Auweraer, F.C. De Schryver, P.M. Borsenberger, H. Bässler, Adv. Mater. 6 (1994) 199–213.

[65] M. Otfried, Introduction to Solid-State Theory, Springer Series in Solid-State Sciences, 1980.

[66] A.J. Campbell, D.D.C. Bradley, D.G. Lidzey, J. Appl. Phys. 82 (1997) 6326–6342.

[67] H. Botteger, V. V. Bryksin, Hopping Conduction in Solids, Akademie Verlag Berlin, 1985.

[68] S. Roth, One-Dimensional Metals, VCH, New York, 1995.

[69] R.J. Kline, M.D. McGehee, Polym. Rev. 46 (2006) 27–45.

[70] Michael C. Petty, Molecular Electronics From Principles to Practice, Wiley-VCH, Chichester, 2007.

[71] R.D. McCullough, R.D. Lowe, J. Chem. Soc. Chem. Commun. (1992) 70.

[72] T.A. Chen, R.D. Rieke, J. Am. Chem. Soc. 114 (1992) 10087–10088.

[73] T.-A. Chen, X. Wu, R.D. Rieke, J. Am. Chem. Soc. 117 (1995) 233–244.

[74] R.S. Loewe, S.M. Khersonsky, R.D. McCullough, Adv. Mater. 11 (1999) 250–253.

[75] J.H. Bannock, S.H. Krishnadasan, A.M. Nightingale, C.P. Yau, K. Khaw, D. Burkitt, J.J.M. Halls, M. Heeney, J.C. de Mello, Adv. Funct. Mater. 23 (2013) 2123–2129.

[76] M.C. Stefan, A.E. Javier, I. Osaka, R.D. McCullough, Macromolecules 42 (2009) 30–32.

[77] H. Seyler, D.J. Jones, A.B. Holmes, W.W.H. Wong, Chem. Commun. 48 (2012) 1598–1600.

[78] H. Seyler, W.W.H. Wong, D.J. Jones, A.B. Holmes, J. Org. Chem. 76 (2011) 3551–3556.

[79] A. Kumar, J. Hasan, A. Majji, A. Avhale, S. Gopinathan, P. Sharma, D. Tarange, R. Bajpai, A. Kumar, J. Flow Chem. 4 (2014) 206–210.

[80] R. Tkachov, V. Senkovskyy, H. Komber, J.-U. Sommer, A. Kiriy, J. Am. Chem. Soc. 132 (2010) 7803–7810.

[81] A. Nawaz, M.S. Meruvia, D.L. Tarange, S.P. Gopinathan, A. Kumar, A. Kumar, H.

Bhunia, A.J. Pal, I.A. Hümmelgen, Org. Electron. 38 (2016) 89–96.

[82] N. Chandrasekaran, E. Gann, N. Jain, A. Kumar, S. Gopinathan, A. Sadhanala, R.H. Friend, A. Kumar, C.R. McNeill, D. Kabra, ACS Appl. Mater. Interfaces 8 (2016) 20243–20250.

[83] P. Stallinga, Electrical Characterization of Organic Electronic Materials and Devices, 2009.

[84] J. Veres, S. Ogier, G. Lloyd, D. de Leeuw, Chem. Mater. 16 (2004) 4543–4555.

[85] C.J. Bettinger, Z. Bao, Adv. Mater. 22 (2010) 651–655.

[86] E.A. Van Etten, E.S. Ximenes, L.T. Tarasconi, I.T.S. Garcia, M.M.C. Forte, H. Boudinov, Thin Solid Films 568 (2014) 111–116.

[87] Y. Jang, D.H. Kim, Y.D. Park, J.H. Cho, M. Hwang, K. Cho, Appl. Phys. Lett. 88 (2006) 72101.

[88] G.W. Hyung, J. Park, J.R. Koo, K.M. Choi, S.J. Kwon, E.S. Cho, Y.S. Kim, Y.K. Kim, Solid. State. Electron. 69 (2012) 27–30.

[89] C.J. Bettinger, Z. Bao, Adv. Mater. 22 (2010) 651–655.

[90] X. Wang, S. Ochiai, G. Sawa, Y. Uchida, K. Kojima, A. Ohashi, T. Mizutani, Jpn. J. Appl. Phys. 46 (2007) 1337–1342.

[91] I. Cruz-Cruz, A.C.B. Tavares, M. Reyes-Reyes, R. López-Sandoval, I.A. Hümmelgen, J. Phys. D. Appl. Phys. 47 (2014) 75102.

[92] L. Grimm, J. Electrochem. Soc. 130 (1983) 1767.

[93] E. El Shafee, R.L. Nessim, Polym. Degrad. Stab. 48 (1995) 67–69.

[94] A.R. Brown, C.P. Jarrett, D.M. de Leeuw, M. Matters, Synth. Met. 88 (1997) 37–55.

[95] J. Zaumseil, H. Sirringhaus, Chem. Rev. 107 (2007) 1296–1323.

[96] C. Deibel, D. MacK, J. Gorenflot, A. Sch??ll, S. Krause, F. Reinert, D. Rauh, V. Dyakonov, Phys. Rev. B - Condens. Matter Mater. Phys. 81 (2010).

[97] K. Kanai, T. Miyazaki, H. Suzuki, M. Inaba, Y. Ouchi, K. Seki, Phys. Chem. Chem. Phys. 12 (2010) 273–282.

[98] Z.-L. Guan, J.B. Kim, H. Wang, C. Jaye, D.A. Fischer, Y.-L. Loo, A. Kahn, Org. Electron. 11 (2010) 1779–1785.

[99] J. Frisch, M. Schubert, E. Preis, J.P. Rabe, D. Neher, U. Scherf, N. Koch, J. Mater. Chem. 22 (2012) 4418–4424.

[100] A.R. Brown, C.P. Jarrett, D.M. de Leeuw, M. Matters, Synth. Met. 88 (1997) 37–55.

[101] J. Zaumseil, H. Sirringhaus, Chem. Rev. 107 (2007) 1296–1323.

[102] M. Koehler, I. Biaggio, Phys. Rev. B 70 (2004) 45314.

[103] D. Jastrombek, A.C.B. Tavares, M.S. Meruvia, M. Koehler, I.A. Hümmelgen, Phys. Status Solidi 212 (2015) 2759–2765.

[104] K.F. Seidel, M. Koehler, Phys. Rev. B 78 (2008) 23508.

[105] M. Koehler, K.F. Seidel, Phys. Rev. B - Condens. Matter Mater. Phys. 81 (2010) 1–7.

[106] L.H. Jimison, M.F. Toney, I. McCulloch, M. Heeney, A. Salleo, Adv. Mater. 21 (2009) 1568–1572.

[107] C.C. Wang, W.-H. Lee, C.-T. Liu, Thin Solid Films 518 (2010) 7385–7389.

[108] C. de Col, A. Nawaz, I. Cruz-Cruz, A. Kumar, A. Kumar, I.A. Hümmelgen, Org. Electron. 17 (2015) 22–27.

[109] J. Sworakowski, U. Bielecka, P. Lutsyk, K. Janus, Thin Solid Films 571 (2014) 56–61.

[110] X. Sun, C. Di, Y. Liu, J. Mater. Chem. 20 (2010) 2599.

[111] T.-D. Tsai, J.-W. Chang, T.-C. Wen, T.-F. Guo, Adv. Funct. Mater. 23 (2013) 4206–4214.

[112] J. Sworakowski, K. Janus, S. Nespurek, M. Vala, IEEE Trans. Dielectr. Electr. Insul. 13 (2006) 1001–1015.

[113] A. Nawaz, I. Cruz-Cruz, R. Rodrigues, I.A. Hümmelgen, Phys. Chem. Chem. Phys. 17 (2015) 26530–26534.

[114] M.J. Rosen, J.T. Kunjappu, Surfactants and Interfacial Phenomena, 4th ed., John Wiley & Sons, Hoboken, New Jersey, 2012.

[115] A. Cifuentes, J.L. Bernal, J.C. Diez-Masa, Anal. Chem. 69 (1997) 4271–4274.

[116] C. Vautier-Giongo, B.L. Bales, J. Phys. Chem. B 107 (2003) 5398–5403.

[117] K. Shinoda, T. Nakagawa, B.-I. Tamamushi, T. Isemura, Colloidal Surfactants, Some Physiochemical Properties, Academic Press, New York, 1963.

[118] K. Shinoda, Colloidal Surfactants, Academic Press, New York, 1963.

[119] P. Somasundaran, D.W. Fuerstenau, J. Phys. Chem. 70 (1966) 90–96.

[120] J.H. Harwell, J.C. Hoskins, R.S. Schechter, W.H. Wade, Langmuir 1 (1985) 251–262.

[121] M.A. Yeskie, J.H. Harwell, J. Phys. Chem. 92 (1988) 2346–2352.

[122] T. Gu, Z. Huang, Colloids and Surfaces 40 (1989) 71–76.

[123] M.R. Bohmer, L.K. Koopal, Langmuir 8 (1992) 2649–2659.

[124] K. Hu, A.J. Bard, Langmuir 13 (1997) 5418–5425.

[125] W.A. Ducker, E.J. Wanless, Langmuir 15 (1999) 160–168.

[126] J.H. Harwell, J.C. Hoskins, R.S. Schechter, W.H. Wade, Langmuir 1 (1985) 251–262.

[127] M.A. Yeskie, J.H. Harwell, J. Phys. Chem. 92 (1988) 2346–2352.

[128] T. Gu, Z. Huang, Colloids and Surfaces 40 (1989) 71–76.

[129] B.G. Sharma, S. Basu, M.M. Sharma, Langmuir 12 (1996) 6506–6512.

[130] E.J. Wanless, W.A. Ducker, J. Phys. Chem. 100 (1996) 3207–3214.

[131] E.J. Wanless, W.A. Ducker, Langmuir 13 (1997) 1463–1474.

[132] K.A. Mazzio, A.H. Rice, M.M. Durban, C.K. Luscombe, J. Phys. Chem. C 119 (2015) 14911–14918.

[133] R.J. Kline, M.D. McGehee, E.N. Kadnikova, J. Liu, J.M.J. Frechet, Adv. Mater. 15 (2003) 1519–1522.

[134] A. Zen, J. Pflaum, S. Hirschmann, W. Zhuang, F. Jaiser, U. Asawapirom, J.P. Rabe, U. Scherf, D. Neher, Adv. Funct. Mater. 14 (2004) 757–764.

[135] R. Zhang, B. Li, M.C. Iovu, M. Jeffries-EL, G. Sauvé, J. Cooper, S. Jia, S. Tristram-Nagle, D.M. Smilgies, D.N. Lambeth, R.D. McCullough, T. Kowalewski, J. Am. Chem. Soc. 128 (2006) 3480–3481.

[136] C.-F. Hu, W.-S. Su, W. Fang, J. Micromechanics Microengineering 21 (2011) 115012.

[137] R. Willecke, F. Faupel, J. Polym. Sci. Part B Polym. Phys. 35 (1997) 1043–1048.

[138] D.H. Cole, K.R. Shull, L.E. Rehn, P. Baldo, Phys. Rev. Lett. 78 (1997) 5006–5009.

[139] D. Gamota, IEEE Standard Test Methods for the Characterization of Organic Transistors and Materials, 2004.

[140] F.C. Spano, J. Chem. Phys. 122 (2005) 234701.

[141] J. Clark, C. Silva, R.H. Friend, F.C. Spano, Phys. Rev. Lett. 98 (2007) 206406.

[142] G. Rumbles, I.D.W. Samuel, L. Magnani, K.A. Murray, A.J. DeMello, B. Crystall, S.C. Moratti, B.M. Stone, A.B. Holmes, R.H. Friend, Synth. Met. 76 (1996) 47–51.

[143] S. Yue, G.C. Berry, R.D. McCullough, Macromolecules 29 (1996) 933.

[144] J. Clark, J.-F. Chang, F.C. Spano, R.H. Friend, C. Silva, Appl. Phys. Lett. 94 (2009) 163306.

[145] A.L. Patterson, Phys. Rev. 56 (1939) 978–982.

[146] W.S. Machado, I.A. Hümmelgen, Phys. Status Solidi - Rapid Res. Lett. 6 (2012) 74–76.

[147] S.H. Kim, W.M. Yun, O.-K. Kwon, K. Hong, C. Yang, W.-S. Choi, C.E. Park, J. Phys. D. Appl. Phys. 43 (2010) 465102.

[148] N. Padma, S. Sen, S.N. Sawant, R. Tokas, J. Phys. D. Appl. Phys. 46 (2013) 325104.

[149] L.-K. Mao, J.-C. Hwang, T.-H. Chang, C.-Y. Hsieh, L.-S. Tsai, Y.-L. Chueh, S.S.H. Hsu, P.-C. Lyu, T.-J. Liu, Org. Electron. 14 (2013) 1170–1176.

[150] L.-K. Mao, J.-Y. Gan, J.-C. Hwang, T.-H. Chang, Y.-L. Chueh, Org. Electron. 15 (2014) 920–925.

[151] J. Sworakowski, Chem. Phys. 456 (2015) 106–110.

[152] S.H. Kim, W.M. Yun, O.-K. Kwon, K. Hong, C. Yang, W.-S. Choi, C.E. Park, J. Phys. D. Appl. Phys. 43 (2010) 465102.

[153] L.-K. Mao, J.-C. Hwang, T.-H. Chang, C.-Y. Hsieh, L.-S. Tsai, Y.-L. Chueh, S.S.H. Hsu, P.-C. Lyu, T.-J. Liu, Org. Electron. 14 (2013) 1170–1176.

[154] D. Jastrombek, A. Nawaz, M. Koehler, M.S. Meruvia, I.A. Hümmelgen, J. Phys. D. Appl. Phys. 48 (2015) 335104.

[155] P.G. Le Comber, W.E. Spear, Phys. Rev. Lett. 25 (1970) 509–511.

[156] H.S. Tan, N. Mathews, T. Cahyadi, F.R. Zhu, S.G. Mhaisalkar, Appl. Phys. Lett. 94 (2009) 263303.

[157] D.H. Kim, Y. Jang, Y.D. Park, K. Cho, Langmuir 21 (2005) 3203–3206.

[158] M.J. Frisch, G.W. Trucks, H.B. Schlegel, G.E. Scuseria, M.A. Robb, J.R. Cheeseman, J.A.M. Jr, T. Vreven, K.N. Kudin, J.C. Burant, J.M. Millam, (2004).

[159] T. Muck, V. Wagner, U. Bass, M. Leufgen, J. Geurts, L.W. Molenkamp, Synth. Met. 146 (2004) 317–320.

[160] A. Nawaz, I. Cruz-Cruz, J.S. Rego, M. Koehler, S.P. Gopinathan, A. Kumar, I.A. Hümmelgen, Semicond. Sci. Technol. 32 (2017) 084003.

[161] A. Nawaz, A. Kumar, I.A. Hümmelgen, Org. Electron. 51 (2017) 94–102.

[162] H. Heil, T. Finnberg, N. von Malm, R. Schmechel, H. von Seggern, J. Appl. Phys. 93 (2003) 1636–1641.

[163] S. Nagamatsu, W. Takashima, K. Kaneto, Y. Yoshida, N. Tanigaki, K. Yase, K. Omote, Macromolecules 36 (2003) 5252–5257.

[164] L. Hartmann, K. Tremel, S. Uttiya, E. Crossland, S. Ludwigs, N. Kayunkid, C. Vergnat, M. Brinkmann, Adv. Funct. Mater. 21 (2011) 4047–4057.

[165] M. Pandey, S. Nagamatsu, S.S. Pandey, S. Hayase, W. Takashima, Org. Electron. 38 (2016) 115–120.

[166] P.-H. Chu, N. Kleinhenz, N. Persson, M. McBride, J.L. Hernandez, B. Fu, G. Zhang, E. Reichmanis, Chem. Mater. 28 (2016) 9099–9109.

[167] S. Tiwari, W. Takashima, S. Nagamatsu, S.K. Balasubramanian, R. Prakash, J. Appl. Phys. 116 (2014) 94306.

[168] M. Pandey, S. Nagamatsu, S.S. Pandey, S. Hayase, W. Takashima, J. Phys. Conf. Ser. 704 (2016) 12005.

[169] M. Pandey, S.S. Pandey, S. Nagamatsu, S. Hayase, W. Takashima, Thin Solid Films 619 (2016) 125–130.

[170] T. Morita, V. Singh, S. Nagamatsu, S. Oku, W. Takashima, K. Kaneto, Appl. Phys. Express 2 (2009) 111502.

[171] M. Pandey, S.S. Pandey, S. Nagamatsu, S. Hayase, W. Takashima, J. Nanosci. Nanotechnol. 17 (2017) 1915–1922.

[172] A. Salleo, Mater. Today 10 (2007) 38–45.

[173] A. Dauendorffer, S. Nagamatsu, W. Takashima, K. Kaneto, Jpn. J. Appl. Phys. 51 (2012) 55802.

[174] X.T. Hao, T. Hosokai, N. Mitsuo, S. Kera, K.K. Okudaira, K. Mase, N. Ueno, J. Phys. Chem. B 111 (2007) 10365–10372.

[175] W.D. Oosterbaan, J.-C. Bolsée, L. Wang, V. Vrindts, L.J. Lutsen, V. Lemaur, D. Beljonne, C.R. McNeill, L. Thomsen, J. V. Manca, D.J.M. Vanderzande, Adv. Funct. Mater. 24 (2014) 1994–2004.

[176] M. Egginger, M. Irimia-Vladu, R. Schwödiauer, A. Tanda, I. Frischauf, S. Bauer, N.S. Sariciftci, Adv. Mater. 20 (2008) 1018–1022.

[177] J.H. Cho, J. Lee, Y. Xia, B. Kim, Y. He, M.J. Renn, T.P. Lodge, C.D. Frisbie, Nat. Mater. 7 (2008) 900–906.

[178] C.K. Chan, L.J. Richter, B. Dinardo, C. Jaye, B.R. Conrad, H.W. Ro, D.S. Germack, D.A. Fischer, D.M. DeLongchamp, D.J. Gundlach, Appl. Phys. Lett. 96 (2010) 133304.

[179] A. Nawaz, C. de Col, I. Cruz-Cruz, A. Kumar, A. Kumar, I.A. Hümmelgen, in:, I. McCulloch, O.D. Jurchescu, I. Kymissis, R. Shinar, L. Torsi (Eds.), 2015, p. 95681A.

[180] P. Sonar, S.P. Singh, Y. Li, Z.-E. Ooi, T. Ha, I. Wong, M.S. Soh, A. Dodabalapur, Energy Environ. Sci. 4 (2011) 2288.

[181] S.Y. Son, Y. Kim, J. Lee, G.-Y. Lee, W.-T. Park, Y.-Y. Noh, C.E. Park, T. Park, J. Am. Chem. Soc. 138 (2016) 8096–8103.

[182] Y. Li, P. Sonar, S.P. Singh, W. Zeng, M.S. Soh, J. Mater. Chem. 21 (2011) 10829.

[183] J.S. Lee, S.K. Son, S. Song, H. Kim, D.R. Lee, K. Kim, M.J. Ko, D.H. Choi, B. Kim, J.H. Cho, Chem. Mater. 24 (2012) 1316–1323.

[184] Z. Fei, L. Chen, Y. Han, E. Gann, A.S.R. Chesman, C.R. McNeill, T.D. Anthopoulos, M. Heeney, A. Pietrangelo, J. Am. Chem. Soc. 139 (2017) 8094–8097.

[185] T. Lei, J.-H. Dou, J. Pei, Adv. Mater. 24 (2012) 6457–6461.

[186] J. Li, Y. Zhao, H.S. Tan, Y. Guo, C.-A. Di, G. Yu, Y. Liu, M. Lin, S.H. Lim, Y. Zhou, H. Su, B.S. Ong, Sci. Rep. 2 (2012) 754.

[187] R. Toniolo, I.A. Hümmelgen, Macromol. Mater. Eng. 289 (2004) 311–314.

[188] S. M. Sze, Physics of Semiconductor Devices, Wiley-VCH, 1964.

Scientific contributions

Journal papers

1. <u>A. Nawaz</u>, A. C. B. Tavares, T. T. Do, B. Patel, P. Sonar and I. A. Hümmelgen, *Experimental and Modelling Study of Low-voltage Field-effect Transistors Fabricated with Molecularly Aligned Copolymer Floating Films*, **2017** (submitted for publication).

2. <u>A. Nawaz</u>, A. Kumar and I. A. Hümmelgen, *Ultra-high mobility in defect-free poly(3-hexylthiophene-2,5-diyl) field-effect transistors through supra-molecular alignment*, Organic Electronics 51, 94, **2017**.

3. <u>A. Nawaz</u>, I. Cruz-Cruz, J. S. Rego, M. Koehler, S. Gopinathan, A. Kumar and I. A. Hümmelgen, *Polymer-dielectric molecular interactions in defect-free poly(3-hexylthiophene): dependence and consequences of regioregularity on transistor charge transport properties*, Semiconductor Science and Technology 32, 084003, **2017**.

4. <u>A. Nawaz</u>, M. S. Meruvia, D. L. Tarange, S. P. Gopinathan, A. Kumar, A. Kumar, H. Bhunia, A. J. Pal and I. A. Hümmelgen, *High mobility organic field-effect transistors based on defect-free regioregular poly(3-hexylthiophene-2, 5-diyl)*, Organic Electronics 38, 89, **2016**.

5. <u>A. Nawaz</u>, C. de Col and I. A. Hümmelgen, *Poly (Vinyl Alcohol) Gate Dielectric Treated With Anionic Surfactant in C60 Fullerene-Based n-Channel Organic Field Effect Transistors*, Materials Research 19, 1201, **2016**.

6. D. Jastrombek, <u>A. Nawaz</u>, M. Koehler, M. S. Meruvia and I. A. Hümmelgen, *Modification of the charge transport properties of the copper phthalocyanine/poly(vinyl alcohol) interface using cationic or anionic surfactant for field-effect transistor performance enhancement*, Journal of Physics D: Applied Physics 48, 335104, **2015**.

7. <u>A. Nawaz</u>, I. Cruz-Cruz, R. Rodrigues and I. A. Hümmelgen, *Performance enhancement of poly(3-hexylthiophene-2,5-diyl) based field effect transistors through surfactant*

treatment of the poly (vinyl alcohol) gate insulator surface, Physical Chemistry Chemical Physics 17, 26530, **2015**.

8. C. de Col, <u>A. Nawaz</u>, I. Cruz-Cruz, A. Kumar, A. Kumar and I. A. Hümmelgen, *Poly(vinyl alcohol) gate dielectric surface treatment with vitamin C for poly(3-hexylthiophene-2,5-diyl) based field effect transistors performance improvement*, Organic Electronics 17, 22, **2015**.

Conference papers

1. <u>A. Nawaz</u>, C. de Col, I. Cruz-Cruz, A. Kumar, A. Kumar and I. A. Hümmelgen, *Gate dielectric surface treatments for performance improvement of poly (3-hexylthiophene-2, 5-diyl) based organic field-effect transistors*, SPIE Organic Photonics+ Electronics, 95681A, **2015**.

Presentations in conferences and meetings

1. <u>A. Nawaz</u>, A. Kumar and I. A. Hümmelgen, *Ultra-high mobility in defect-free poly(3-hexylthiophene) field-effect transistors through alignment of supra-molecular assemblies*, XVI MRS SBPMat Meeting – Gramado, Brazil, September 2017 (*oral presentation*).

2. <u>A. Nawaz</u>, I. Cruz-Cruz, J. S. Rego, M. Koehler, S. P. Gopinathan, A. Kumar and I. A. Hümmelgen, *Channel interface molecular interactions in defect-free poly(3-hexylthiophene) and consequences on transistor charge transport properties*, XVI MRS SBPMat Meeting – Gramado, Brazil, September 2017 (*poster presentation*).

3. <u>A. Nawaz</u>, C. de Col, I. Cruz-Cruz, A. Kumar, A. Kumar and I. A. Hümmelgen, *Gate dielectric surface treatments for performance improvement of poly(3-hexylthiophene-2,5-diyl) based organic field-effect transistors*, SPIE Optics + Photonics conference – San Diego, USA, August 2015 (*poster presentation*).

4. <u>A. Nawaz</u>, I. Cruz-Cruz, R. Rodrigues and I. A. Hümmelgen, *Hexadecyltrimethylammonium bromide (CTAB) treated Poly(3-hexylthiophene-2,5-diyl) semiconductor and cross-linked poly(vinyl alcohol) insulator based organic field-effect transistors*, XIII MRS SBPMat Meeting – João Pessoa, Brazil, September 2014 (*poster presentation*).